Parton distributions and lattice QCD calculations:
toward 3D structure

July 8, 2020

Martha Constantinou,[1,∗] Aurore Courtoy,[2] Markus A. Ebert,[3] Michael Engelhardt,[4,∗] Tommaso Giani,[5] Tim Hobbs,[6,7]
Tie-Jiun Hou,[8] Aleksander Kusina,[9] Krzysztof Kutak,[9] Jian Liang,[10] Huey-Wen Lin,[11,12,∗,†] Keh-Fei Liu,[10]
Simonetta Liuti,[13] Cédric Mezrag,[14] Pavel Nadolsky,[6] Emanuele R. Nocera,[15,∗] Fred Olness,[6,∗] Jian-Wei Qiu,[7]
Marco Radici,[16] Anatoly Radyushkin,[7,17] Abha Rajan,[18] Ted Rogers,[7,17] Juan Rojo,[15,19] Gerrit Schierholz,[20]
C.-P. Yuan,[11] Jian-Hui Zhang,[21] Rui Zhang[11,12]   (∗editors)

[1] *Department of Physics, Temple University, 1925 N. 12th Street, Philadelphia, PA 19122-1801, USA*
[2] *Instituto de Física, Universidad Nacional Autónoma de México,Apartado Postal 20-364, 01000 Ciudad de México, Mexico*
[3] *Center for Theoretical Physics, Massachusetts Institute of Technology, Cambridge, MA 02139, USA*
[4] *Department of Physics, New Mexico State University, Las Cruces, NM 88003, USA*
[5] *Higgs Centre for Theoretical Physics, University of Edinburgh, Peter Guthrie Tait Road, Edinburgh EH9 3FD, United Kingdom*
[6] *Department of Physics, Southern Methodist University, Dallas, TX 75275, USA*
[7] *Thomas Jefferson National Accelerator Facility, Newport News, VA 23606, USA*
[8] *Department of Physics, College of Sciences, Northeastern University, Shenyang 110819, China*
[9] *Institute of Nuclear Physics Polish Academy of Sciences, PL-31342 Krakow, Poland*
[10] *Department of Physics and Astronomy, University of Kentucky, Lexington, KY 40506, USA*
[11] *Department of Physics and Astronomy, Michigan State University, East Lansing, MI 48824, USA*
[12] *Department of Computational Mathematics, Science and Engineering, Michigan State University, East Lansing, MI 48824, USA*
[13] *Physics Department, University of Virginia, 382 MCormick Road, Charlottesville, VA 22904, USA*
[14] *Irfu, CEA, Université Paris Saclay, F-91191, Gif-sur-Yvette, France*
[15] *Nikhef Theory Group, Science Park 105, 1098 XG Amsterdam, The Netherlands*
[16] *INFN - Sezione di Pavia, I27100 Pavia, Italy*
[17] *Department of Physics, Old Dominion University, Norfolk, VA 23529, USA*
[18] *Physics Department, Brookhaven National Laboratory, Upton, New York 11973, USA*
[19] *Department of Physics and Astronomy, VU University Amsterdam, Amsterdam, The Netherlands*
[20] *Deutsches Elektronen-Synchrotron DESY, 22603 Hamburg, Germany*
[21] *Center of Advanced Quantum Studies, Department of Physics, Beijing Normal University, Beijing 100875, China*

The strong force which binds hadrons is described by the theory of Quantum Chromodynamics (QCD). Determining the character and manifestations of QCD is one of the most important and challenging outstanding issues necessary for a comprehensive understanding of the structure of hadrons. Within the context of the QCD parton picture, the Parton Distribution Functions (PDFs) have been remarkably successful in describing a wide variety of processes. However, these PDFs have generally been confined to the description of collinear partons within the hadron. New experiments and facilities provide the opportunity to additionally explore the transverse structure of hadrons which is described by Generalized Parton Distributions (GPDs) and Transverse Momentum Dependent Parton Distribution Functions (TMD PDFs). In our previous report (Lin *et al.*, 2018d), we compared and contrasted the two main approaches used to determine the collinear PDFs: the first based on perturbative QCD factorization theorems, and the second based on lattice QCD calculations. In the present report, we provide an update of recent progress on the collinear PDFs, and also expand the scope to encompass the generalized PDFs (GPDs and TMD PDFs). We review the current state of the various calculations, and consider what new data might be available in the near future. We also examine how a shared effort can foster dialog between the PDF and Lattice QCD communities, and yield improvements for these generalized PDFs.

The authors welcome comments and suggestions regarding the report content.
[†]Corresponding author: Huey-Wen Lin   `hwlin@pa.msu.edu`

arXiv:2006.08636v2 [hep-ph] 7 Jul 2020

CONTENTS

I. INTRODUCTION AND MOTIVATION

The Standard Model (SM) of particle physics has been remarkably successful in describing the nature of the elementary constituents and their interactions. Of the four fundamental forces, the strong interaction as described by the theory of quantum chromodynamics (QCD) is particularly intriguing, as it exhibits a wealth of phenomena (confinement, spontaneous chiral symmetry breaking, anomalies, instantons) and binds the quarks and gluons that form the observable hadrons. However, it is precisely these properties of QCD that make it challenging to characterize the structure of the strongly interacting hadrons in the context of conventional perturbation theory.

On the experimental front, there are a number of planned and proposed new facilities on the horizon which can provide a wealth of new data to help us better characterize the strong interaction; this will improve our knowledge of the fundamental forces and constituents of nature and lead to new discoveries. To fully utilize this new experimental information, it is imperative that our theoretical tools advance to keep pace; this is the focus of our report.

The QCD-based parton picture has provided a reliable computational framework for describing the physics of hadrons. However, an essential ingredient for these calculations are the parton distribution functions (PDFs), which encode the properties of quarks and gluons inside the hadrons. Ultimately, the accuracy of any calculation based on the QCD parton model depends on the accuracy of the PDFs; thus, the PDFs are crucial for current LHC measurements as well as future HL-LHC, LHeC, and EIC investigations.

Unfortunately the PDFs are, at present, often the element that limits the precision. For example, the focus of the upcoming LHC runs will be to improve the event statistics with increased luminosity; thus, the path to future discoveries will be delineated with high-precision comparisons as we search for discrepancies between the data and the Standard-Model predictions. Hence, our ability to fully characterize the Higgs boson and constrain any new-physics signatures ultimately comes down to how accurately we can determine the underlying PDFs.

We also note here that the PDFs are imperative for some astrophysical studies, including high-energy cosmic rays which are used to compute atmospheric neutrino backgrounds.

At present, the computation of PDFs from first principles is complex, computationally intensive, and it requires diligence and ingenuity to minimize uncertainties.

There are two main communities with complementary approaches to determining the PDFs: 1) determination by global analysis of experimental measurements, and 2) direct computation using lattice QCD. The global

QCD analyses use large experimental data sets in the context of the QCD parton model (along with factorization theorems) to extract process-independent PDFs. The lattice-QCD approach directly computes the QCD path integral on a discretized finite-volume Euclidean space-time grid to extract moments of PDFs, quasi-PDFs, and other quantities.

A general overview of these approaches was presented in the 2017 PDFLattice report (Lin *et al.*, 2018d); this work grew out of a 2017 workshop[1] which brought the two communities together to address common questions and followed up on the very fruitful discussions and interactions that took place during the workshop. That first document served as a common reference to standardize notation and conventions to facilitate communication between these communities.

This current report grew out of a follow-up 2019 workshop;[2] it updates and extends the scope of the previous studies in a number of dimensions.

In particular, the prospect of future LHeC and EIC facilities enables us to contemplate expanding beyond the collinear PDF framework and considering also generalized parton distributions (GPDs) and transverse-momentum–dependent (TMD) PDFs. Together with the collinear PDFs, we can obtain a complete three-dimensional description of the hadron structure.

The conventional PDFs $f(x)$ describe the probability of finding a parton with momentum fraction x inside a hadron moving in the infinite momentum frame; in this case, the parton is *assumed* to be moving collinear to the hadron with zero transverse momentum. If we desire additional information about the parton, we could ask about the transverse momentum $\mathbf{k_T}$ and the impact parameter $\mathbf{b_T}$ of the parton relative to the parent hadron. Both $\mathbf{k_T}$ and $\mathbf{b_T}$ are 2-dimensional vectors measured relative to the axis defined by the hadron momentum. Combining this information together yields the 5-dimensional Wigner distribution $W(x, \mathbf{k_T}, \mathbf{b_T})$ which, in a sense, provides complete information on the parton. If we integrate the Wigner distribution over the transverse momentum, we obtain a Generalized Parton Distribution (GPD) $f_{\mathrm{GPD}}(x, \mathbf{b_T})$, while if we integrate over the impact parameter we obtain a Transverse Momentum Dependent (TMD) PDF $f_{\mathrm{TMD}}(x, \mathbf{k_T})$. Thus, by expanding the scope of our investigations beyond collinear PDFs to include GPDs and TMD PDFs we can extract more detailed information on the partons which comprise the hadron.

Not only do the GPDs describe the spatial distributions of quarks and gluons in the plane transverse to the hadron momentum, but they also provide a mechanism to study the rich spin structure of the hadrons. Together with the collinear information encoded in the x momentum fraction variable, the GPDs provide a three-dimensional (3D) tomographic image of the structure of hadrons in terms of QCD's quarks and gluons.

Likewise, the TMD PDFs encode not only the transverse momentum distribution of the hadronic components, but can also provide the polarization degrees of freedom. The information about transverse degrees of freedom is essential in the context of QCD factorization theorems for multiscale, noninclusive collider observables. The transverse momentum degrees of freedom of partons can be addressed within so called transverse-momentum–dependent factorization, where essentially the transverse momentum is much smaller than the hard scale of the final state. A typical process where one applies this factorization is Drell-Yan production. Another approach (valid at low x) is addressed within the color-glass condensate (CGC) model, which is an effective model formulated within QCD.

The broad objective of our work is to advance tools that can perform detailed comparisons between data and QCD theory, as well as combine information from the two sides, to gain an enhanced understanding of the various PDFs. This work is ongoing and forms the basis for next-generation PDF input to facilitate precision measurements and new discoveries at the future hadron facilities, as we validate our understanding of the SM and search for deviations which might signal evidence of new physics.

The outline of this paper is as follows. In Section 2 we review the essential elements of the global QCD analysis and lattice-QCD methods for collinear PDFs, and highlight some of the recent developments. In Section 3 we introduce the GPDs and discuss areas where lattice QCD and machine learning (ML) can contribute. In Section 4 we introduce TMD PDFs, including the new lattice quasi-TMD PDFs, and discuss recent advances. In Section 5 we discuss future interactions between the global-analysis and lattice-QCD communities and offer some conclusions.

This document presents work that appears in the literature until June 1, 2020 (published, or on the arXiv). The discussion is extended to conference proceedings for recent work that has not been published elsewhere. To keep this document at a reasonable length, we present selected aspects of each publication discussed in the main text and we encourage the interested reader to consult the referred work.

---

[1] Parton Distributions and Lattice Calculations in the LHC era (**PDFLattice2017**) 22–24 March 2017, Oxford University, UK. http://www.physics.ox.ac.uk/confs/PDFlattice2017
[2] Parton Distributions and Lattice Calculations (**PDFLattice2019**) 25–27 September 2019, Michigan State University (MSU) Kellogg Biological Station, USA. https://indico.cern.ch/event/804857/

II. PARTON DISTRIBUTION FUNCTIONS

In the framework of leading-twist collinear factorization (Collins *et al.*, 1989), PDFs are the momentum densities of partons carrying a fraction x of the momentum of their parent nucleon. Depending on the polarization of the parton with respect to that of the nucleon, three collinear PDF species can be defined: the unpolarized PDF, f, for an unpolarized parton in an unpolarized nucleon; the helicity PDF, Δf, for the net amount of partons polarized along or opposite a longitudinally polarized nucleon; and the transversity PDF, $\delta f = h_1^f$, for the net amount of quarks polarized along or opposite a transversely polarized nucleon. In canonical field theory, PDFs are equivalently defined in terms of matrix elements of bi-local operators, *e.g.* for quarks

$$
\begin{aligned}
f(x) &= \frac{1}{4\pi} \int dy^- e^{-ixP^+y^-} \langle P,S|\bar{\psi}_f \gamma^+ \mathcal{W}\psi_f|P,S\rangle, \\
\Delta f(x) &= \frac{1}{4\pi} \int dy^- e^{-ixP^+y^-} \langle P,S|\bar{\psi}_f \gamma^+ \gamma^5 \mathcal{W}\psi_f|P,S\rangle, \\
h_1^f(x) &= \frac{1}{4\pi} \int dy^- e^{-ixP^+y^-} \langle P,S|\bar{\psi}_f i\sigma^{1+}\gamma^5 \mathcal{W}\psi_f|P,S\rangle,
\end{aligned}
\tag{1}
$$

where $\bar{\psi}_f = \bar{\psi}_f(0,0,\mathbf{0}_\perp)$ and $\psi_f = \psi_f(0,y^-,\mathbf{0}_\perp)$ are the (quark) fields, $y^\pm = \frac{1}{2}(y^0 \pm y^3)$ are the spacetime coordinates along the lightcone direction, γ are the Dirac matrices, σ are the Pauli matrices, $\mathcal{W}$ is the Wilson line ensuring the Gauge invariance of the operator, and P and S are the momentum and spin of the proton. All four-vectors are expressed using light-cone coordinates.

Expressions similar to those in Eq. (1) also hold for upolarized and helicity gluon PDFs. They all include renormalization of all fields and coupling in the $\overline{\text{MS}}$ scheme (see (Kovařík *et al.*, 2019) for details), a fact that makes PDF depend on the (renormalization) scale μ. This dependence is purely perturbative, and can be computed by means of DGLAP evolution equations (Altarelli and Parisi, 1977; Dokshitzer, 1977; Gribov and Lipatov, 1972). Nuclear modifications, occurring when a nucleon is bound in a nucleus, do not alter these definitions: nuclear and nucleon PDFs are defined by the same leading-twist operators entering Eq. (1) (though acting on different states), therefore it is customary to assume that nuclear modifications can be absorbed into PDFs.

In this Section, we review recent progress in the determination of unpolarized, helicity and transversity PDFs from the two methods delineated in the Introduction: global QCD analyses of experimental data, on the one hand; and lattice QCD, on the other hand. We focus on updates occurred since the publication of the 2017 PDFLattice report (Lin *et al.*, 2018d). We then investigate possible intersections between the two methods, specifically three aspects that we deem of particular relevance: moments of PDFs, the use of lattice data in global fits, and the unpolarized and helicity strange PDF.

II.1. Global PDFs Updates

A global QCD analysis of PDFs consists in modeling PDFs by means of a suitable parametrization, which is then optimized by comparing PDF-dependent predictions for one or more physical scattering processes involving initial-state nucleons to (multiple sets of) their actual measurements. In this sense, a PDF determination can be considered a nonlinear-regression problem, in which one has to learn the relative weights of a set of functions from data. Key to this procedure are QCD factorization theorems (Collins *et al.*, 1989), according to which the cross section for a class of sufficiently inclusive hadronic processes can be determined by folding the PDFs with perturbatively computable partonic cross sections.

The accuracy and precision of a PDF determination largely depend on the data set and on the theoretical and statistical sophistication of the analysis. The input data sets are remarkably different across the three PDF species defined in Eq. (1); while there are thousands of measurements available to determine the unpolarized PDFs, there are typically only hundreds of them for the helicity, and tens for the transversity. The kinematic coverage and the variety of hadronic processes decreases accordingly: unpolarized and helicity PDFs benefit, although to a different extent, from measurements in inclusive and semi-inclusive deep-inelastic scattering (DIS and SIDIS), Drell-Yan (DY), and a variety of proton-proton (pp) scattering processes (including gauge-boson, jet, and heavy-particle production). The transversity PDF, instead, is limited by its nature to processes coupled to a chiral-odd final state; in a purely collinear framework, that is di-hadron production in SIDIS or in pp collisions (Di). This state of affairs is summarized in Fig. 1, where we display the kinematic coverage, in the (x, Q^2)-plane ($Q = \mu$ is the characteristic scale of the data), of the hadronic cross section data for the processes commonly included in modern QCD analyses of unpolarized, helicity and transversity PDFs. The dashed line is at $Q = 1$ GeV. Data below this value are usually not included in QCD analyses of PDFs because QCD becomes largely non-perturbative, due to the growth of the strong coupling. The extended kinematic ranges attained by a future Large Hadron-electron Collider (LHeC) (Abelleira Fernandez *et al.*, 2012) or a polarized Electron-Ion Collider (EIC) (Accardi *et al.*, 2016b) are also displayed. A corresponding plot for unpolarized nuclear PDFs can be found in Fig. 1 of Ref. (Ethier and Nocera, 2020).
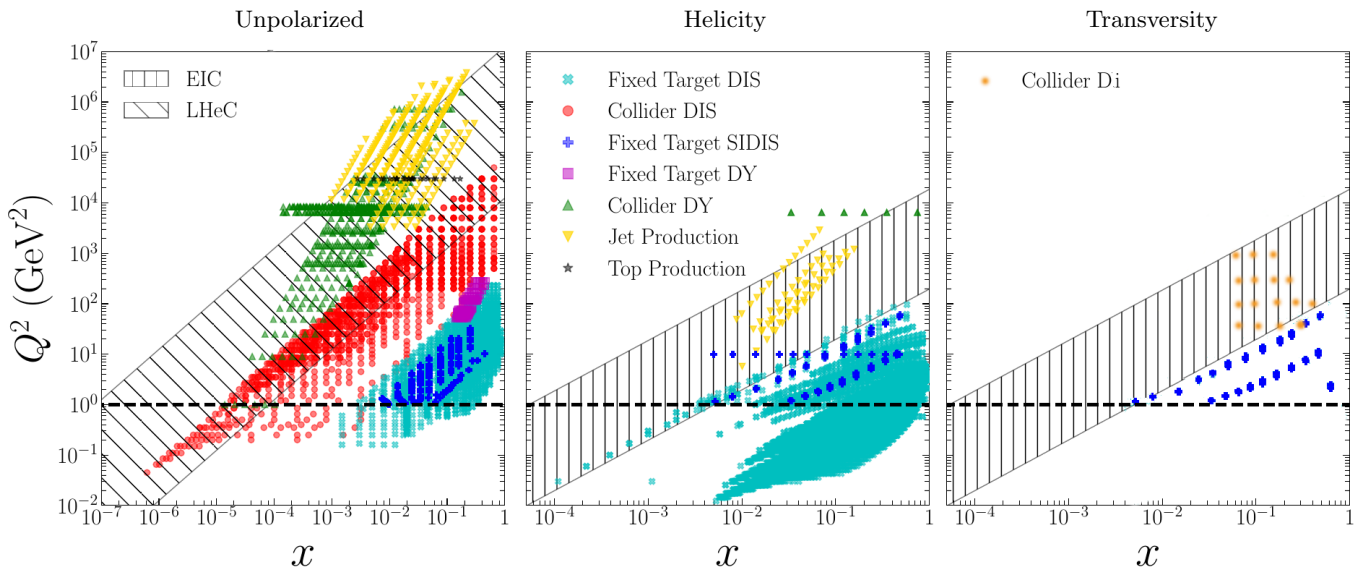
FIG. 1 The kinematic coverage in the (x, Q^2) plane of the hadronic cross-section data for the processes commonly included in global QCD analyses of collinear unpolarized, helicity, and transversity PDFs. The extended kinematic ranges attained by the LHeC and the EIC are also displayed. See Fig. 1 of Ref. (Ethier and Nocera, 2020) for unpolarized nuclear PDFs.

The remainder of this section will present a summary of recent developments in the determination of unpolarized, helicity and transversity PDFs, and will outline their respective features. We refer the interested reader to Ref. (Ethier and Nocera, 2020) for a recent, more extended review of the subject.

II.1.1. Unpolarized PDFs

The continued excellent performance of the CERN Large Hadron Collider (LHC) (Evans and Bryant, 2008) has brought the determination of unpolarized PDFs in a precision era. The recent completion of Run II has accumulated data from an integrated luminosity of approximately 150 fb^{-1}, a fact that shrank the statistical uncertainty of the measurements to unprecedented small values, typically 1% or less. This state of affairs challenges PDFs as a tool to perform precision tests of the SM and searches of new physics; PDFs must become comparably precise. Next-to-next-to-leading order (NNLO) accuracy has become standard, and large efforts were also devoted to update PDF sets with an increasing amount of LHC measurements, to develop statistical tools to investigate the impact and/or inconsistencies of the data, and to represent residual theoretical uncertainties (*e.g.* beyond NNLO) in the PDFs. On the other hand, PDFs remain key to understand the nonperturbative structure of the proton, for instance to investigate the role of higher-twist terms in the operator product expansion, or the shape of the ratio of d to u flavor at large x. In the following, we discuss these aspects by summarizing the progress of the leading PDF sets.

The CTEQ-TEA collaboration has recently released their new CT18 PDF set (Hou *et al.*, 2019b), accurate up to NNLO. More than 700 data points from 12 new LHC data sets were included in the new fits. Among them, the most important data sets that drove changes in the quark and antiquark PDFs are the LHCb W- and Z-boson data at 7 and 8 TeV. Very mild changes in the fitted PDFs were observed with the addition of the ATLAS 8-TeV and CMS 7- and 8-TeV W- and Z-boson data. Changes in the gluon PDF were instead driven by the inclusion of CMS and ATLAS jet data, and of ATLAS 8-TeV Z-boson transverse-momentum distributions, which both made the central value and the uncertainty of the gluon decrease in the region $0.1 < x < 0.4$. The subsequent inclusion of top-pair–production data from ATLAS and CMS, in particular of single- and double-differential distributions, was demonstrated to have little impact in the CT18 fit. Finally, the central value of the sea-quark ratio $(s + \bar{s}) / (\bar{u} + \bar{d})$ increased in the small-x region, due predominantly to the inclusion of LHCb data. A methodology to study the sensitivity and the impact of specific data sets to the PDFs without the need of performing a fit was also developed (Hou *et al.*, 2019a; Schmidt *et al.*, 2018; Wang *et al.*, 2018). A variant of the baseline CT18 fit, called CT18Z, was determined with the additional inclusion of the ATLAS 7-TeV $W^{\pm}/Z$ rapidity distributions and by taking the factorization and renormalization scales in the DIS process to be x-dependent. The fit represents the maximal deviation from the nominal CT18 fit, notably in the gluon and strange-quark PDFs. The resulting PDFs for the CT18 set, which are representative of the qualitative status of
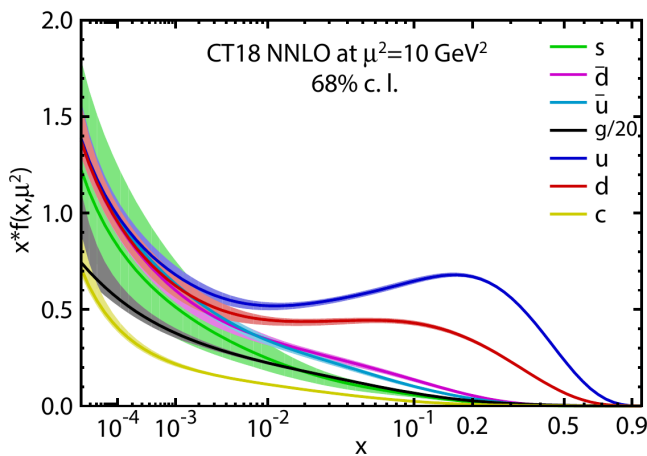
FIG. 2 The CT18 PDFs at $\mu^2 = 10$ GeV^2 for the xu, $x\bar{u}$, xd, $x\bar{d}$, $xs = x\bar{s}$, and xg PDFs. Error bands correspond to the 68% confidence level. Figure from (Kovařík *et al.*, 2019).

current unpolarized PDFs, are shown in Fig. 2.

The latest general-purpose PDF determination from the MMHT collaboration is MMHT14 (Harland-Lang *et al.*, 2015), which was later extended to include HERA I–II legacy measurements (Harland-Lang *et al.*, 2016), jet-production measurements (Harland-Lang *et al.*, 2018), and differential measurements in top-pair production (Bailey and Harland-Lang, 2020) from the LHC. These intermediate updates demonstrated that experimental correlations across systematic uncertainties have been improperly estimated for some of the ATLAS jet and differential top data sets. The features of a new preliminary general-purpose PDF set were presented in Ref. (Thorne *et al.*, 2019), which included new LHC data sets, notably the particularly precise 7-TeV ATLAS W- and Z-boson measurements, which increase the ratio of strange to non-strange light sea quarks at low x, whilst still allowing for a positive light-sea-quark asymmetry, albeit with a maximum at slightly lower x. The MMHT fit has also been updated with an improved and extended parametrization based on Chebyshev polynomials.

The NNPDF collaboration released their latest general-purpose PDF set in Ref. (Ball *et al.*, 2017). This was later extended to include direct photon (Campbell *et al.*, 2018), single-top (Nocera *et al.*, 2019), and dijet-production measurements (Abdul Khalek *et al.*, 2020) from the LHC. A reassessment of the impact of top-pair differential distributions measured by ATLAS at 8 TeV was also presented in Ref. (Amoroso *et al.*, 2020), which demonstrated the different impact of absolute and normalized distributions in the fit, and the importance of fitting charm in their description. The NNPDF collaboration has also developed a statistical procedure to represent theory uncertainties in PDFs (Ball and Deshpande, 2019), and applied it to missing higher-order corrections (MHOU) in the strong-coupling expansion of

theoretical predictions (Abdul Khalek *et al.*, 2019b,c), and to nuclear uncertainties in observables obtained from scattering off nuclear targets (Ball *et al.*, 2019). The procedure consists in supplementing the experimental covariance matrix with a theoretical covariance matrix estimated by way of an educated guess. In the case of MHOU, correlated uncertainties were estimated at next-to-leading order (NLO) by varying the factorization and renormalization scales according to various prescriptions; in the case of nuclear corrections, correlated uncertainties were estimated as the difference between theoretical predictions obtained either with a free-proton or nuclear PDF. The representation of such uncertainties in PDFs is likely to become mandatory in the future, because their size is comparable to that determined from the uncertainty of the data. The inclusion of such theoretical uncertainties was demonstrated to improve the description of the data, while increasing PDF uncertainties only mildly.

In Fig. 3 we compare the CT18, MMHT14 and NNPDF3.1 PDF sets at a scale $Q = \mu = 2$ GeV. Specifically, we display the following PDF combinations from top to bottom and left to right: $u_v + d_v = u - \bar{u} + d - \bar{d}$, $u - d$, $\bar{u} + \bar{d}$, $\bar{d} - \bar{u}$, $s + \bar{s}$, $s - \bar{s}$, $c + \bar{c}$ and g. Note the special scale on the x axis. While the three global analyses produce similar total valence distributions $u_v + d_v$ for $0.05 \lesssim x \lesssim 0.5$, their predictions on other flavor combinations could differ by 10% or more, as in $\bar{u} - \bar{d}$, $\bar{u} + \bar{d}$, $s + \bar{s}$, $c + \bar{c}$ and g. In particular, the $c + \bar{c}$ PDF combination is largely different between NNPDF3.1 and the other sets, given that charm is parametrized on the same footing as other PDFs in the NNPDF3.1 set, while it is generated perturbatively in the others. Finally, note that the difference $s - \bar{s}$ is not displayed for CT18 because they assume $s = \bar{s}$; MMHT14 and NNPDF3.1 determine s and $\bar{s}$ PDFs independently.

Beside the three general-purpose PDF sets described above, other unpolarized PDF determinations have been produced or updated recently, namely ABMP, CJ, JAM and HERAPDF. These PDF sets are based on a reduced set of measurements and/or on peculiar theoretical assumptions. As such, they are more limited in scope.

The ABMP16 (Alekhin *et al.*, 2017) PDF set is the only unpolarized PDF set determined in a schemes with a fixed number of flavors: for 3, 4 and 5 active flavors separately. It was recently supplemented with an extended set of single-top and top-pair measurements from the Tevatron and the LHC and an increasing number of DY data, notably recent ATLAS gauge-boson–production distributions at 5 and 7 TeV and double-differential distributions for Z-boson production from ATLAS and CMS. More stringent kinematic cuts have been applied, which reduce the impact of higher-twist terms included in the analysis.

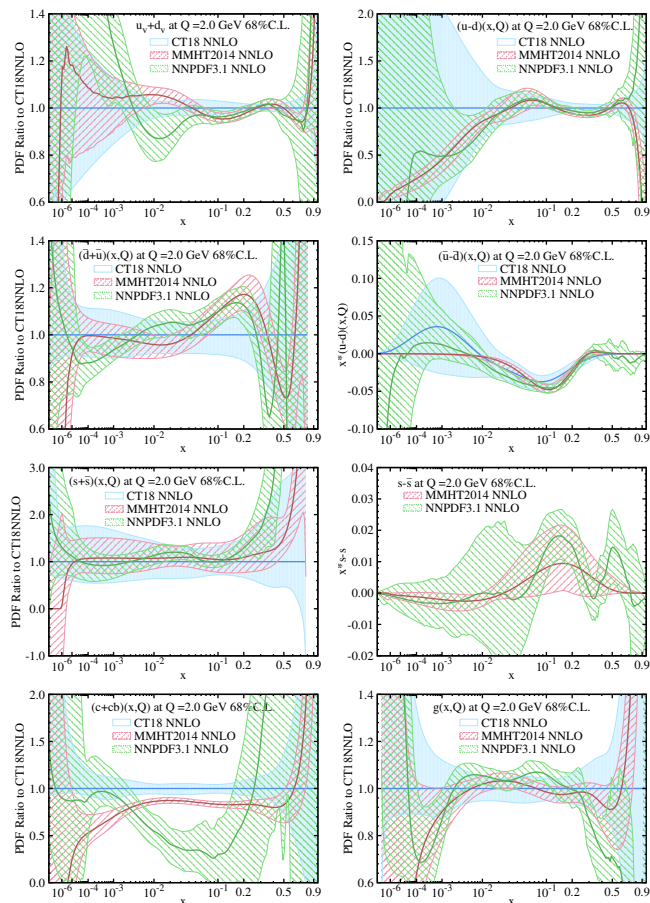The CJ15 (Accardi *et al.*, 2016a) analysis determined

FIG. 3 The CT18, MMHT14 and NNPDF3.1 PDFs at $Q = 2$ GeV for various flavor combinations.

FIG. 4 The u/d ratio for the CT18, CT14HERA2 and CJ15 PDFs at $Q = 10$ GeV.

the ratio d/u at NLO by including fixed-target DIS data at low Q and high x, which are otherwise excluded by kinematic cuts in other PDF analyses. In order to reduce theoretical bias, higher-twist contributions and nuclear effects important in this kinematic region were included in the analysis. In Fig. 4 the d/u ratio obtained from the CJ15 analysis at NLO is compared to the result obtained from the CT14HERA2 (Hou *et al.*, 2017) and CT18 analyses at NNLO. The plot shows that the CT18 and CJ15 central predictions converge to different values at large x, respectively 0.1 and 0.2. Nevertheless, the CT18 and CJ15 results are compatible within uncertainties, although the CJ15 error band is much smaller than the CT18 one, possibly because the tolerance criterion is not adopted in the CJ15 analysis.

The JAM collaboration performed the first *universal fit*, JAM19 (Sato *et al.*, 2020), a simultaneous determination of PDFs and fragmentation functions (FFs) at NLO from a global analysis of DIS, DY, SIDIS and electron-positron annihilation data. This fit is unique in its kind, as it allows investigation of the unpolarized sea-quark PDFs from semi-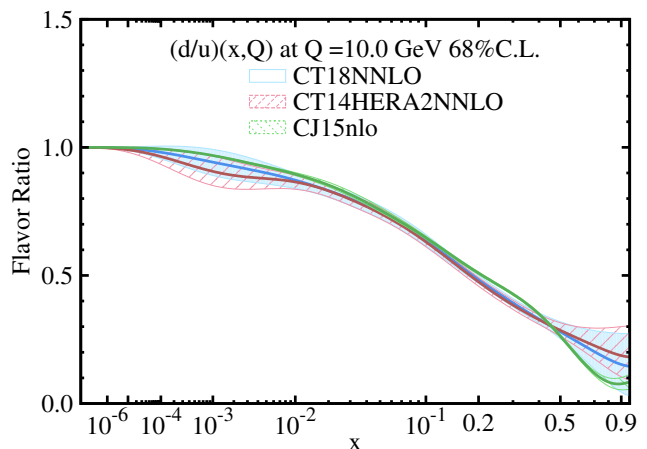inclusive processes, whereby bias from the unknown FFs is minimised as much as possible. The fit revealed in particular a strong suppression of the strange PDF from kaon production, in contrast to what is found in all other PDF determinations, which deserves further investigation.

Finally, the HERAPDF2.0 set was updated (Cooper-Sarkar, 2019) with the HERA legacy inclusive DIS data set supplemented with (multi-)jet production data in DIS from ZEUS and H1. Theoretical predictions were computed at NNLO with NNLOJET (Gehrmann *et al.*, 2018) for the first time. The new NNLO fit favors a value of the strong coupling $\alpha_s(M_Z) = 0.1150$ which is lower than that found at NLO, $\alpha_s(M_Z) = 0.1183$. Consequently, two new HERA2PDF2.0Jets NNLO fits, with different α_s values were made available.

As a general remark, we note that the small-x region of unpolarized PDFs is phenomenologically relevant for the production of final states, for example dijets in the forward-rapidity region of HERA, RHIC and LHC. In pp collision, a final state of rapidity around 4 can probe momentum regions as low as $x \sim 10^{-4}$. Furthermore, in heavy-ion collisions it is believed that the small-x gluons form an over-occupied system needed for later thermalization of quark-gluon plasma. A precise understanding of the gluon PDF at low x is therefore of uttermost importance, and represents a domain where all of the analyses discussed above can be improved, for instance along th elines of Ref. (Ball *et al.*, 2018). The current approach to studying the small-x gluon density is formulated upon the Balitsky-Kovchegov equation (Balitsky, 1996; Kovchegov, 1999) and its finite-N_c generalization (Jalilian-Marian *et al.*, 1997, 1998a,b). The former can be solved using standard methods for integro-differential equations, while the latter, being a functional equation, can be solved by means of lattice-QCD methods, after reformulation as an Langevin equation (Rummukainen and Weigert, 2004).

The two equations are both nonlinear and lead to a saturation scale which signals the strong process of recombination of gluons and gluon saturation. Both equations describe the perturbative evolution of Wilson lines; therefore, they are valid strictly in the perturbative regime of QCD. However, one needs to regulate the nonperturbative large sizes of the Wilson lines, which are eventually probed during the evolution. This is one of the limitations of the approach. It would be of great advantage to further develop the lattice-QCD approach to attack the small-x behaviour of the gluon PDF.

II.1.2. Nuclear PDFs

Should the unpolarized hard-scattering processes occur off nuclei instead of free nucleons, it is customary to assume that they can still be described in terms of factorization theorems (Barshay *et al.*, 1975). Nuclear effects are then reabsorbed into PDFs, which differ from the unpolarized PDFs discussed in the previous section, and which are called nuclear PDFs. Recent progress in the phenomenological determination of nuclear PDFs has been mainly driven by the availability of hard probes in proton-lead collisions at the LHC. Representative examples of such processes include dijet (Eskola *et al.*, 2019) and D-meson production (Kusina *et al.*, 2018) to constrain the gluon nuclear PDFs at small and large x, respectively, and W, Z production to constrain nuclear modifications to quark flavor separation (Kusina *et al.*, 2017). These observables complement the existing information from neutral-current and charged-current DIS structure functions as well as from proton-lead collision data from RHIC (see Ref. (Ethier and Nocera, 2020) for an overview). Several other processes could be added to global nuclear PDF fits in the future, such as photon production (Campbell *et al.*, 2018), low-mass DY, and possibly even top-quark pair production.

Several groups have presented phenomenological determinations of nuclear PDFs. These differ in the input data set, in the accuracy of the theoretical computations, in the flavor assumptions, and in the methodological details of the analysis, such as the parametrization of the nucleus dependence, and the representation of uncertainties. The nuclear-PDF analysis including the most extensive data set to date is EPPS16 (Eskola *et al.*, 2017), which is the only one to take into account jet- and W, Z-production data from proton-lead collisions at the LHC. Other recent nuclear PDF sets, based on a more limited data set than EPPS16, are nCTEQ15 (Kovarik *et al.*, 2016), TuJu19 (Walt *et al.*, 2019), and nNNPDF1.0 (Abdul Khalek *et al.*, 2019a).

We refer the interested reader to Refs. (Ethier and Nocera, 2020; Kovařík *et al.*, 2019) for a detailed comparison of all of these nuclear PDF sets. Here, we note that the determination of nuclear PDFs is less advanced than that of their free-proton counterparts at least in four respects. First, the limited amount of experimental measurements, which results in large uncertainties on nuclear PDFs, especially for the gluon and the individual quark flavors. Second, the use, to some extent, of model-dependent assumptions, in particular to mimic shadowing and anti-shadowing effects as a function of x and of the atomic number A. Third, the consistency between nuclear PDFs and their $A = 1$ limit (that is, the free-proton PDFs) both in terms of central values and uncertainties, as well as the treatment of correlations between nuclear and proton PDFs. Fourth, possible data inconsistencies, for example between neutral- and charged-current structure functions and between some of the LHC observables.

Future facilities, specifically the EIC, will address the first of these limitations by extending the kinematic reach of the measurements down to $x \sim 10^{-9}$, as anticipated in several impact studies (Abdul Khalek *et al.*, 2019a; Aschenauer *et al.*, 2017; Paukkunen, 2018). Reliable calculations from lattice QCD could add valuable information to address some of the remaining limitations. The calculation of nuclear PDFs using lattice QCD is in general more demanding than the computation of free-proton PDFs, in a way that grows with the number of nucleons in the nucleus. For this reason, only few pioneering results on very light nuclei are currently available. In particular, the NPLQCD collaboration computed the first moment of the unpolarized gluon distribution in nuclei up to $A = 3$ (Winter *et al.*, 2017) (for deuteron and ^{3}He). These results are obtained at a higher-than-physical quark mass; as such, they should be viewed as a starting point for future developments.

II.1.3. Helicity PDFs

Helicity PDFs describe the net amount of momentum densities of partons aligned along or opposite a longitudinally polarized nucleon. Their relevance is related to the fact that the contribution of quarks, antiquarks and gluons to the nucleon spin is quantified by the first moments of the corresponding helicity PDFs, according to the canonical decomposition of the proton's total angular momentum (Leader and Lorcé, 2014).

The most recent analyses of polarized PDFs are DSSV14 (de Florian *et al.*, 2014), NNPDFpol1.1 (Nocera *et al.*, 2014) and JAM17 (Ethier *et al.*, 2017). Since publication, the DSSV14 analysis was updated with a Monte-Carlo variant (De Florian *et al.*, 2019), which also studied the impact of recent dijet measurements from STAR (Adam *et al.*, 2018; Adamczyk *et al.*, 2017). The NNPDFpol1.1 PDF set was also updated with STAR measurements, including the same dijet measurements and additional W-boson production data (Nocera,
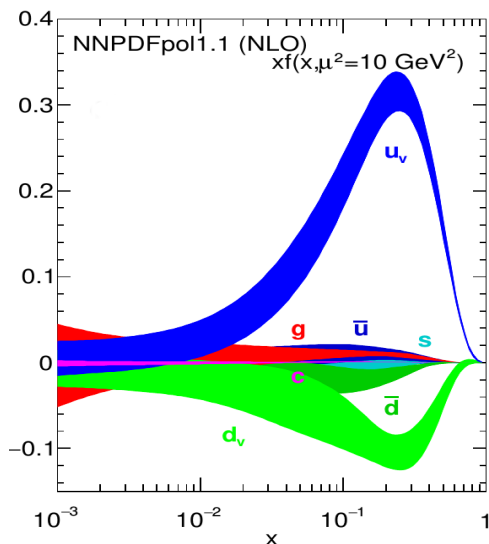
FIG. 5 The helicity PDFs from the NNPDFPOL1.1 parton set at $\mu^2 = 10$ GeV^2. Figure from (Tanabashi *et al.*, 2018).

2017). The JAM17 analysis is unique in its kind, because it realises a universal fit, that is, a simultaneous determination of the helicity PDFs and of the FFs of pions and kaons by means of an analysis of the SIDIS data. Because of this fact, theoretical assumptions on the SU(N_f) symmetry, which relate the first moments of the isotriplet and octet helicity PDF combinations to the weak decays of hadrons, can be relaxed. Therefore, theoretical bias in the determination of helicity sea-quark distributions is alleviated, in particular on strangeness (see Sect. II.3.3).

All of these analyses are accurate to NLO. The PDFs from the NNPDFPOL1.1 sets are displayed, at a scale $\mu^2 = 10$ GeV^2 in Fig. 5 for illustration purposes. The up quark valence distribution is the most constrained helicity PDF, primarily thanks to measurements of the proton structure function g_1 over a relatively broad range of x and Q^2; see Fig. 1. The corresponding down-quark distribution, which is opposite in sign, is smaller in magnitude and shows somewhat larger uncertainties. Nevertheless, a fair agreement between various PDF sets has been achieved for the valence polarizations, with differences originating from theoretical, experimental, and methodological choices generally being smaller than the PDF uncertainty (representing the uncertainty of the data). The polarization of the sea quarks is significantly smaller than the polarization of the valence quarks. It is also more dependent on the measurements included in each PDF set, and on the flavor assumptions with which the data are analyzed. Specifically, while all PDF sets show a fairly consistent anti-down polarization, the anti-up distribution is positive in the NNPDFPOL1.1 PDF set, due to W-boson production data, while it changes sign in the DSSV14 PDF

set, due to SIDIS data. This difference is somewhat relieved in the JAM17 result, where the simultaneous determination of helicity PDFs and FFs generally leads to PDFs with larger uncertainties. The situation is more involved for the strange helicity PDF, which remains largely unconstrained from DIS data alone (see Sect. II.3.3). Finally, the gluon helicity distribution has been established to be consistently sizable and positive in both the DSSV14 and NNPDFPOL1.1 analyses thanks to the availability of precise jet, dijet, and pion-production spin-asymmetry measurements at RHIC. Such evidence, however, is limited to the region $0.02 \lesssim x \lesssim 0.4$, outside of which the gluon helicity PDF is affected by large extrapolation uncertainties that prevent any definitive conclusion about its role in the proton spin decomposition. The extended kinematic region attained by a future polarized EIC (see Fig. 1) will be pivotal to clarify this picture, as demonstrated by several impact studies (Aschenauer *et al.*, 2013, 2012, 2015; Ball *et al.*, 2014).

II.1.4. Transversity PDFs

Transversity describes the correlation between the transverse polarizations of the nucleon and of its constituent partons. Because of its chiral-odd nature, it can be measured only in processes where it pairs to another chiral-odd object (Artru and Mekhfi, 1990; Jaffe and Ji, 1991). Historically, transversity was extracted for the first time in the framework of TMD factorization, by exploiting the Collins effect (Anselmino *et al.*, 2007) in SIDIS measurements, whereby transversity couples to the chiral-odd Collins FF $H_1^\perp$ (Collins, 1993). This procedure may be prone to theoretical bias, because TMD evolution depends on nonperturbative parameters that are not very well constrained by experiment. Furthermore, it cannot be extended to pp collision measurements, for which TMD factorization is explicitly broken (Rogers and Mulders, 2010). This limitation can be overcome by considering the Collins effect for a hadron detected inside a jet (Adamczyk *et al.*, 2018). A hybrid framework can be established (Kang *et al.*, 2017), where the TMD FF $H_1^\perp$ is paired to the collinear PDF h_1.

An alternative method was proposed to determine transversity in a fully collinear framework: it is based on the semi-inclusive production of two hadrons inside the same current jet with small invariant mass (Bianconi *et al.*, 2000; Jaffe *et al.*, 1998). The elementary mechanism consists in the correlation between the transverse polarization of the quark directly fragmenting into the two hadrons and their transverse relative momentum (Collins and Ladinsky, 1994). In this case, the dihadron SIDIS cross section (once integrated over partonic transverse momenta) contains a specific azimuthal modulation in the orientation of the plane

containing the momenta of the two hadrons. The coefficient of this modulation is the simple product $h_1 H_1^{\triangleleft}$, where $H_1^{\triangleleft}$ is a chiral-odd dihadron FF (DiFF) quantifying the above correlation (Bacchetta and Radici, 2003; Bianconi *et al.*, 2000; Radici *et al.*, 2002). The function $H_1^{\triangleleft}$ can be independently determined from correlations between the azimuthal orientations of two hadron pairs in back-to-back jets produced in electron-positron annihilation (Bacchetta *et al.*, 2009; Boer *et al.*, 2003; Courtoy *et al.*, 2012; Matevosyan *et al.*, 2018). Because of collinear factorization, it is possible to isolate the same combination $h_1 H_1^{\triangleleft}$ also in pp collisions (Bacchetta and Radici, 2004), a fact that gives rise to an asymmetric azimuthal distribution of the final hadron pair when one of the two initial protons is transversely polarized (Radici *et al.*, 2016).

Experimental measurements of the asymmetric azimuthal distribution of $\pi^+ \pi^-$ pairs in SIDIS have been collected by the HERMES collaboration for a proton target (Airapetian *et al.*, 2008) and by the COMPASS collaboration for both proton and deuteron targets (Adolph *et al.*, 2012, 2014), summing up to 22 independent data points. The azimuthal asymmetry in the distribution of back-to-back $\pi^+ \pi^-$ pairs in $e^+ e^-$ annihilation was firstly measured by the BELLE collaboration (Vossen *et al.*, 2011), a fact that opened the way to the first parametrization of $H_1^{\triangleleft}$ (Courtoy *et al.*, 2012). In turn, this result was used in combination with the SIDIS data to extract the valence components of h_1 (Bacchetta *et al.*, 2011, 2013; Radici *et al.*, 2015) at leading-order (LO) accuracy. The STAR collaboration recently released results for the predicted asymmetry of $\pi^+ \pi^-$ pairs produced from pp collisions with a transversely polarized proton at the center-of-mass energy of $\sqrt{s} = 200$ GeV (Adamczyk *et al.*, 2015). The first extraction of transversity from a global analysis of all of these data sets was, therefore, carried out in Ref. (Radici and Bacchetta, 2018) at LO, where the bootstrap method (Bacchetta *et al.*, 2013; Radici *et al.*, 2015) was used to propagate the data uncertainty into the PDF uncertainty. We will call this analysis PV18 in the remainder of the paper. The STAR collaboration subsequently released measurements at $\sqrt{s} = 500$ GeV (Adamczyk *et al.*, 2018), that need to be included in future updates of the fit. The overall experimental information amounts to approximately 50 independent data points covering the range $0.008 < x < 0.35$, about two orders of magnitude less than for the analysis of unpolarized PDFs, see Fig. 1.

From the theoretical point of view, the decomposition on the helicity basis of the quark-hadron helicity amplitude in terms of the three leading-twist PDFs (unpolarized, helicity and transversity) leads to the so-

called Soffer inequality (Soffer, 1995)

$$|h_1^q(x, Q^2)| \leq \frac{1}{2} \left[q(x, Q^2) + \Delta q(x, Q^2) \right] = F_{SB}^q(x, Q^2) , \tag{2}$$

for each quark q and antiquark $\bar{q}$ separately. For valence quarks $q_v = q - \bar{q}$, the Soffer inequality reads

$$|h_1^{q_v}| \leq F_{SB}^q + F_{SB}^{\bar{q}} \equiv F_{SB}^{q+\bar{q}} , \tag{3}$$

and is conserved under QCD evolution (Goldstein *et al.*, 1995; Vogelsang, 1998). Because the experimental data cover a limited range in x, Eq. (3) is a bound that limits the allowed parameter space in any reliable determination of transversity.

The global analysis of Ref. (Radici and Bacchetta, 2018) assumed the following functional form at the initial scale $Q_0^2 = 1$ GeV^2:

$$x h_1^{q_v}(x, Q_0^2) = F^q(x) \, F_{SB}^{q+\bar{q}}(x, Q_0^2) , \tag{4}$$

where $F^q(x)$ contained five fitting parameters for each valence flavor q_v. Imposing the constraint $|F^q(x)| \leq 1$ for all x automatically enforces the Soffer inequality at any scale. The low-x behavior of $h_1^{q_v}(x)$ was further constrained by requiring that its zeroth Mellin moment, the tensor charge, is finite. The MSTW08 (Martin *et al.*, 2009) and DSSV08 (de Florian *et al.*, 2009) parton sets were used as input for the unpolarized (at LO) and the helicity (at NLO) PDFs entering Eq. (3). Using other parametrizations, for instance CT18 (Hou *et al.*, 2019b) for the unpolarized PDF, or JAM15 (Sato *et al.*, 2016) or JAM17 (Ethier *et al.*, 2017)) for the helicity PDF, was shown to leave the fit of the transversity unaltered (Benel *et al.*, 2020; Radici and Bacchetta, 2018).

The dependence of the transversity PDF on the Soffer bound implicit in Eq. (4) may result in a saturation of said bound at large x. If so, one may wonder whether the data is in tension with the bound itself, or whether the account of the Soffer bound is not flexible enough. This issue was investigated in the fit of Ref. (Benel *et al.*, 2020), which we call MEX19, based only on SIDIS dihadron production data and on the bootstrap method. Four functional forms were considered, all consisting of sums of selected Bernstein polynomials of four different degrees that spanned almost the entire x range and that were multiplied by $x^{1.25}$. An estimate of the statistical compatibility between the valence transversity distributions and the bound was performed through the reweighting of the data in the minimization procedure. Given the uncertainty on the deuteron data, the $h_1^{d_v}$ had to be constrained to an envelope designed based on the fall-off of PDFs at large x using the Lagrange multiplier method.

In Fig. 6 we show $x \, h_1(x)$ at $Q^2 = 2.4$ GeV^2. The upper (lower) panel refers to its valence up (down) component. The shaded (pink) band is the result of the PV18 global fit of Ref. (Radici and Bacchetta,
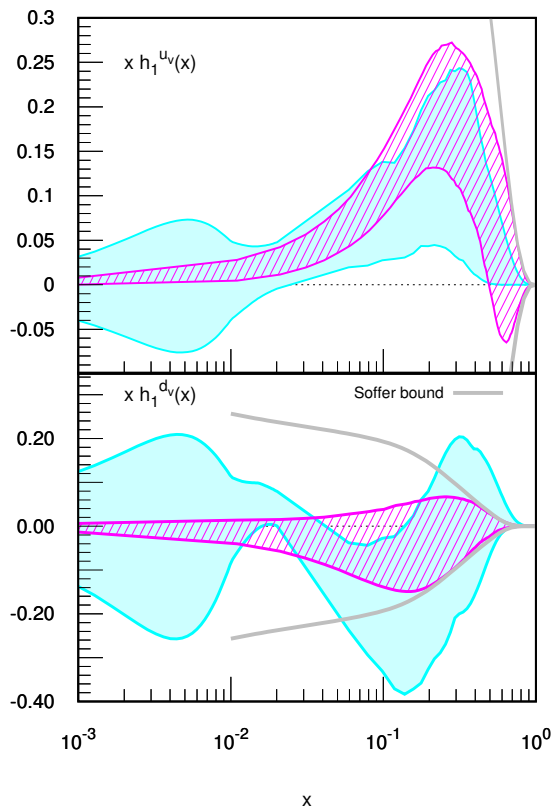
FIG. 6 The transversity $x\,h_1(x)$ at 90% CL. Upper (lower) plot for valence up (down) component. Gray lines represent the Soffer bound. Darker (pink) band for the PV18 global fit of (Radici and Bacchetta, 2018) at $Q^2 = 2.4$ GeV^2. Lighter (cyan) band for the MEX19 constrained analysis of (Benel et al., 2020) at the average scale of the data.

2018). The error band corresponds to the 90% confidence level (CL), and includes also a systematic theoretical error induced by the currently unconstrained gluon contribution to DiFF (Radici and Bacchetta, 2018). It turns out that the transversity for the valence down quark is very sensitive to this uncertainty. The plain (cyan) band is the result of the MEX19 constrained fit of Ref. (Benel et al., 2020); error bands correspond to the 90% CL. The Soffer bound is represented in a limited range by a gray line using the unpolarized and helicity PDFs from the LO MSTW08 (Martin et al., 2009) and the NLO DSSV08 (de Florian et al., 2009) sets, respectively. At small x, the error on the bound (still negligible in comparison to the current overall uncertainties on the transversity PDF) increases due to the uncertainties in both parametrizations. This is, however, inconsequential for valence distributions, which are suppressed by evolution. From Fig. 6 we observe that the two determinations are consistent within uncertainties, although the larger uncertainty on the valence down quark at large x can be appreciated in the fit of Ref. (Benel et al., 2020) as a consequence of the Soffer bound.

Nevertheless, PDF shapes and uncertainties are comparable to those determined in TMD analyses of the Collins effect (Anselmino et al., 2013; Kang et al., 2016), including in a dedicated studies on the role of the Soffer bound on the tensor charge (D'Alesio et al., 2020). The Soffer bound was completely released in (Cammarota et al., 2020). In all cases, the uncertainty bands remain large; future developments will depend on a detailed study of flavor dependence of DiFFs by using BELLE data for dihadron multiplicities (Seidl et al., 2017), and on including in the global fit also the STAR data at higher center-of-mass energy (Adamczyk et al., 2018). From the theoretical point of view, work is in progress to update the analyses to NLO accuracy.

II.2. Lattice PDFs Updates

Lattice QCD regularizes QCD on a finite Euclidean lattice by means of numerical computations of QCD correlation functions in the path-integral formalism, using methods adapted from statistical mechanics. Of particular interest for this report, are novel methods to access information on PDFs using lattice QCD. This is a very challenging task, as distribution functions are light-cone quantities and cannot be calculated on a Euclidean lattice. A few methods have been proposed, some as early as the 1990s, and others very recently. This includes, studies based on the hadronic tensor (Liu, 2000; Liu and Dong, 1994; Liu et al., 1999), auxiliary quark field approaches (Braun and Müller, 2008; Detmold and Lin, 2006), Large-Momentum Effective Theory (LaMET) (Ji, 2013, 2014; Ji et al., 2020) (quasi-PDFs), pseudo-PDFs (Radyushkin, 2017a), a method based on OPE (Chambers et al., 2017), and the Good Lattice Cross Sections approach (Ma and Qiu, 2015, 2018a,b). We refer the reader to Ref. (Cichy and Constantinou, 2019; Ji et al., 2020; Lin et al., 2018d) for a thorough description of the methods. In this section we review recent progress on some of these methods that have been studied extensively within lattice QCD. The current stage of the field and the limited data for some methods, does not permit one to quantitatively compare the lattice results extracted from different methods. Having more data, in particular simulations at the physical point, will improve the current understanding of the sources of systematic uncertainties. This way, we can assess what are the cavities and technical limitations of each method, such as, the region of x for which the lattice results are reliably extracted.

II.2.1. PDFs at the physical point with quasi-distributions

Pioneering works have shown great promise in obtaining quantitative results for the unpolarized,

helicity and transversity quark and antiquark distributions (Alexandrou *et al.*, 2014, 2015; Chen *et al.*, 2016; Lin, 2014a,b; Lin *et al.*, 2015) using the quasi-PDFs approach (Ji, 2013), which utilized Large Momentum Effective Theory (LaMET) (Ji, 2014) to match lattice calculable matrix elements, to their light-cone counterparts. The groups working on extracting x-dependent PDFs from lattice QCD have significantly improved their calculations. A recent review on the theory and lattice calculations can be found in Refs. (Cichy and Constantinou, 2019; Ji *et al.*, 2020). There are several theoretical developments related to the renormalizability of quasi-PDFs (Chen *et al.*, 2017; Ishikawa *et al.*, 2016; Ji and Zhang, 2015; Ji *et al.*, 2017, 2018), and the appropriate matching formalism (Izubuchi *et al.*, 2018; Stewart and Zhao, 2018; Xiong *et al.*, 2014). One of the major developments for the lattice calculation concerns the understanding of the renormalization pattern on the lattice (Chen *et al.*, 2019a; Constantinou and Panagopoulos, 2017), as well as the development of a complete nonperturbative renormalization procedure (Alexandrou *et al.*, 2017a; Chen *et al.*, 2018a) that removes all divergences of nonlocal operators.

The first unpolarized PDFs at the physical pion mass (Alexandrou *et al.*, 2018a; Lin *et al.*, 2018a) using the quasi-PDFs approach were determined using small momentum. This, in addition with the challenges in the reconstruction of the x dependence, may lead to the wrong sign of sea-flavor asymmetry to be seen following Fourier transformation. The upper plot of Fig. 7 shows the newer PDF results on ensembles at the physical pion mass with momenta above 2 GeV, and then renormalized at 3 GeV (Lin *et al.*, 2018b) (denoted as matched PDF). The associated error band includes systematic errors coming from variations in the renormalization scale, from the choice of zP_z in the Fourier transform, from an estimation of lattice-spacing and finite-volume effects, from other nucleon matrix corrections, and from approximations made in the matching formula. As expected from the Fourier-transform study, the sea-flavor asymmetry is recovered with increased momentum. In the positive isovector quark region, the lattice results agree with CT14 (Dulat *et al.*, 2016), which is consistent with NNPDF3.1 (Ball *et al.*, 2017) and CJ15 (Accardi *et al.*, 2016a), up to the small-x region, where even larger zP_z data are required for lattice calculations to have control over these regions. The middle plot of Fig. 7 shows LP^3's isovector quark helicity PDF (Lin *et al.*, 2018b) matched in the $\overline{\text{MS}}$-scheme at the scale $\mu = 3$ GeV, extracted from LaMET at the largest proton momentum (3 GeV). The inner band denotes the statistical error, while the outer band also includes systematic uncertainties similar to those determined in the case of unpolarized PDFs. The lattice result is compared to two phenomenological fits,

NNPDFpol1.1 (Nocera *et al.*, 2014) and JAM17 (Ethier *et al.*, 2017). The bottom plot in Fig. 7 shows the LP^3's proton isovector transversity PDF (Liu *et al.*, 2018) at the renormalization scale $\mu = \sqrt{2}$ GeV ($\overline{\text{MS}}$ scheme), extracted from lattice QCD and LaMET at $P_z = 3$ GeV. The error band includes statistical errors (which fold in the excited-state uncertainty) and the same systematics mentioned in the unpolarized PDF case. The lattice result is compared to global fits by JAM17 and LMPSS17 (Lin *et al.*, 2018c).

The ETMC Collaboration has also improved their calculations of PDFs, and refined the matching procedure by proposing a modified $\overline{\text{MS}}$ scheme, which satisfies particle number conservation. Note that this scheme corresponds to the quasi-PDFs, while the light-cone PDFs (see Eq. (1)) are always renormalized in the $\overline{\text{MS}}$ scheme. The modified $\overline{\text{MS}}$ scheme was applied to the unpolarized and helicity PDFs in Ref. (Alexandrou *et al.*, 2018b) and for the transversity PDF. The latter was presented for the first time at the physical point in Ref. (Alexandrou *et al.*, 2018c). The ensemble used has $N_f = 2$ twisted-mass fermions with clover improvement (Abdel-Rehim *et al.*, 2017). The ensemble has a lattice spacing 0.093 fm, lattice spatial extent 4.5 fm, and pion mass 130 MeV. Three values were used for the momentum boost: 0.83, 1.11, and 1.38 GeV. In this work, increasing the momentum to values higher than 1.5 GeV led to an unreliable extraction of the ground state. The final PDFs are displayed in Fig. 7 at scale 1.38 GeV and are compared with a selection of results from global fits. The unpolarized PDF has slope similar to the phenomenological one in the positive-x region, but lies above it. The lattice results for the helicity PDF are compatible with phenomenological PDFs for $x \lesssim 0.4$–0.5. The lattice result for the transversity PDF is in agreement with the global fits, as well as with those constrained using the lattice determination of the tensor charge as input, for $x \lesssim 0.4$–0.5. Interestingly, the statistical accuracy of the aforementioned lattice results is better than either phenomenological determination.

Furthermore, ETMC studied several sources of systematic uncertainties directly at the physical point (Alexandrou *et al.*, 2019d). This is essential, because the pion mass dependence is sizable for the nonlocal matrix elements (see, for example, Fig. 6 of Ref. (Alexandrou *et al.*, 2018b)). All sources of systematic uncertainties that can be studied were included in Ref. (Alexandrou *et al.*, 2019d), that is: excited-state contamination, renormalization, reconstruction of the x-dependence, effects of truncating the Fourier transform, and different matching prescriptions. This in-depth study revealed that excited-state contamination is not negligible for fast-moving nucleons and should be properly reduced. The work also demonstrated that the discrete and limited
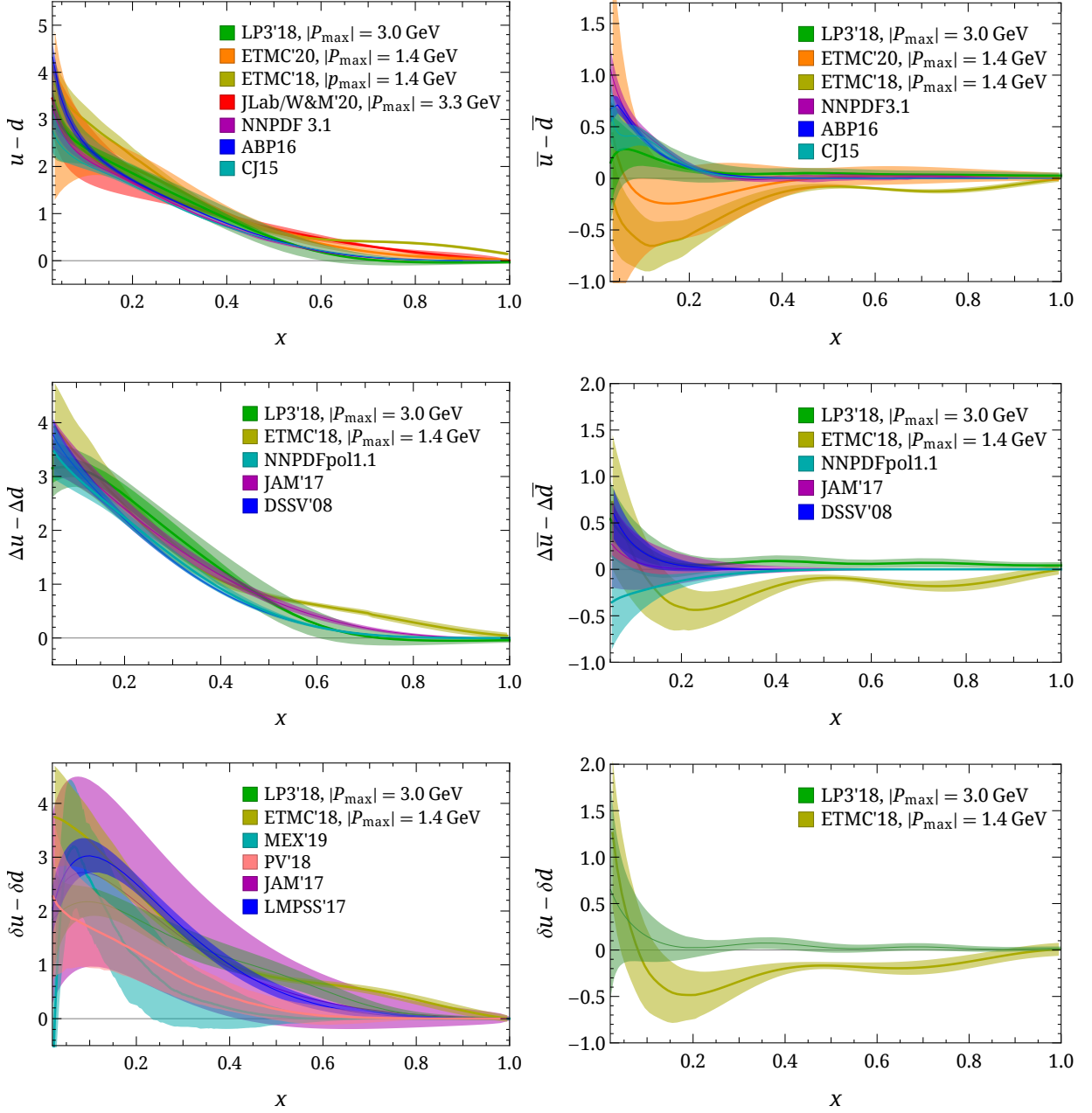
FIG. 7 Summary of the lattice calculation of isovector unpolarized (top), helicity (middle) and transversity (bottom) with LP^3 and ETMC isovector quark (left column) and antiquark (right column) taken from (Alexandrou *et al.*, 2019d, 2018b,c; Bhat *et al.*, 2020; Chen *et al.*, 2018b; Lin *et al.*, 2018b; Liu *et al.*, 2018), JLab/W&M valence unpolarized distribution results from (Joó *et al.*, 2020), and global fits from (Accardi *et al.*, 2016a; Alekhin *et al.*, 2017; Ball *et al.*, 2017) (unpolarized), (Ethier *et al.*, 2017; de Florian *et al.*, 2009; Nocera *et al.*, 2014) (helicity), and (Benel *et al.*, 2020; Lin *et al.*, 2018c; Radici and Bacchetta, 2018) (transversity). Note that none of the current lattice calculations have taken the continuum limit ($a \to 0$) and have remaining lattice artifacts (such as finite-volume effects); disagreement in the obtained distributions is not unexpected.

number of data for nonzero z are not sufficient for a reliable reconstruction of the x-dependence of PDFs. Antiquarks were particularly affected, because the sign of the sea asymmetry is highly prone to systematic uncertainties.

The first study of systematic uncertainties arising

from finite-volume effects for the quasi-distributions was reported in Ref. (Lin and Zhang, 2019) using a 220-MeV pion mass with $M_\pi^{\mathrm{val}} L \approx 3.3$, 4.4 and 5.5, respectively. After a careful extraction of the bare matrix elements for the unpolarized and polarized distributions (see the right-hand side of Fig. 8), no volume dependence was

Ref.	Sea quarks	Valence quarks	$N_{\Delta t}$	method	$P_{\max}$ (GeV)	a (fm)	M_π (MeV)	$M_\pi L$
ETMC'20	2f twisted mass	twisted mass	4	pseudo-PDF	1.38	0.09	130	3.0
JLab/W&M	2+1 clover	clover	n/a	pseudo-PDF	3.29	0.09	172–358	5.08–5.47
ETMC'18	2f twisted mass	twisted mass	4	quasi-PDF	1.38	0.09	130	3.0
LP3'18	2+1+1f HISQ	clover	4	quasi-PDF	3	0.09	135	4.0
LP3'17	2+1+1f HISQ	clover	2	quasi-PDF	1.3	0.09	135	4.0

TABLE I The lattice parameters used in calculations of x-dependent PDFs near or extrapolated to physical pion mass. $N_{\Delta t}$ indicates the number of source-sink separation used in the lattice calculation to control the excited-state systematics which can be significant for nucleon structure. The work of the JLab/W&M (Joó *et al.*, 2020) group uses the Feynman-Hellmann theorem, where the matrix elements are extracted from two-point–like lattice correlators, and $N_{\Delta t}$ does not apply in their approach. The references for each work are as follows: ETMC'20 (Bhat *et al.*, 2020), JLab/W&M (Joó *et al.*, 2020), ETMC'18 (Alexandrou *et al.*, 2019d, 2018b,c), LP3'18 (Chen *et al.*, 2018b; Lin *et al.*, 2018b; Liu *et al.*, 2018), LP3'17 (Lin *et al.*, 2018a).
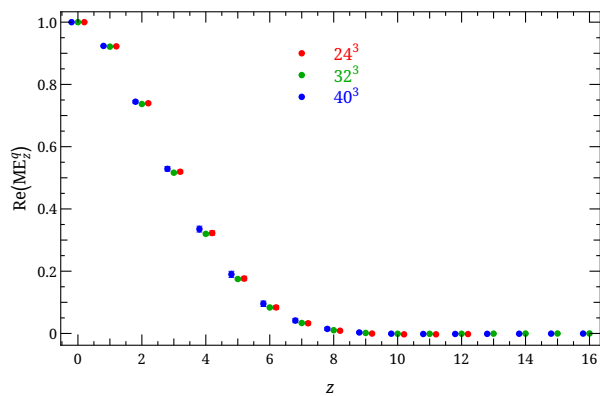

FIG. 8 The normalized isovector nucleon matrix elements for unpolarized PDFs $P_z \approx 1.3$ GeV as functions of z at the three volumes ($M_\pi L = 3.3$, 4.4 and 5.5 indicated by red, green and blue, respectively) (Lin and Zhang, 2019).

observed in these ensembles within the statistical error. It was therefore concluded that finite-volume dependence does not play a significant role for the boosted nucleon matrix elements ($P_z \approx 1.3$ GeV larger) used for quasi-distributions within the range $M_\pi^{\mathrm{val}} L \in \{3.3, 5.5\}$.

To calculate the small-x ($x < 0.01$) behavior of the PDFs using existing lattice x-dependent methods, one needs to pursue boost momenta P_z an order of magnitude higher than those currently being used. The minimum x obtainable from lattice QCD is connected to the product of the length of the Wilson line and momentum boost, zP_z. It is also expected that the size of the momentum boost is connected to the reliability of the lattice results in the various x regions. For example, higher values of P_z result in fast decay of the matrix elements, and therefore, the truncation of the maximum value of z in the Fourier transform matters less. There are a number of proposals to avoid to Fourier transformation by working in position space; this would work in an ideal world where there is arbitrarily precise data throughout the large-zP_z region. However, in reality, the lattice data taken in the small-zP_z region are not precise enough to even discern whether the parton distribution is flat across

all x; one loses sensitivity to very distinct distributions in x-space, which appear very similar in zP_z space. Furthermore, one still needs large boost momenta zP_z to reliably obtain the distribution in the small-x region, and very fine lattice spacing, $a < 0.02$ fm to reduce the lattice discretization systematic error that goes like $(P_z a)^n$. There have been some exploratory studies of how to get around the problem: Ref. (Zhang *et al.*, 2020a) applied machine-learning algorithms to make predictions for different types of lattice LaMET data, such as kaon PDFs, meson distribution amplitudes and gluon PDFs. The data correlation and predictions of higher momenta and their dependence on the amount of training and bias-correction data, and machine-learning model parameters were studied in great detail. More studies done in this direction are mandatory to revolutionize the investigation of the small-x nucleon structure.

II.2.2. PDFs at the physical point with pseudo-distributions

Besides quasi-PDFs, additional novel methods have been proposed for the extraction of lightcone distributions (Aglietti *et al.*, 1998; Bali *et al.*, 2018; Braun and Müller, 2008; Chambers *et al.*, 2017; Detmold *et al.*, 2018; Detmold and Lin, 2006; Liang *et al.*, 2019; Liu and Dong, 1994; Ma and Qiu, 2018a,b; Sufian *et al.*, 2019). One of these methods is the so-called pseudo-distributions approach, originally proposed by Radyushkin (Radyushkin, 2017a,b, 2018a, 2017c, 2018b, 2019a,b,c). The raw data are the same as in the quasi-PDFs approach, but the analysis differs in several ways. In the pseudo-PDFs approach, the matrix elements are expressed in terms of z^2 and of the Ioffe time (Ioffe, 1969) $\nu \equiv -p \cdot z$ (where p is the nucleon momentum boost), and are called Ioffe-time distributions. One of the main differences between quasi- and pseudo-PDFs is the reconstruction of the x-dependence of the distributions: quasi-PDFs are defined as the Fourier transform of the matrix elements in z, while pseudo-PDFs as the transform in Ioffe time. As a consequence, pseudo-distributions have only canonical

support ($x \in [-1 : 1]$), while quasi-PDFs are allowed to be nonzero outside the canonical x-range. Another major difference of practical value is that the Ioffe time can increase by either increasing z or p. Thus, lattice data at small values of the momentum boost are also desirable.

The pseudo-distribution approach was investigated on the lattice soon after it was proposed. The valence unpolarized PDF of the nucleon was studied first in the quenched setup (Orginos *et al.*, 2017), and later using dynamical simulations at $m_\pi = 400$ MeV (Joó *et al.*, 2019a). The pion PDFs were also studied in Ref. (Joó *et al.*, 2019b). Other work related to the pseudo-PDFs approach on the lattice can be found in Ref. (Karpie *et al.*, 2019, 2018). A recent calculation including an ensemble near physical pion mass (170 MeV) is presented in Ref. (Joó *et al.*, 2020). The maximum value of P_3 used for the ensembles with pion mass 358, 278, and 179 MeV is 2.46, 3.29, and 2.12 GeV, respectively. In Fig. 7 we show the valence PDF extrapolated to the physical pion mass using the aforementioned ensembles, as explained in Ref. (Joó *et al.*, 2020). It is important to emphasize that, unlike the case of quasi-PDFs, the final PDFs do not rely on a sole value of P_3. The relevant parameter for the reconstruction of the PDFs is the Ioffe time, which can be increased by increasing either z or P_3. Typically, the data at large P_3 are more noisy, and, therefore, do not drive the values of the final PDFs. The lattice results are compared to various determinations from global fits. The agreement of the former with the latter is excellent in the region $x < 0.25$, while it deteriorates at large x. This discrepancy may be due to an underestimation of systematic uncertainties in the lattice result, which deserves further investigation.

Another notable lattice calculation using the pseudo-distribution approach, with simulations directly at the physical point, was presented in Ref. (Bhat *et al.*, 2020). A novel aspect is the extraction not only of the valence distribution $q_v(x)$, but also of the combination with antiquarks $q_v(x) + 2\bar{q}(x)$. This led to the extraction of the total and sea-quark distributions, $q(x) = q_v(x) + \bar{q}(x)$ and $q_s(x) = \bar{q}(x)$. The lattice results are presented in Fig. 7. The purple band represents the statistical uncertainties of the lattice result, and the cyan band the combination of statistical and systematic uncertainties. Some of these uncertainties were computed explicitly (for example, the reconstruction of the x-dependence), while others (for example, for volume and discretization effects) an estimate was given, see Ref. (Bhat *et al.*, 2020) for details. The lattice result is compared to a global fit of unpolarized PDFs, NNPDF3.1, with which it is in very good agreement. This fact demonstrates that a realistic determination of unpolarized PDFs from the lattice is possible.
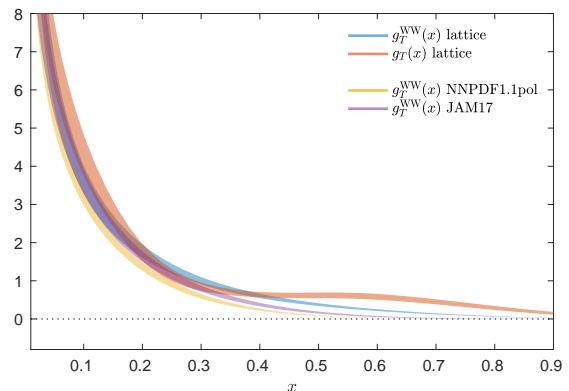

FIG. 9 Comparison of $g_T(x)$ from lattice (red band) with its WW approximations: lattice-extracted g_T^{WW} (blue band) and calculated from global fits (NNPDF1.1pol (Nocera *et al.*, 2014) orange band, JAM17 (Ethier *et al.*, 2017) purple band). The proton momentum is $P_3 = 1.67$ GeV.

II.2.3. Twist-3 PDFs

A new direction is currently being pursued with lattice calculations of the x-dependence of twist-3 PDFs, which are important to characterize the structure of hadrons beyond the leading twist (they contain information on quark-gluon-quark correlations (Balitsky and Braun, 1989; Kanazawa *et al.*, 2016)). The first calculation was completed recently (Bhattacharya *et al.*, 2020a) for the twist-3 $g_T(x)$ distribution, including the computation of the one-loop matching kernel (Bhattacharya *et al.*, 2020b). The quasi-distribution approach is used with three values of the momentum boost (0.83, 1.25, and 1.67 GeV). The pion mass of the ensemble is 260 MeV. This calculation not only predicts the x-dependence of $g_T(x)$ but serves as a test of the Wandzura-Wilczek (WW) approximation (Wandzura and Wilczek, 1977). In this approximation, the twist-3 $g_T(x)$ distribution may be obtained from its twist-2 counterpart $g_1(x)$

$$g_T^{\mathrm{WW}}(x) = \int_x^1 \frac{dy}{y} g_1(y) \,. \tag{5}$$

In Ref. (Bhattacharya *et al.*, 2020a), g_T^{WW} is evaluated using the lattice data as a function of x, as shown in Fig. 9 for $P_3 = 1.67$ GeV. It is also compared to the actual data of $g_T(x)$, and is found to be consistent for a large range of x. The large-x region reveals some tension, which may be due to systematic uncertainties. It is also possible that this is an indication of violations of the WW approximation. It is also interesting to compare the lattice result with the WW approximation obtained using g_1 from global fits (Ethier *et al.*, 2017; Nocera *et al.*, 2014). Good agreement is observed up to $x \approx 0.3$, while the discrepancy for larger x values indicates possible systematic effects.

II.2.4. Gluon PDFs

The unpolarized gluon PDF is defined by the Fourier transform of the lightcone correlation in the hadron,

$$g(x, \mu^2) = \int \frac{\mathrm{d}y^-}{\pi x} e^{-ixy^- P^+} \times$$
$$\times \ \langle P|F_\mu^+(y^-)\mathcal{W}(y^-,0)F^{\mu+}(0)|P\rangle \ , \quad (6)$$

where $y^\pm = \frac{1}{2}(y^0 \pm y^3)$ is the spacetime coordinate along the lightcone direction, $|P\rangle$ is the hadron state with momentum $P_\mu = (P_0, 0, 0, P_z)$ and normalization $\langle P|P\rangle = 1$, μ is the renormalization scale, $F_{\mu\nu} = T^a G_{\mu\nu}^a = T^a(\partial_\mu A_\nu^a - \partial_\nu A_\mu^a - gf^{abc}A_\mu^b A_\nu^c)$ is the gluon field tensor, and $\mathcal{W}(y^-,0) = \mathcal{P}\exp(-ig\int_0^{y^-} \mathrm{d}\eta^- A^+(\eta^-))$ is the lightcone Wilson link from y^+ to 0 with A^+ as the gluon potential in the adjoint representation. Unfortunately, these time-separated and nonlocal operators cannot be directly calculated using lattice QCD.

In the first exploratory study which applied the quasi-PDF approach to the gluon PDFs (Fan *et al.*, 2018), ensembles with unphysically heavy quark masses were used. Since gluon quantities are much noisier than quark disconnected loops, calculations with very high statistics are necessary to reveal a signal. The calculations were done using overlap fermions on gauge ensembles with 2+1 flavors of domain-wall fermion and spacetime volume $24^3 \times 64$, $a = 0.1105(3)$ fm, and $M_\pi^{\mathrm{sea}} = 330$ MeV. The gluon operators were calculated for all volumes and high statistics: 207,872 measurements were taken of the two-point functions with valence quarks at the light sea and strange masses (corresponding to pion masses 340 and 678 MeV, respectively). The coordinate-space gluon quasi-PDF matrix element ratios are plotted in Fig. 10, and compared to the corresponding Fourier transform of the gluon PDF based on two global fits at NLO: the PDF4LHC15 combination (Butterworth *et al.*, 2016) and the CT14 set (Dulat *et al.*, 2016). Up to perturbative matching and power corrections $O(1/P_z^2)$, the lattice results are compatible with global fits within the statistical uncertainty at large z. The results at the lighter pion mass (at the unitary point) of 340 MeV are also shown in Fig. 10. These are consistent with those from the strange point but have larger uncertainties. The gluon quasi-PDFs in the pion were also studied for the first time in Ref. (Fan *et al.*, 2018) and features similar to those observed for the proton were revealed. Finally, there have been recent developments in improving the operators for the gluon-PDF lattice calculations (Balitsky *et al.*, 2019; Wang *et al.*, 2019b; Zhang *et al.*, 2019b), which will allow us to take the continuum limit for the gluon PDFs in future lattice calculations.
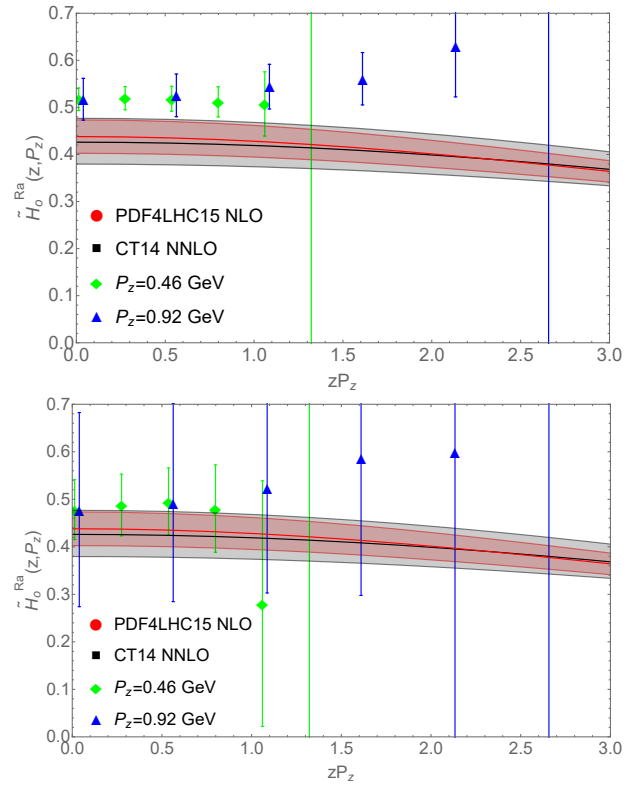

FIG. 10 The final results of gluon PDF matrix elements at 678 MeV (top) and 340 MeV (bottom) pion mass as functions of zP_z, compared with the FT of the gluon PDF from the global fits PDF4LHC15 (Butterworth *et al.*, 2016) and CT14 (Dulat *et al.*, 2016).

II.2.5. Hadronic Tensor

The hadronic tensor

$$W_{\mu\nu} = \frac{1}{4\pi} \int d^4z e^{iq\cdot z} \langle P, S \left| \left[J_\mu^\dagger(z)J_\nu(0) \right] \right| P, S\rangle \quad (7)$$

characterizes the nonperturbative nature of the nucleon in scattering processes involving nucleons such as DIS. It can be further decomposed into structure functions (Blumlein, 2013), which are commonly used to determine the PDFs in global fits through factorization theorems. A lattice calculation of the hadronic tensor provides a first-principle method to study PDFs as well as physical processes like the low-energy neutrino-nucleon scattering (Liang *et al.*, 2020, 2018a; Liu, 2000, 2016; Liu and Dong, 1994). This approach has several advantages. The hadronic tensor is scale independent, such that no renormalization is needed except for the finite lattice normalization, if local vector and axial currents are used for the lattice calculation. Furthermore, the structure functions are frame independent, therefore, no highly boosted nucleons are needed.

In the hadronic tensor approach, additional parton degrees of freedom are revealed graphically, among which, the connected sea (CS) antipartons which account
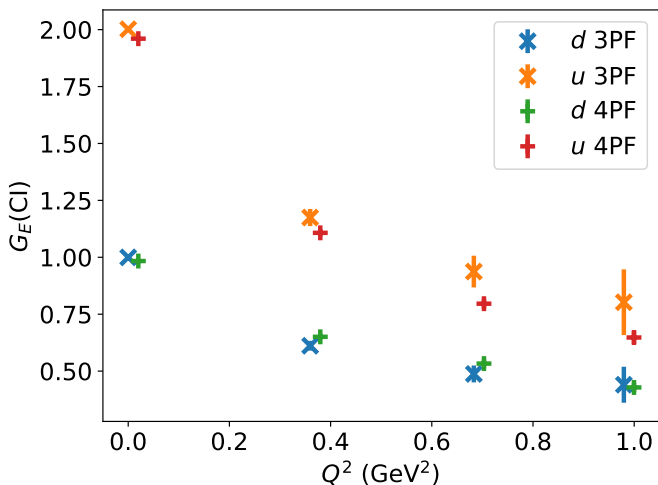
FIG. 11 The electric form factors (connected insertions only) calculated by means of normal 3-point functions (3PF) and 4-point functions (4PF) for both u and d quarks.

for the Gottfried sum-rule violation (Liu *et al.*, 2012; Liu and Dong, 1994). It is worthwhile pointing out that the quasi-PDF in the negative x region in the connected insertion is the CS antiparton in the hadronic tensor approach due to the fact that it is the antiparton in the connected insertion which is not affected by the gluon and disconnected sea (DS) distributions in evolution. Besides, in the practical lattice calculation, some diagrams (Wick contractions) contain only higher twist contributions, a fact that offers the possibility of studying higher twist effects on the lattice.

Numerically, a substantial challenge of this approach is to convert the hadronic tensor from the Euclidean space back to the Minkowski space, which involves solving an inverse problem of a Laplacian transform (Liang *et al.*, 2020, 2018a; Liu, 2016). In order to tackle this problem, three methods (i.e., the Backus-Gilbert method (Backus and Gilbert, 1968, 1970; Hansen *et al.*, 2017), the maximum entropy method (Asakawa *et al.*, 2001; Rietsch, 1977) and the Bayesian reconstruction method (Burnier and Rothkopf, 2013)) have been implemented and tested (Liang *et al.*, 2020, 2018a). It is believed that the Bayesian reconstruction method and its further improved version (Fischer *et al.*, 2018; Kim *et al.*, 2018) is the best method so far to solve the problem. On the other hand, the inverse problem is a common problem in PDF calculations, and can be simplified or avoided by using model-inspired fitting functions.

Another challenge of this approach is to access high momentum and energy transfers in such a way that the calculation can be extended into the DIS region. Numerical tests (Liang *et al.*, 2020) show that small lattice spacings are essential for this purpose. The need of fine lattices appears to be a common problem faced by the lattice PDF community. For the hadronic tensor

calculation, one important point is that it works in all the energy ranges (from elastic scattering to inelastic scattering and on to DIS). Before lattices with very fine spacing are available, the hadronic tensor can be used to study the nucleon elastic form factors and low-energy scatterings such as the neutrino-nucleon scattering which is of significant physical importance. Fig. 11 shows a numerical check of this approach in terms of form factors on the RBC-UKQCD 32Ifine lattice (Blum *et al.*, 2016). The structure function of the elastic scattering from the hadronic tensor, a 4-point function, is the product of the elastic nucleon form factors for the currents involved. Fig. 11 shows that the the electric form factors (connected insertions only) calculated by means of the 3-point functions for both u and d quarks are found to be consistent with errors with those deduced from the hadronic tensor.

This lays a solid foundation for further calculations. Currently, lattices with lattice spacing ~ 0.04 fm are suitable, for instance, to study the neutrino-nucleus scattering for DUNE experiments where the neutrino energy is between ~ 1 to ~ 7 GeV. At the same time, these lattices can also be used to explore the pion PDFs. In the future, working on lattices with lattice spacing of 0.03 fm or even smaller would be desirable for studying the nucleon substructure.

II.3. Intersection of Lattice and Global PDF Fits

In this Section, we review some aspects of potential interplay between lattice QCD computations and PDF fits. First, we update the benchmark of lattice QCD and global fit results for the lowest moments of unpolarized and helicity PDFs, in continuity with the previous (Lin *et al.*, 2018d), and extend it to transversity. Second, we investigate the usage of lattice QCD data in fits of unpolarized PDFs. Third, we discuss how lattice QCD computations can shed light on the poorly known unpolarized and helicity strange PDFs.

II.3.1. Moments

One of the main outcomes of the 2017 PDFLattice white paper was a detailed comparison between lattice QCD and global fit results for the (lowest) moments of unpolarized and helicity PDFs. Specifically, we identified a set of benchmark moments, we appraised the various results available for them in the literature, and we provided corresponding benchmark values for lattice QCD and global fits. In the following, we present an update of this exercise.

We consider the following benchmark moments of unpolarized, helicity and transversity PDFs, respectively

$$\langle x \rangle_{u^+ - d^+} , \quad \langle x \rangle_{u^+} , \quad \langle x \rangle_{d^+} , \quad \langle x \rangle_{s^+} , \quad \langle x \rangle_g ; \quad (8)$$

	★	○	■
DE	At least three lattice spacings[a] with at least two lattice spacings below 0.1 fm and a range of lattice spacings that satisfies $[a_{\max}/a_{\min}]^2 \geq 2$	At least two lattice spacings[a] with at least one point below 0.1 fm and a range of lattice spacings that satisfy $[a_{\max}/a_{\min}]^2 \geq 1.4$	Otherwise
CE	One ensemble with a physical pion mass[b] *or* a chiral extrapolation with three or more pion masses, with at least two pion masses below 250 MeV and at least one below 200 MeV	A chiral extrapolation with three or more pion masses[b], two of which are below 300 MeV.	Otherwise
FV	Ensembles with $M_{\pi,\min}L \geq 4$ *or* at least three volumes with spatial extent $L > 2.5$ fm[c]	Ensembles with $M_{\pi,\min}L \geq 3.4$ *or* at least two volumes with spatial extent $L > 2.5$ fm[c]	Otherwise
RE	Non-perturbative renormalization[d]	Perturbative renormalization (one loop or higher)	Otherwise
ES	At least three source-sink separations or a variational method to optimize the operator derived from at least a 3×3 correlator matrix, at every pion mass and lattice spacing	Two source-sink separations at every pion mass and lattice spacing, or three or more source-sink separations at one pion mass below 300 MeV. For the variational method, an optimized operator derived from a 2×2 correlator matrix at every pion mass and lattice spacing, or a 3×3 correlator matrix for one pion mass below 300 MeV	Otherwise

[a] We assume that the lattice actions are $\mathcal{O}(a)$-improved, *i.e.* that the discretization errors vanish quadratically with the lattice spacing. For unimproved actions, an additional lattice spacing is required. These criteria must be satisfied in each case for at least one pion mass below 300 MeV. To receive a ★ or a ○ either a continuum extrapolation must be performed, or the results must demonstrate no significant discretization effects over the appropriate range of lattice spacings.
[b] We define a physical pion mass ensemble to be one with $M_\pi = 135 \pm 10$ MeV for the above criteria.
[c] For calculations that use a mixed-action approach, *i.e.* with different lattice actions for the valence and sea quarks, we apply these criteria to the valence quarks; $M_{\pi,\min}$ is the lightest pion mass employed in the calculation.
[d] For g_A we award a ★ also to calculations that use fermion actions for which $Z_A/Z_V = 1$ or employ combinations of quantities for which the renormalization is unity by construction.

TABLE II Summary of the rating criteria for lattice QCD computations of PDF moments, see also (Lin *et al.*, 2018d).

$$g_A \equiv \langle 1 \rangle_{\delta u^- - \Delta d^+}, \quad \langle 1 \rangle_{\delta u^-}, \quad \langle 1 \rangle_{\Delta d^+}, \quad \langle 1 \rangle_{\Delta s^+}, \tag{9}$$

$$\langle x \rangle_{\Delta u^- - \Delta d^-}; $$

$$g_T \equiv \langle 1 \rangle_{\delta u^- - \delta d^-}, \quad \langle 1 \rangle_{\delta u^-}, \quad \langle 1 \rangle_{\delta d^-}. \tag{10}$$

The moments of unpolarized and helicity PDFs, Eqs. (8)-(9), correspond to the benchmark quantities already identified in the 2017 PDFLattice white paper, and are expressed using the conventional notation described in Appendix A of (Lin *et al.*, 2018d). We now define the moments of transversity PDFs in a similar way

$$g_T \equiv \langle 1 \rangle_{\delta u^- - \delta d^-} = \int_0^1 dx \left[h_1^{u^-} - h_1^{d^-} \right], \tag{11}$$

$$\langle 1 \rangle_{\delta u^-} = \int_0^1 dx\, h_1^{u^-}, \qquad \langle 1 \rangle_{\delta d^-} = \int_0^1 dx\, h_1^{d^-}, \tag{12}$$

where $h_1^{u^-} = h_1^u - h_1^{\bar{u}}$ and $h_1^{d^-} = h_1^d - h_1^{\bar{d}}$. We do not focus on quantities other than those listed above, because current lattice calculations of higher moments and/or moments of other PDF combinations are not sufficiently mature to allow for a meaningful comparison between lattice QCD and global fit results.

In the 2017 PDFLattice white paper we appraised each source of systematic uncertainty in the lattice QCD results by means of a rating system, defined in Sect. (3.1.2) of (Lin *et al.*, 2018d). Specifically, we considered the following sources of systematic uncertainties: discretization effects and extrapolation to the continuum limit (DE); chiral extrapolation to unphysical pion masses (CE); finite-volume effects (FV); choice of renormalization (RE); and excited state contamination (ES). The rating system, which is inspired to that adopted by the Flavor Lattice Averaging Group FLAG) (Aoki *et al.*, 2020), awards a blue star (★) for sources of uncertainty that are well controlled or very conservatively estimated, a blue circle (○) for sources of uncertainty that have been controlled or estimated to some extent, and a red square (■) for uncertainties that have not met our criteria or for which no estimate is given. The details of the rating system are further summarized in Tab. II for the reader's convenience. Our criteria and the corresponding ratings are chosen to provide as fair an assessment of the various calculations as possible, and are not intended to discredit the merits of any of them. In this respect, our criteria are aspirational: where lattice QCD results do not meet these standards, we hope that the lattice community will work towards improved calculations and greater precision. Modifications to this rating system will occur as the lattice QCD results evolve.

II.3.1.1. Moments of unpolarized PDFs. Modern analyses of unpolarized PDFs benefit from a wide data set (see Fig. 1) and are performed at NNLO perturbative accuracy in the strong coupling as standard in most cases. For this reason, the phenomenological knowledge of lattice-calculable quantities — including unpolarized PDF moments — is well established. The pulls of a typical phenomenological analysis of unpolarized PDFs on the corresponding moments was comprehensively evaluated and mapped in Ref. (Hobbs *et al.*, 2019).

In comparison to the 2017 PDFLattice white paper, some new lattice QCD computations were performed, which we summarize in Tab. III and rate according to the criteria defined in Tab. II. New results, mostly for $N_f = 2+1+1$ and $N_f = 2+1$ dynamical flavors, were computed at a scale $\mu = 2$ GeV, including for $\langle x \rangle_g$. On the global fit front, two new analyses of unpolarized PDFs were released, as discussed in Sect. II.1: CT18 (Hou *et al.*, 2019b) and JAM19 (Sato *et al.*, 2020). We therefore compute the corresponding values for the benchmark moments $\langle x \rangle_{u^+-d^+}$, $\langle x \rangle_{u^+}$, $\langle x \rangle_{d^+}$, $\langle x \rangle_{s^+}$ and $\langle x \rangle_g$ with the highest perturbative accuracy allowed by each analysis, NNLO and NLO, respectively. We report these values at $\mu = 2$ GeV in Tab. IV, where we also display the PDFLattice17 benchmark value (Lin *et al.*, 2018d) for comparison. We recall that this value was determined as the unweighted average of the NNPDF3.1 (Ball *et al.*, 2017), CT14 (Dulat *et al.*, 2016), MMHT14 (Harland-Lang *et al.*, 2015), ABMP16 (Alekhin *et al.*, 2017) (with $N_f = 4$ flavors), CJ15 (Accardi *et al.*, 2016a) and HERAPDF2.0 (Abramowicz *et al.*, 2015) analyses (see Tab. 3.5 of Ref. (Lin *et al.*, 2018d) for their values).

The results for the benchmark moments $\langle x \rangle_{u^+-d^+}$, $\langle x \rangle_{u^+}$, $\langle x \rangle_{d^+}$, $\langle x \rangle_{s^+}$ and $\langle x \rangle_g$, obtained either from lattice QCD (Tab. III) or from a global analysis of the experimental data (Tab. IV), are graphically compared in Fig. 12 at $\mu = 2$ GeV. In each case, we also determine benchmark values by combining various lattice QCD results, on the one hand, and global fit results, on the other hand. For lattice QCD computations, whenever more than one result is available, we take the envelope of all of the available results, separately for each number of dynamical flavors. This choice is conservative, but seems optimal to us: it will not overestimate too much the uncertainty of the benchmark values in the cases in which lattice moments are in good mutual agreement (such as for $\langle x \rangle_{u^+-d^+}$), but at the same time will avoid bias in the cases in which systematic uncertainties on the individual values had not been completely controlled. For global analyses of experimental data, given the overall consistency of the various results and the limited progress, we follow the same prescription adopted in the 2017 PDFLattice white paper, but we update it by replacing the CT14 values with their CT18 counterparts in the unweighted average. We do not include the JAM19 values in it, because the analysis is unique

in its kind, given that it determines PDFs and FFs simultaneously. Our benchmark values are summarized in Tab. V.

As is apparent from Fig. 12 and Tabs. III-V, the overall picture described in the 2017 PDFLattice white paper is somewhat confirmed: there is a fair agreement between lattice QCD and global fit results, with previous tension for $\langle x \rangle_{s^+}$ and $\langle x \rangle_g$ relieved by the new lattice results from ETMC20 and χQCD18. The uncertainty of lattice calculations is in general larger by one order of magnitude than for global fits, also because the constraint of momentum sum rule is usually imposed on the latter but not on the former. All these remarks are still valid if individual results for the benchmark moments are taken in lieu of averages.

II.3.1.2. Moments of helicity PDFs. The nucleon axial charge g_A has long been considered as one of the most important benchmark quantities for lattice QCD computations, given that it is experimentally well determined through neutron weak decays (Tanabashi *et al.*, 2018). Also, g_A is of central importance to QCD, as it is related to the Bjorken sum rule (Bjorken, 1966, 1970).

In comparison to the 2017 PDFLattice white paper, several new lattice QCD computations of g_A and of the flavor-diagonal axial charges appeared in the literature, which we summarize in Tab. VI and rate according to the criteria defined in Tab. II. A pool of new results for $N_f = 2+1$ and $N_f = 2+1+1$ dynamical flavors were computed. Conversely, the determination of helicity PDFs in global fits did not witness significant changes since the publication of the 2017 PDFLattice white paper. We therefore refer the reader to the numbers reported in Tab. 3.6 of Ref. (Lin *et al.*, 2018d).

The results for the benchmark moments g_A, $\langle 1 \rangle_{\Delta u^+}$, $\langle 1 \rangle_{\Delta d^+}$, $\langle 1 \rangle_{\Delta s^+}$, and $\langle x \rangle_{\Delta u^- - \Delta_d^-}$, obtained either from lattice QCD (Tab. VI) or from the PDFLattice17 average of global fits (Lin *et al.*, 2018d), are graphically compared in Fig. 13 at $\mu = 2$ GeV. In each case, we also determine the benchmark values from the various results. For lattice QCD computations, we use the same prescription adopted in the case of unpolarized moments: whenever more than one result is available, we take the envelope of all of the available results, separately for each number of dynamical flavors. For global analyses of experimental data, given the lack of new results, we take the 2017 PDFLattice average. We recall that it was determined as the unweighted average of the NNPDFPOL1.1 (Nocera *et al.*, 2014), DSSV08 (de Florian *et al.*, 2009) and JAM15 (Sato *et al.*, 2016) analyses. Our benchmark values are summarized in Tab. VII at $\mu = 2$ GeV.

As is apparent from Fig. 13 and Tabs. VI-VII there is an overall fair agreement between lattice QCD computations and phenomenological fits, except for some
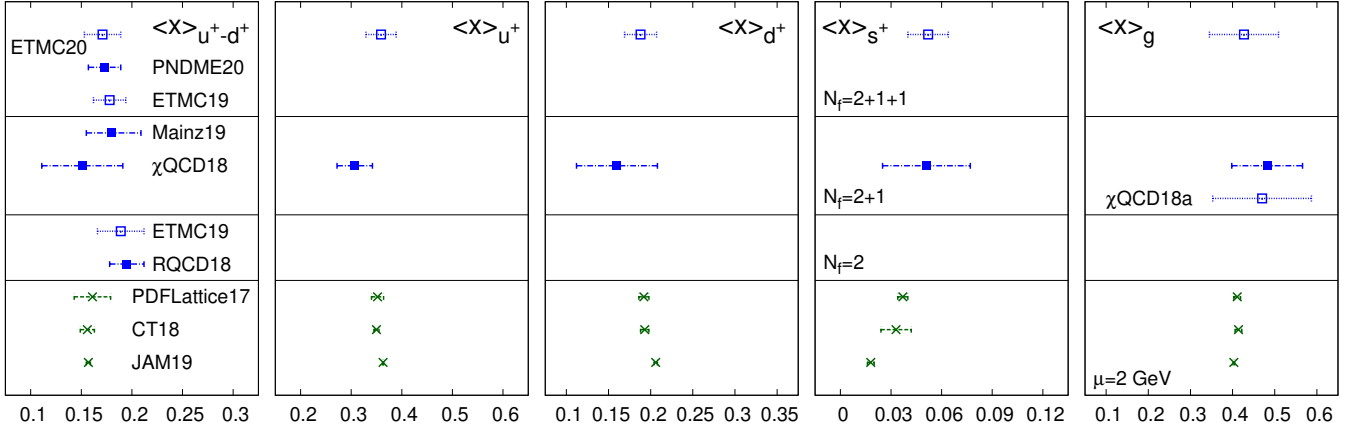
FIG. 12 The lattice QCD (in blue) and global fit (in green) values for the benchmark moments defined in Eq. (8), as collected in Tabs. III and IV. Lattice QCD results with stars or circles for all of the sources of systematic uncertainties in Tab. II are denoted with filled squares, otherwise with empty squares. All values are at $\mu = 2$ GeV.
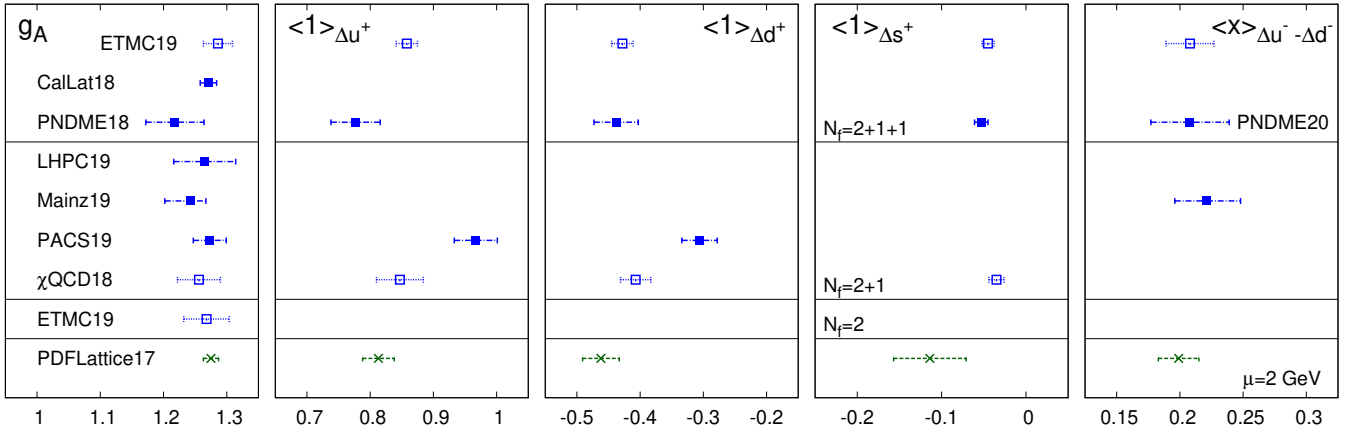

FIG. 13 Same as Fig. 12, but for the benchmark moments of helicity PDFs. See Tab. VI for references.

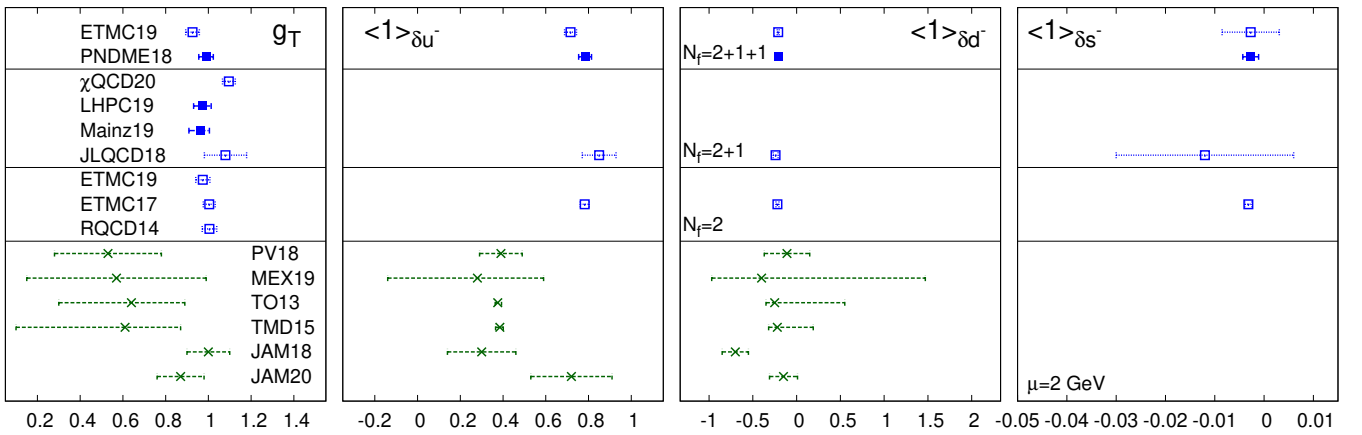FIG. 14 Same as Fig. 12, but for the benchmark moments of transversity PDFs.

Moment	Collaboraton	Reference	N_f	DE	CE	FV	RE	ES		Value
$\langle x\rangle_{u^+-d^+}$	ETMC 20	(Alexandrou *et al.*, 2020b)	2+1+1	■	★	○	★	★	**	0.171(18)
	PNDME 20	(Mondal *et al.*, 2020)	2+1+1	★	★	★	★	★		0.173(14)(07)
	ETMC 19	(Alexandrou *et al.*, 2020c)	2+1+1	■	★	○	★	★	**	0.178(16)
	Mainz 19	(Harris *et al.*, 2019)	2+1	★	○	★	★	★		$0.180(25)(^{+14}_{-6})$
	χQCD 18	(Yang *et al.*, 2018b)	2+1	○	★	○	★	★		0.151(28)(29)
	ETMC 19	(Alexandrou *et al.*, 2020c)	2	■	★	○	★	★	**	0.189(23)
	RQCD 18	(Bali *et al.*, 2019b)	2	★	★	○	★	★		0.195(07)(15)
$\langle x\rangle_{u^+}$	ETMC 20	(Alexandrou *et al.*, 2020b)	2+1+1	■	★	○	★	★	**	0.359(30)
	χQCD 18	(Yang *et al.*, 2018b)	2+1	○	★	○	★	★		0.307(30)(18)
$\langle x\rangle_{d^+}$	ETMC 20	(Alexandrou *et al.*, 2020b)	2+1+1	■	★	○	★	★	**	0.188(19)
	χQCD 18	(Yang *et al.*, 2018b)	2+1	○	★	○	★	★		0.160(27)(40)
$\langle x\rangle_{s^+}$	ETMC 20	(Alexandrou *et al.*, 2020b)	2+1+1	■	★	○	★	★	**	0.052(12)
	χQCD 18	(Yang *et al.*, 2018b)	2+1	○	★	○	★	★		0.051(26)(5)
$\langle x\rangle_{g}$	ETMC 20	(Alexandrou *et al.*, 2020b)	2+1+1	■	★	○	★	★	**	0.427(92)
	χQCD 18	(Yang *et al.*, 2018b)	2+1	○	★	○	★	★		0.482(69)(48)
	χQCD 18a	(Yang *et al.*, 2018a)	2+1	■	★	★	★	■		0.47(4)(11)

** No quenching effects are seen.

TABLE III Lattice QCD values of the benchmark moments of unpolarized PDFs $\langle x\rangle_{u^+-d^+}$, $\langle x\rangle_{u^+}$, $\langle x\rangle_{d^+}$, $\langle x\rangle_{s^+}$ and $\langle x\rangle_{g}$, rated according to the criteria in Tab. II. The numbers in parentheses refer to the statistical and systematic uncertainties, respectively, or to the combination of the two, if a single value is provided. All values are obtained at $\mu = 2$ GeV.

Moment	PDFLattice17	CT18	JAM19
$\langle x \rangle_{u^+ - d^+}$	0.161(18)	0.156(7)	0.157(2)
$\langle x \rangle_{u^+}$	0.352(12)	0.350(5)	0.363(1)
$\langle x \rangle_{d^+}$	0.192(6)	0.193(5)	0.206(2)
$\langle x \rangle_{s^+}$	0.037(3)	0.033(9)	0.018(2)
$\langle x \rangle_g$	0.411(8)	0.413(8)	0.403(2)

TABLE IV Values for global fit determinations of the benchmark moments of unpolarized PDFs (see text for details) for the PDFLattice17 average (Lin *et al.*, 2018d), and for the CT18 (Hou *et al.*, 2019b) and JAM19 (Sato *et al.*, 2020) analyses. All values are shown at $\mu = 2$ GeV.

Moment	Lattice QCD	Global Fit
$\langle x \rangle_{u^+ - d^+}$	$0.153 — 0.194^a$ $0.111 — 0.209^b$ $0.166 — 0.212^c$	0.161(18)
$\langle x \rangle_{u^+}$	$0.359(30)^{a,\dagger}$ $0.307(35)^{b,\dagger}$	0.353(12)
$\langle x \rangle_{d^+}$	$0.188(19)^{a,\dagger}$ $0.160(48)^{b,\dagger}$	0.192(6)
$\langle x \rangle_{s^+}$	$0.052(12)^{a,\dagger}$ $0.051(26)^{b,\dagger}$	0.037(3)
$\langle x \rangle_g$	$0.427(92)^{a,\dagger}$ $0.353 — 0.587^b$	0.411(8)

^{a} $N_f = 2 + 1 + 1$ ^{b} $N_f = 2 + 1$ ^{c} $N_f = 2$
† Single lattice result

TABLE V Benchmark values for lattice QCD calculations and global fit determinations of the benchmark moments of unpolarized PDFs (see text for details). All values are shown at $\mu = 2$ GeV.

discrepancies in the results for the individual flavor components of the axial charge. Contrary to the case of unpolarized moments, the uncertainties of the two are of comparable size. We note however that the uncertainties on the global fit result might be underestimated because of extrapolation into the small- and large-x regions, where data are less abundant. We also remark that current uncertainties on g_A do not discriminate among lattice QCD results obtained with a different numbers of dynamical flavours, thus confirming that $\mathrm{SU}_f(2)$ is a good symmetry of QCD.

II.3.1.3. Moments of Transversity PDFs. The nucleon isovector tensor charge g_T has recently received much attention, namely as a probe of beyond-the-Standard-Model (bSM) effects. On the one hand, it can contribute to neutron β decay through a possible tensor coupling not included in the SM Lagrangian (Bhattacharya *et al.*, 2012). On the other hand, it affects the contribution of quark electric dipole moments to the neutron electric dipole moment in a way which is relevant for searches of bSM sources of CP-violation (Dubbers and Schmidt, 2011; Yamanaka *et al.*, 2017). A precise determination of g_T has therefore become crucial (Courtoy *et al.*, 2015).

Lattice calculations of the isovector tensor charge are currently the most precise lattice estimates of isovector charges because of small statistical fluctuations and a mild dependence on extrapolation parameters. Results from several collaborations are available, including for the flavor-diagonal charges $\langle 1 \rangle_{\delta u^-}$, $\langle 1 \rangle_{\delta d^-}$ and $\langle 1 \rangle_{\delta s^-}$, which are summarized (and rated according to the criteria in Tab. II) in Tab. VIII at $\mu = 2$ GeV.

The values of the tensor charge g_T and of its flavor components $\langle 1 \rangle_{\delta u^-}$ and $\langle 1 \rangle_{\delta d^-}$ obtained from the determination of transversity PDFs from experimental data are summarized in Tab. IX. As discussed in Sect. II.1.4 two of these analyses are performed in a purely collinear framework, namely PV18 (Radici and Bacchetta, 2018) and MEX19 (Benel *et al.*, 2020), while the others are performed by means of the TMD formalism (see Sect. IV). All of these analyses do not include information on the tensor charge from the lattice, except for JAM18 (Lin *et al.*, 2018c), where the fit is constrained by the average lattice value of g_T. All values in Tab. IX are computed at a scale $\mu = 2$ GeV, except for the TO13 ($\mu = 1$ GeV) and for the TMD15 ($\mu = \sqrt{10}$ GeV) analyses; error bars on the PV18 (Radici and Bacchetta, 2018) and JAM20 (Cammarota *et al.*, 2020) results represent 90% confidence levels.

The results for the tensor charge g_T and for its flavor components, obtained ether from lattice QCD or from a global analysis of the experimental data, are graphically compared in Fig. 14 at $\mu = 2$ GeV. In each case, we also determine benchmark values by suitably combining various lattice QCD results, on the one hand, and global fit results, on the other hand. For lattice QCD computations, we use the same prescription adopted in the case of unpolarized moments: whenever more than one result is available, we take the envelope of all of the available results, separately for each number of dynamical flavors. For global analyses of experimental data, the spread of values is such that any combination, *e.g.* in the form of their unweighted average, seems unjustified; more conservatively, we therefore take the envelope of the various results. Note that no global fit results are available for the strange component of the tensor charge, $\langle 1 \rangle_{\delta s^-}$ due to the lack of data sensitive to it. All these values are summarized in Tab. X at $\mu = 2$ GeV.

As is apparent from Fig. 14 and Tabs. IX-X, the results obtained from a global analysis of experimental data are affected by uncertainties which are significantly larger than those of their lattice counterparts as well as than those of their unpolarized and helicity companions. The reason for this state of affairs is the severe lack of data (see Fig. 1), and the consequent difficulty in estimating the extrapolation uncertainty that affects transversity outside the region covered by data. For instance, in the PV18 analysis, the Mellin moment was computed in the range $[x_{\min}, 1]$, where $x_{\min} = 10^{-6}$

Moment	Collaboration	Reference	N_f	DE	CE	FV	RE	ES		Value
g_A	ETMC 19	(Alexandrou *et al.*, 2019b)	2+1+1	■	★	○	★	★	**	1.286(23)
	CalLat 18	(Chang *et al.*, 2018)	2+1+1	○	★	★	★	★		1.271(13)
	PNDME 18	(Gupta *et al.*, 2018)	2+1+1	★	★	★	★	★		1.218(25)(30)
	LHPC 19	(Hasan *et al.*, 2019)	2+1	○	★	★	★	★		1.265(49)
	Mainz 19	(Harris *et al.*, 2019)	2+1	★	○	★	★	★		$1.242(25)(^0_{-31})$
	PACS 19	(Shintani *et al.*, 2019)	2+1	○	★	★	★	★		1.273(24)(5)(9)
	χQCD 18	(Liang *et al.*, 2018b)	2+1	○	■	★	★	★		1.256(16)(30)
	ETMC 19	(Alexandrou *et al.*, 2019b)	2	■	★	○	★	★	**	1.268(36)
$\langle 1 \rangle_{\Delta u^+}$	ETMC 19	(Alexandrou *et al.*, 2019b)	2+1+1	■	★	○	★	★	**	0.858(17)
	PNDME 18	(Gupta *et al.*, 2018)	2+1+1	★	★	★	★	★		0.777(25)(30)
	PACS 19	(Shintani *et al.*, 2019)	2+1	○	★	★	★	★		0.967(30)(16)
	χQCD 18	(Liang *et al.*, 2018b)	2+1	○	■	★	★	★		0.847(18)(32)
$\langle 1 \rangle_{\Delta d^+}$	ETMC 19	(Alexandrou *et al.*, 2019b)	2+1+1	■	★	○	★	★	**	−0.428(17)
	PNDME 18	(Gupta *et al.*, 2018)	2+1+1	★	★	★	★	★		−0.438(18)(30)
	PACS 19	(Shintani *et al.*, 2019)	2+1	○	★	★	★	★		−0.306(19)(21)
	χQCD 18	(Liang *et al.*, 2018b)	2+1	○	■	★	★	★		−0.407(16)(18)
$\langle 1 \rangle_{\Delta s^+}$	ETMC 19	(Alexandrou *et al.*, 2019b)	2+1+1	■	★	○	★	★	**	−0.0450(71)
	PNDME 18	(Gupta *et al.*, 2018)	2+1+1	★	★	★	★	★		−0.053(8)
	χQCD 18	(Liang *et al.*, 2018b)	2+1	○	■	★	★	★		−0.035(6)(7)
$\langle x \rangle_{\Delta u^- - \Delta d^-}$	PNDME 20	(Mondal *et al.*, 2020)	2+1+1	★	★	★	★	★		0.208(19)(24)
	ETMC 19	(Alexandrou *et al.*, 2019b)	2+1+1	■	★	○	★	★	**	0.193(19)
	Mainz 19	(Harris *et al.*, 2019)	2+1	★	○	★	★	★		$0.221(25)(^{+10}_{-0})$

** No quenching effects are seen.

TABLE VI Same as Tab. III, but for the axial charge $g_A = \langle 1 \rangle_{\delta u^- - \delta d^-}$ and the moments of helicity PDFs $\langle 1 \rangle_{\delta u^-}$, $\langle 1 \rangle_{\delta d^-}$, and $\langle 1 \rangle_{\delta s^-}$. All values are obtained at $\mu = 2$ GeV. Note that g_A is scale invariant.

Moment	Lattice QCD	Global Fit
g_A	$1.179 - 1.309^a$ $1.202 - 1.314^b$ $1.268(36)^{c,\dagger}$	1.258(28)
$\langle 1 \rangle_{\Delta u^+}$	$0.738 - 0.875^a$ $0.810 - 1.001^b$	0.813(25)
$\langle 1 \rangle_{\Delta d^+}$	$-0.473 - -0.403^a$ $-0.431 - -0.278^b$	-0.462(29)
$\langle 1 \rangle_{\Delta s^+}$	$-0.0538 - -0.0379^a$ $-0.0035(9)^{b,\dagger}$	-0.114(43)
$\langle x \rangle_{\Delta u^- - \Delta d^-}$	$0.174 - 0.239^a$ $0.221(^{27}_{25})^{b,\dagger}$	0.199(16)

$^a N_f = 2 + 1 + 1$ $^b N_f = 2 + 1$ $^c N_f = 2$
† Single lattice result

TABLE VII Same as Tab. V, but for helicity PDFs.

for the adopted MSTW08LO parametrization (Martin *et al.*, 2009) of the unpolarized PDF in Eq. (2). This constraint avoided extrapolation errors below $x_{\min}$ and ensured that the tensor charge is evaluated at 1% accuracy (Radici and Bacchetta, 2018). In the MEX19 analysis, extrapolation was controlled by choosing a parametrization that ensured the integrability of h_1 by construction.

From Fig. 14, we also conclude that most determinations of the tensor charge from global fits are compatible with each other. The compatibility with lattice results is a little more involved. While it is obvious for g_T^d (within large uncertainties), there is a clear tension (up to 2σ) for g_T^u and, consequently, for g_T.

In particular, the JAM18 result is compatible with the lattice prediction for g_T by construction, but it is largely incompatible for the flavor-diagonal tensor charges. The JAM20 result is the only one that is compatible with all of the lattice tensor charges; it clearly supersedes JAM18 and confirms how crucial is to pursue global fits from large independent data sets. However, the JAM20 analysis has some relevant limitations (for example, it does not include effects from TMD evolution, which might be important when connecting SIDIS data to e^+e^- and hadronic collision data at much higher scales); because of the still large error bars, this result is also compatible with other phenomenological outcomes, and in particular with the global fit PV18. In conclusion, the issue of compatibility of tensor charges obtained from lattice calculations and from phenomenological fits still requires further studies.

II.3.2. Lattice data in global fits

In order to extract PDFs from a set of experimental measurements, a factorization theorem connecting the theoretical predictions for these data to the PDFs is needed. For example, in the case of unpolarized DIS, the measured structure functions F are expressed in terms of

Moment	Collaboration	Reference	N_f	DE	CE	FV	RE	ES		Value
g_T	ETMC 19	(Alexandrou *et al.*, 2019b)	2+1+1	■	★	○	★	★	**	0.926(32)
	PNDME 18	(Gupta *et al.*, 2018)	2+1+1	★	★	★	★	★	*	0.989(32)(10)
	χQCD 20	(Horkel *et al.*, 2020)	2+1	■	★	○	★	★	†	1.096(30)
	LHPC 19	(Hasan *et al.*, 2019)	2+1	○	★	○	★	★	*	0.972(41)
	Mainz 19	(Harris *et al.*, 2019)	2+1	★	○	★	★	★		$0.965(38)(^{+13}_{-41})$
	JLQCD 18	(Yamanaka *et al.*, 2018)	2+1	■	○	○	★	★		1.08(3)(3)(9)
	ETMC 19	(Alexandrou *et al.*, 2019b)	2	■	★	○	★	★	**	0.974(33)
	ETMC 17	(Alexandrou *et al.*, 2017d)	2	■	★	■	★	★		1.004(21)(02)(19)
	RQCD 14	(Bali *et al.*, 2015)	2	○	★	★	★	■		1.005(17)(29)
$\langle 1 \rangle_{\delta u^-}$	ETMC 19	(Alexandrou *et al.*, 2019b)	2+1+1	■	★	○	★	★	**	0.716(28)
	PNDME 18	(Gupta *et al.*, 2018)	2+1+1	★	★	★	★	★	*	0.784(28)(10)
	JLQCD 18	(Yamanaka *et al.*, 2018)	2+1	■	○	○	★	★		0.85(3)(2)(7)
	ETMC 17	(Alexandrou *et al.*, 2017d)	2	■	★	■	★	★		0.782(16)(2)(13)
$\langle 1 \rangle_{\delta d^-}$	ETMC 19	(Alexandrou *et al.*, 2019b)	2+1+1	■	★	○	★	★	**	-0.210(11)
	PNDME 18	(Gupta *et al.*, 2018)	2+1+1	★	★	★	★	★	*	-0.204(11)(10)
	JLQCD 18	(Yamanaka *et al.*, 2018)	2+1	■	○	○	★	★		-0.24(2)(0)(2)
	ETMC 17	(Alexandrou *et al.*, 2017d)	2	■	★	■	★	★		-0.219(10)(2)(13)
$\langle 1 \rangle_{\delta s^-}$	ETMC 19	(Alexandrou *et al.*, 2019b)	2+1+1	■	★	○	★	★	**	-0.0027(58)
	PNDME 18	(Gupta *et al.*, 2018)	2+1+1	★	★	★	★	★	*	-0.0027(16)
	JLQCD 18	(Yamanaka *et al.*, 2018)	2+1	■	○	○	★	★		-0.012(16)(8)
	ETMC 17	(Alexandrou *et al.*, 2017d)	2	■	★	■	★	★		-0.00319(69)(2)(22)

** No quenching effects are seen.
* Not fully $\mathcal{O}(a)$ improved by requiring an additional lattice spacing.
† The rating comes from the valence pion mass used in the calculation. In other calculations, valence an sea pions are the same.

TABLE VIII Same as Tab. III, but for the tensor charge $g_T = \langle 1 \rangle_{\delta u^- - \delta d^-}$ and the transverse flavor diagonal charges $\langle 1 \rangle_{\delta u^-}$, $\langle 1 \rangle_{\delta d^-}$, and $\langle 1 \rangle_{\delta s^-}$. All values are obtained at $\mu = 2$ GeV.

Collaboration	g_T	$\langle 1 \rangle_{\delta u^-}$	$\langle 1 \rangle_{\delta d^-}$
PV18	0.53(25)	0.39(10)	$-0.11(26)$
MEX19	0.57(42)	$0.28(^{+31}_{-42})$	$-0.40(^{+87}_{-57})$
TO13	$0.64(^{+25}_{-34})$	$0.375(^{+18}_{-12})$	$-0.25(^{+30}_{-10})$
TMD15	$0.61(^{+26}_{-51})$	$0.385(^{+16}_{-20})$	$-0.22(^{+31}_{-10})$
JAM18	1.0(1)	0.30(16)	$-0.70(15)$
JAM20	0.87(11)	0.72(19)	$-0.15(16)$

TABLE IX The values of the tensor charge g_T and of its flavor components $\langle 1 \rangle_{\delta u^-}$ and $\langle 1 \rangle_{\delta d^-}$ obtained from the following determinations of transverssity PDFs: PV18 (Radici and Bacchetta, 2018), from a global fit of data on inclusive di-hadron production in SIDIS and pp; MEX19 (Benel *et al.*, 2020), from the same mechanism but on SIDIS data only; TO13 (Anselmino *et al.*, 2013), from a parton-model analysis of Collins effect in SIDIS and e^+e^- data; TMD15 (Kang *et al.*, 2016), from the same data set but analyzed in the TMD framework including evolution effects; JAM18 (Lin *et al.*, 2018c), as in TO13, but constrained to reproduce the lattice average value for g_T; and JAM20 (Cammarota *et al.*, 2020) from a global fit of inclusive single-hadron production data. All values are computed at $\mu = 2$ GeV, except for TO13 ($\mu = 1$ GeV) and TMD15 ($\mu = \sqrt{10}$ GeV).

the unpolarized PDFs f as

$$F\left(x, Q^2\right) = \sum_q \int_x^1 \frac{d\xi}{\xi} C_q \left(\frac{x}{\xi}, \frac{Q^2}{\mu^2}, \alpha_s \right) f_q \left(\xi, \mu^2 \right)$$
$$\equiv \sum_q C_q \left(x, \frac{Q^2}{\mu^2}, \alpha_s \right) \otimes f_q \left(x, \mu^2 \right), \quad (13)$$

Moment	Lattice QCD	Global Fit
g_T	$0.894 - 1.023^a$	
	$0.909 - 1.175^b$	$0.10 - 1.1$
	$0.941 - 1.039^c$	
$\langle 1 \rangle_{\delta u^-}$	$0.688 - 0.814^a$	
	$0.85(8)^{b,\dagger}$	$-0.14 - 0.91$
	$0.782(21)^{c,\dagger}$	
$\langle 1 \rangle_{\delta d^-}$	$-0.221 - -0.189^a$	
	$-0.24(3)^{b,\dagger}$	$-0.97 - 0.47$
	$-0.219(17)^{c,\dagger}$	
$\langle 1 \rangle_{\delta s^-}$	$-0.0085 - 0.0031^a$	
	$-0.012(18)^{b,\dagger}$	—
	$-0.00319(72)^{c,\dagger}$	

$^a N_f = 2+1+1$ $^b N_f = 2+1$ $^c N_f = 2$
† Single lattice result

TABLE X Same as Tab. V, but for transversity PDFs.

where C_q are the perturbatively computable Wilson coefficients and the symbol $\otimes$ denotes the convolution integral. One can parametrize the unknown PDFs at a given scale Q_0, and express the theoretical predictions as a function of the PDF parameters (called θ henceforth) after performing DGLAP evolution of the PDF to the scale of the data Q via the Altarelli-Parisi kernel Γ:

$$f_q \left(x, Q^2; \theta \right) = \Gamma \left(Q^2, Q_0^2, \alpha_s \right) \otimes f_q \left(x, Q_0^2; \theta \right). \quad (14)$$

In a global fit, the procedure is applied simultaneously to every process for which experimental data and

a factorization theorem are available. The PDF parameters are then determined by optimizing an appropriate figure of merit, usually the log-likelihood χ^2.

The steps described above can be equally applied to the extraction of PDFs from lattice data, as described and implemented in Refs. (Cichy *et al.*, 2019; Karpie *et al.*, 2019; Ma and Qiu, 2018a,b). Since lattice QCD cannot calculate PDFs directly, a factorization theorem is necessary in order to connect some lattice observable to parton distributions, just like how the factorization formula in Eq. (13) connects theoretical predictions for DIS experimental data to PDFs. By lattice observable we mean a quantity which in practice can be computed on the lattice: here we will consider the position-space matrix element between proton states of the vector bilocal operator underlying the definition of quasi- and pseudo-PDFs

$$M_A\left(\nu, z^2\right) = \langle P|\bar{\psi}(z)\lambda_A\gamma_0\, U(z,0)\psi(0)|P\rangle, \qquad (15)$$

where $\nu = P\cdot z$, λ_A denotes the flavour structure and the separation between fields is purely spatial $z = (0,0,0,z)$. This factorization formula has been worked out up to 1-loop order in perturbation theory, in several independent ways. In the case of quasi-PDFs, the factorization is realized in momentum space, in the limit of large proton momentum, giving

$$\tilde{f}_A(x,\mu^2) = \int_{-1}^1 \frac{dy}{|y|}\, C_A\left(\frac{x}{y}, \frac{\mu}{P_z}, \frac{\mu}{\mu'}\right) f_A(y,\mu'^2)$$
$$+ \mathcal{O}\left(\frac{M^2}{P_z^2}, \frac{\Lambda_{\mathrm{QCD}}^2}{P_z^2}\right), \qquad (16)$$

$\tilde{f}_A(x,\mu^2)$ and C_A being the quasi-PDF and the momentum space matching coefficients respectively. Considering the case of the unpolarized isovector parton distribution, starting from Eq. (16) we can take the real and imaginary part of its inverse Fourier transform, introducing the two following lattice observables

$$\mathrm{Re}\left[M\left(\nu, z^2; \mu\right)\right] = \int_0^1 dx\, \mathcal{C}_3^{\mathrm{Re}}\left(\nu x, z, \frac{\mu}{P_z}\right) V_3\left(x, \mu\right)$$
$$= \mathcal{C}_3^{\mathrm{Re}}\left(z, \frac{\mu}{P_z}\right) \circledast V_3\left(\mu^2\right), \qquad (17)$$

$$\mathrm{Im}\left[M\left(\nu, z^2; \mu\right)\right] = \int_0^1 dx\, \mathcal{C}_3^{\mathrm{Im}}\left(\nu x, z, \frac{\mu}{P_z}\right) T_3\left(x, \mu\right)$$
$$= \mathcal{C}_3^{\mathrm{Im}}\left(z, \frac{\mu}{P_z}\right) \circledast T_3\left(\mu^2\right), \qquad (18)$$

where V_3 and T_3 are the nonsinglet distributions

$$V_3(x) = u\left(x\right) - \bar{u}\left(x\right) - \left[d\left(x\right) - \bar{d}\left(x\right)\right], \qquad (19)$$
$$T_3(x) = u\left(x\right) + \bar{u}\left(x\right) - \left[d\left(x\right) + \bar{d}\left(x\right)\right]. \qquad (20)$$

Eqs. (17) and (18) can then be used to build, together with the corresponding values from the lattice, a

χ^2 function, whose minimization would lead to the determination of V_3 and T_3. In order to define a meaningful χ^2, the statistical and systematical uncertainties over each data point, together with their correlations, have to be known. Once these two pieces of information are provided, a fit to lattice data can be performed using the same fitting framework adopted for experimental data, without any major modification. This exercise was performed in Ref. (Cichy *et al.*, 2019), using data for the quasi-PDFs matrix element computed by the ETMC collaboration (Alexandrou *et al.*, 2019d, 2018b), within the NNPDF fitting framework. Various assumptions for the systematic uncertainties on the lattice data were considered, corresponding to optimistic, realistic and pessimistic scenarios, respectively. A representative result of this exercise is displayed in Fig. 15, where two lattice results obtained in realistic scenarios (labelled as S2 and S5) are compared to the NNPDF3.1 global analysis for the T_3 and V_3 nonsiglet distributions at a scale $\mu = 1.6$ GeV. As can be seen from Fig. 15, the lattice result is affected by large uncertainties in comparison to its phenomenological counterpart, and displays a fairly shifted shape.

The same steps can be repeated for any lattice observable, *e.g.* lattice computable hadron matrix elements, like the one in Eq. (15) but with different parton operators, as long as the observables can be factorized into perturbatively calculable coefficient functions convoluted with the same PDFs (Ma and Qiu, 2018a,b). Here, the data of these lattice observables play the same role as experimental data that can be used for extracting PDFs. Although current lattice data cannot cover a kinematic range as wide as experimental data can, lattice calculations could be advantageous for extracting PDFs, or partonic structure in general, of hadrons that are difficult to do experiments with, such as free neutrons, pions (Sufian *et al.*, 2020, 2019), and kaons.

II.3.3. Unpolarized and helicity strange PDFs

The strange and antistrange PDFs remain the least known PDFs among all of the unpolarized and helicity distributions. This state of affairs is determined by the lack of experimental data sensitive to this flavor, and is further aggravated by apparent inconsistencies between different data sets. In the unpolarized case, discrepancies have arisen in analyses of inclusive $W^{\pm}/Z$ production from ATLAS with respect to charged-current neutrino DIS measurements. While the former support a ratio of the strange to non-strange light sea quarks around unity, the latter give a result around one half at a scale of 1.9 GeV^2 (Aad *et al.*, 2014). This state of affairs is illustrated in Fig. 16, where we compare the ratio $(s(x,Q) + \bar{s}(x,Q))/\left(\bar{u}(x,Q) + \bar{d}(x,Q)\right)$ for the CT18, MMHT14 and NNPDF3.1 PDF sets at $Q = 2$ GeV.
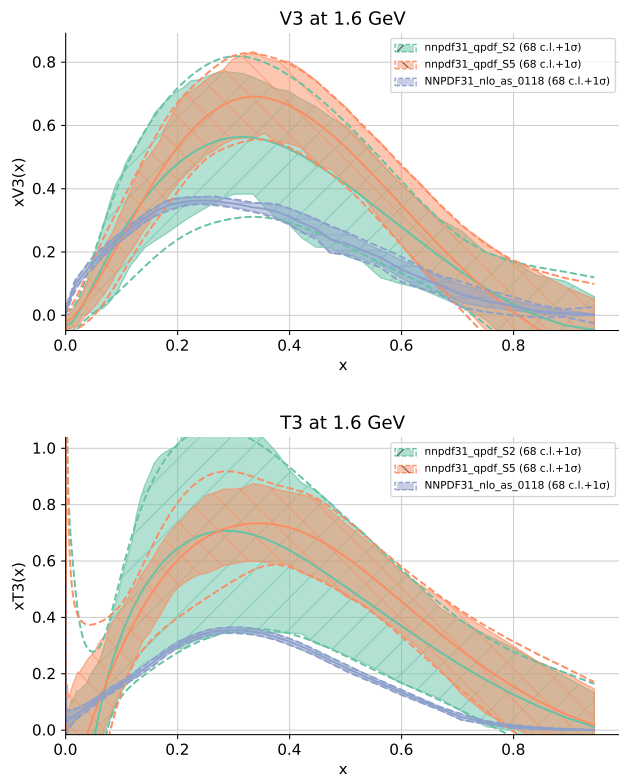
FIG. 15 A comparison of two lattice results (labelled S2 and S5), obtained from an analysis of lattice data with a realistic estimate of systematic uncertainties, with the result of the NNPDF3.1 global analysis. Results are displayed for the V_3 (top) and T_3 (bottom) nonsiglet PDF combinations at a scale $\mu = 1.6$ GeV. Figure from (Cichy *et al.*, 2019).

In all of the three PDF sets, the ratio is dominated by neutrino DIS data. The lack of higher-order massive corrections or nuclear uncertainties (Ball *et al.*, 2019) in the description of these data or a sub-optimal estimate of experimental correlations in the ATLAS $W^{\pm}/Z$ data may be reasons for the discrepancy between the two, which are currently being investigated. The picture is further complicated if measurements of kaon production in SIDIS are added in the QCD analyses, a fact that suppresses the ratio even more (Sato *et al.*, 2020).

In the helicity case, the strange distribution is entirely unconstrained unless measurements of SIDIS asymmetries for kaon production are incorporated in the analyses or if $\mathrm{SU}_f(3)$ constraints from weak baryon decays are assumed. In both cases, the strange helicity PDF is prone to a theoretical bias difficult to quantify, coming respectively from missing uncertainties in the fragmentation of an s quark into a kaon or from the violation of $\mathrm{SU}_f(3)$ symmetry.

Exploratory studies using lattice QCD to determine the unpolarized strange PDFs are ongoing. A first lattice calculation of the strange quasi-PDFs (Zhang *et al.*, 2020b) is compared to the Fourier transform of
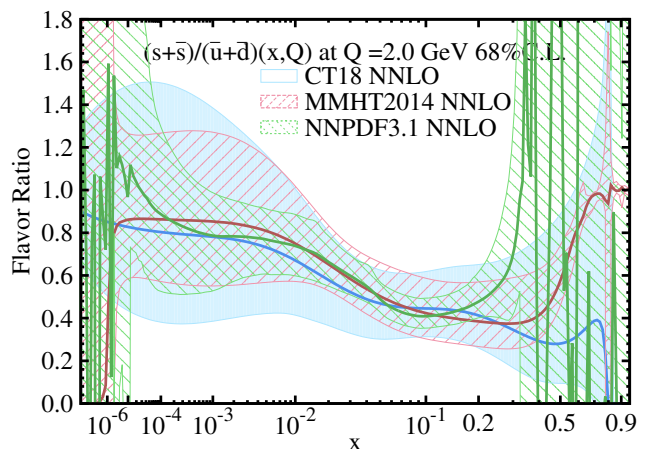

FIG. 16 A comparison of 68% C.L. uncertainties on the ratio $(s(x,Q) + \bar{s}(x,Q)) / (\bar{u}(x,Q) + \bar{d}(x,Q))$, for CT18, MMHT2014 and NNPDF3.1 PDFs at $Q = 2$ GeV.

the global fitting results from NNPDF3.1 (Ball *et al.*, 2017) and CT18 (Hou *et al.*, 2019b) at NNLO in Fig. 17 at a scale of 4 GeV^2. The quasi-PDF matrix elements are extracted from correlators computed on the $a \approx 0.12$ fm, $24^3 \times 64$ ensemble with $2 + 1 + 1$ flavors of highly improved staggered quarks (Follana *et al.*, 2007) and $M_{\pi} \approx 310$ MeV was generated by the MILC collaboration (Bazavov *et al.*, 2013). Hypercubic smearing (Hasenfratz and Knechtli, 2001) is applied to the configurations. To approach the light-cone distribution, the nucleon operator is constructed with momentum smeared quark sources (Bali *et al.*, 2016) and boosted to momenta up to $P_z = 2.18$ GeV. The matrix elements are renormalized with non-perturbative renormalization factors in the RI/MOM scheme (Martinelli *et al.*, 1995) at $\mu^R = 2.4$ GeV, $pz^R = 0$. Due to the assumption $s(x) = \bar{s}(x)$ in the CT18 PDF set, the Fourier transformed matrix elements have a vanishing real part. It is observed that the real part of the renormalized quasi-PDF matrix elements are consistent with zero at large momentum. The imaginary matrix elements are proportional to the sum of the quark and antiquark distribution; the magnitude is consistently smaller than those from CT18 and NNPDF, possibly due to missing the contributions from other flavor distributions in the matching kernel. A full analysis of lattice-QCD systematics, such as finite-volume effects and discretization, is not yet included, and plans to extend the current calculations are underway.
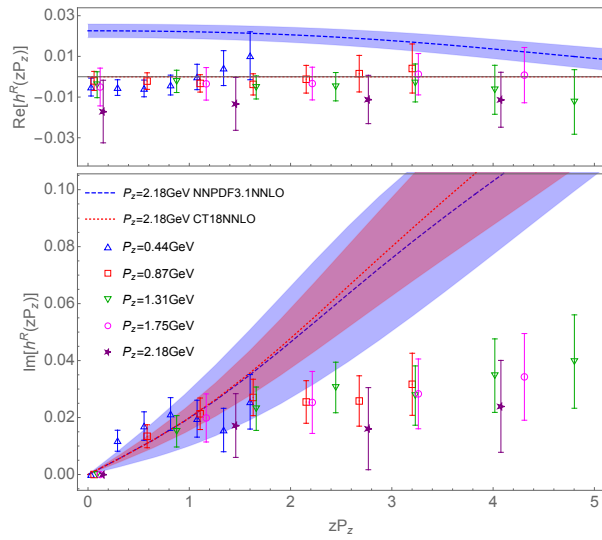
FIG. 17 The quasi-PDF matrix element renormalized in the RI/MOM scheme at $\mu^R = 2.4$ GeV, $pz^R = 0$ on the lattice compared with the Fourier transform of the NNLO NNDPF3.1 and CT18 PDF sets. The upper (lower) plot is the real (imaginary) part. The real part of the CT18 PDF is exactly zero because of the $s(x) = \bar{s}(x)$ assumption entering the fit. The imaginary part of the lattice result grows slower at large z, and the real part is consistent with zero at large momentum.

III. GENERALIZED PDFS (GPD)

III.1. Introduction

More than half a century after the first discovery of the nucleon's internal structure, we still know little about its three-dimensional structure, which is described in terms of the generalized parton distributions (GPDs). Interest in GPDs has grown rapidly since they were first introduced in the late 90's (Ji, 1997; Müller *et al.*, 1994; Radyushkin, 1996), because of the unique insight they provide into the spatial distribution of quarks and gluons inside the proton (Burkardt, 2000), as well as its mechanical properties, including angular momentum, pressure, and shear forces (Polyakov, 2003) (for extensive reviews on the subject see Refs. (Belitsky and Radyushkin, 2005; Diehl, 2003; Kumericki *et al.*, 2016)). While the latter are encoded in the QCD energy-momentum tensor which is canonically probed through gravity, it was realized by Ji (Ji, 1997) that its matrix elements between proton states can be described through Mellin moments of GPDs. GPDs, therefore, bring the energy-momentum tensor matrix elements within experimental grasp through electromagnetic scattering. GPDs can be viewed as a hybrid of parton distributions (PDFs), form factors and distribution amplitudes. Experimentally, they can be accessed in exclusive processes such as deeply virtual Compton scattering or meson electroproduction. Determining GPDs is an important mission of the US Department of Energy (DOE) drawing global scientific interest. Experimental collaborations and facilities worldwide have been devoted to searching for these last unknowns of the nucleon, including HERMES at DESY, COMPASS at CERN, GSI in Europe, BELLE and JPAC in Japan, Halls A, B and C at Jefferson Laboratory, and PHENIX and STAR at RHIC (Brookhaven National Laboratory) in the US. The study of GPDs and their imaging, or nucleon femtography, has led both the QCD and hadronic physics community worldwide to propose building an Electron-Ion Collider (EIC) to further explore these quantities (Accardi *et al.*, 2016b). In Europe, CERN has plans for the LHeC, adding an electron accelerator to the existing LHC hadron accelerator. There are also Chinese plans for similar electron-ion colliders.

Analogous to the usual PDFs, GPDs parametrize the quark and gluon correlation functions involving matrix elements of operators at a lightlike separation between the parton fields,

$$W_{\Lambda\Lambda'}^{[\gamma^+]} = \frac{1}{2} \int \frac{dy^-}{2\pi} e^{ik^+y^-} \langle p', \Lambda' \mid \bar{\psi}\left(-\frac{y}{2}\right) \gamma^+ \mathcal{U}\left(-\frac{y}{2}, \frac{y}{2}\right) \psi\left(\frac{y}{2}\right) \mid p, \Lambda \rangle_{y^+=y_T=0}$$
$$= \frac{1}{2P^+} \langle p', \Lambda' \mid \gamma^+ H(x,\xi,t) + \frac{i\sigma^{+j}\Delta_j}{2M} E(x,\xi,t) \mid p, \Lambda \rangle \quad (21)$$

$$\widetilde{W}_{\Lambda\Lambda'}^{[\gamma^+\gamma_5]} = \frac{1}{2} \int \frac{dy^-}{2\pi} e^{ik^+y^-} \langle p', \Lambda' \mid \bar{\psi}\left(-\frac{y}{2}\right) \gamma^+\gamma_5 \mathcal{U}\left(-\frac{y}{2}, \frac{y}{2}\right) \psi\left(\frac{y}{2}\right) \mid p, \Lambda \rangle_{y^+=y_T=0}$$
$$= \frac{1}{2P^+} \langle p', \Lambda' \mid \gamma^+\gamma_5 \widetilde{H}(x,\xi,t) + \frac{\gamma_5\Delta^+}{2M} \widetilde{E}(x,\xi,t) \mid p, \Lambda \rangle. \quad (22)$$

Two additional kinematic variables enter their definition besides the quark light cone longitudinal momentum fraction, $x = k^+/P^+$ (with $P = (p + p')/2$): the light cone component of the longitudinal momentum transfer between the initial and final proton, $\xi = -\Delta^+/(2P^+) \approx x_{Bj}/(2 - x_{Bj}) > 0$ (with $\Delta = p' - p$), and the transverse component, $\boldsymbol{\Delta}_T = \mathbf{p}'_T - \mathbf{p}_T$; the latter is taken into account through the invariant, $t = \Delta^2 = M^2\xi^2/(1 - \xi^2) - \Delta_T^2/(1 - \xi^2), t < 0$. At leading (twist-two) level, four quark chirality conserving (chiral even) GPDs, H, E, $\widetilde{H}$ and $\widetilde{E}$, defined in Eqs. (21) and (22), parametrize the quark-proton correlation functions.

Like the PDFs, GPDs are nonperturbative parton-hadron correlation functions. They are not direct physical observables, since no quark or gluon has been observed in isolation, owing to QCD color confinement.

Lattice QCD cannot calculate GPDs directly, since they are defined in terms of operators with lightlike separation between the parton fields. GPDs are connected to various physical observables through QCD factorization. For example, the deeply virtual Compton scattering (DVCS) cross section can be expressed in terms of Compton form factors (CFFs) which are factorized into GPDs convoluted over the variable x with perturbatively calculated short-distance coefficient functions (Belitsky and Radyushkin, 2005; Diehl, 2003; Goeke *et al.*, 2001; Kumericki *et al.*, 2016). In addition to the four chiral even GPDs, we have four more quark-flip/chiral odd GPDs, H_T, E_T, $\widetilde{H}_T$ and $\widetilde{E}_T$ and four gluon GPDs, H_g, E_g, $\widetilde{H}_g$ and $\widetilde{E}_g$. The latter can be singled out in deeply virtual meson-production experiments.

While several deeply virtual exclusive experiments

performed in the past decade are affected by large theoretical and experimental uncertainties on the CFFs (see (Kumericki *et al.*, 2016) for a detailed list), the experimental program of Jefferson Lab at 12 GeV will allow us, in the next decade, to map out the complete helicity structure of the cross section (Kriesten *et al.*, 2020), making it possible to extract GPDs in the quark sector with sufficiently high precision. Looking into the future, the upcoming EIC will be instead focused on low x, providing a unique probe of the gluon GPDs.

Deeply virtual exclusive processes are measured in coincidence experiments where all the particles in the final state are either directly or indirectly detected. Extracting GPDs from data involves a much larger number of variables than extracting PDFs. Furthermore, each experiment can only add a small piece to the picture. This makes it very difficult, if not impossible, to extract GPDs from experiment with the high-precision required to obtain images at the femtoscale (femtography), using traditional global-fitting methods. More sophisticated analyses are being developed working towards this goal, and a major research effort has been focused on applying machine-learning tools to the extraction of GPDs from data (Sec. III.5).

III.2. Status of GPD calculations

A lot of activity and progress has been recently dedicated to extracting information on GPDs from lattice QCD calculations as reported in detail in Sections III.3, III.4. In addition, several models/parametric forms have been developed that, on one side, facilitate the comparison with experimental data and, on the other, allow us to identify new deeply virtual exclusive observables that can be factorized in terms of GPDs. The main efforts in this direction include the light-front overlap representation (Chouika *et al.*, 2017a) used in the PARTON analysis (Berthou *et al.*, 2018), the reggeized diquark model (Gonzalez-Hernandez *et al.*, 2013) used in the recent effort in Ref.(Kriesten *et al.*, 2020), conformal moments based models (Müller *et al.*, 2014) used in the analysis of Refs.(Kumericki *et al.*, 2011; Kumerički and Müller, 2016), as well as parametrizations based on double distributions (Goloskokov and Kroll, 2008).

To be able to rely on a variety of models is particularly important for the study of GPDs because of the additional constraints that have to be satisfied as compared to PDFs and other one-dimensional quantities. Time reversal and Parity conservation generate discrete symmetries obeyed by GPDs for $\xi \to -\xi$, $x \to -x$; Lorentz invariance generates the property of polynomiality, namely that the x^j moments of quark GPDs are even polynomials in ξ, and that x^{j-1} moments of gluon GPDs are even polynomials in ξ (see also Section III.4.3); finally, from the norm of

the Hilbert space one obtains positivity constraints, or inequalities between GPDs and the corresponding PDFs (Belitsky and Radyushkin, 2005; Diehl, 2003; Kumericki *et al.*, 2016). The behavior of GPDs, including their perturbative evolution, under these constraints can be tracked down and monitored using models.

The wealth of GPD phenomenology combined with its intrinsic difficulty has pushed several groups of theorists and phenomenologists to develop frameworks dedicated to the extraction of GPDs and of the 3D structure of the nucleon from experimental data. In Section III.5 we describe platforms that are currently been used for data interpretation.

III.3. Moments of GPD from lattice QCD

A widely-used approach to extract information of GPDs on the lattice is via an operator product expansion. Based on this approach, the resulting local operators can be inserted between hadronic matrix elements, which are calculable in lattice QCD. The Mellin moments, obtained from such matrix elements, provide important information on the structure of the hadron under study, and can be compared against phenomenological fits of experimental data. The moments of GPDs are a generalization of the moments of PDF with a nonzero momentum transfer between the initial and final state: form factors and generalized form factors, expressed in terms of the momentum transferred squared, Q^2. Form factors (FFs) have been studied intensively for many years in lattice QCD due to many decades of scattering experimental results that one can compare with, and recent interests in proton radius puzzles with all possible theoretical calculations. On the other hand, there are less interests in the generalized form factors (GFFs) which can be challenging to extract and reduce the systematic uncertainties. Lack of reliable extraction of GFF experimental data has also put many lattice collaboration to diverge their resources elsewhere. With the exciting results coming out of JLab 12GeV program and other future colliders, one expect more GFFs lattice calculations in the near future.

III.3.1. Nucleon electromagnetic form factors

The most commonly calculated form factors are the nucleon isovector electromagnetic form factors, defined by

$$\langle N(p_f)|V_\mu^+(x)|N(p_i)\rangle =$$
$$\bar{u}^N \left[\gamma_\mu F_1(q^2) + i\sigma_{\mu\nu} \frac{q^\nu}{2M_N} F_2(q^2) \right] u_N e^{iq\cdot x}, \qquad (23)$$

where the isovector current is $V_\mu^+(x) = \bar{u}\gamma_\mu u - \bar{d}\gamma_\mu d$ and F_1 and F_2 are Dirac and Pauli form factors,

respectively. The Sachs electric and magnetic form factors can be obtained from $F_{1,2}$ as $G_E(q^2) = F_1(q^2) + q^2 F_2(q^2)/(2M_N)^2$ and $G_M(q^2) = F_1(q^2) + F_2(q^2)$, which correspond to the Fourier transforms of nucleon charge and magnetization density distributions in the Breit frame. Inspired by the decades of continuous experimental measurements, there are many calculations at physical pion mass for the electromagnetic form factors In Fig. 18, only selected results from near-physical pion masses are shown. PACS has the largest volume among these calculations and is able to probe the smallest Q^2. The parameters of the lattice calculations are summarized in Table XI. Overall, the lattice-QCD results among different collaborations are in good agreement within 1-2 standard deviations. The magnetic form factors have reasonable agreement with the experimental ones, but the electric form factors, depending on the analysis approach, have a small tension. With more precision experimental electric form factors on their way to resolve the proton radius puzzle, it would be desirable to have lattice form factors at the percent level. To achieve this, one will need to include QED and isospin symmetry breaking in the lattice calculation, which will require significantly more computational resources, as well as new techniques.

Besides the progress in the calculation of the connected contributions to the electromagnetic form factors, there have been advances in the evaluation of their disconnected (light and strange quark) contributions. The latter result from the self-contractions of the inserted operator, that is, its quark and anti-quark of same flavor contract with each other. Approximately speaking, the operator couples to the hadron via gluons, and are often viewed as sea quark contributions. This allows a u- and d-quark decomposition and the proper extraction of the proton and neutron electromagnetic form factors via:

$$G^p(Q^2) = \frac{1}{2}\left(\frac{1}{3}G^{u+d}(Q^2) + G^{u-d}(Q^2)\right), \quad (24)$$

$$G^n(Q^2) = \frac{1}{2}\left(\frac{1}{3}G^{u+d}(Q^2) - G^{u-d}(Q^2)\right). \quad (25)$$

The isoscalar combination in the above equations should be the sum of both connected and disconnected contributions. The electric and magnetic proton form factors including both connected and disconnected diagrams have been calculated by ETMC using twisted mass fermions (TM) ensembles ($N_f = 2$ and $N_f = 2 + 1 + 1$) with different volumes and can be found in Ref. (Alexandrou *et al.*, 2019a). Here we show the neutron form factors in Fig. 19 for the most accurate data of ETMC at a volume with $L = 5.12$ fm (red circles), which are compared against experimental data shown with black crosses. The data are taken from Refs. (Becker *et al.*, 1999; Bermuth *et al.*, 2003; Eden *et al.*, 1994; Glazier *et al.*, 2005; Golak *et al.*, 2001; Herberg *et al.*, 1999; Madey *et al.*, 2003; Meyerhoff
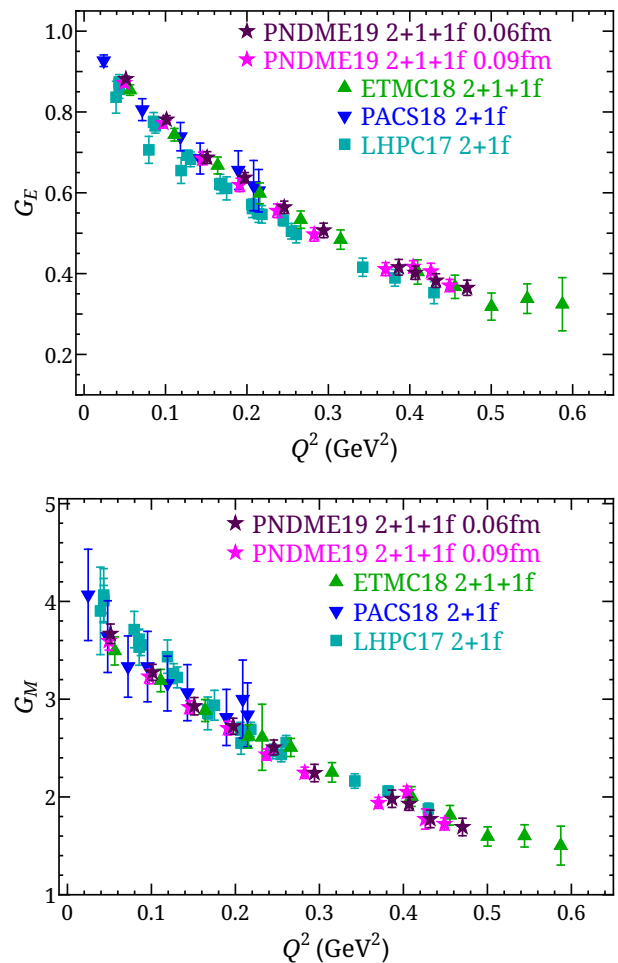

FIG. 18 Selected nucleon isovector electric (left) and magnetic (right) form factor results from near physical pion mass as functions of transferred momentum Q^2. The references corresponding to the above works are: 2f ETMC18 (Alexandrou *et al.*, 2017c) 2+1f LHPC14 (Green *et al.*, 2014), LHPC17 (Hasan *et al.*, 2018), PACS18 (Shintani *et al.*, 2019); 2+1+1f ETMC18 (Alexandrou *et al.*, 2019a), PNDME19 (Jang *et al.*, 2018) with 2 lattice spacings of 0.06 and 0.09 fm.

et al., 1994; Ostrick *et al.*, 1999; Passchier *et al.*, 1999; Plaster *et al.*, 2006; Rohe *et al.*, 1999; Schiavilla and Sick, 2001; Warren *et al.*, 2004; Zhu *et al.*, 2001) for the electric form factor and from Refs. (Alarcon, 2007; Anderson *et al.*, 2007; Anklin *et al.*, 1994, 1998; Gao *et al.*, 1994; Kubon *et al.*, 2002) for the magnetic form factor. There is a very good agreement between lattice and experiment, with exception the small-Q^2 for G_M^n. Note that the experimental data have, in general, larger uncertainties as compared to the lattice data. We want to emphasize that, such comparison is considered a success for lattice QCD, as it is the first time that the proton and neutron electromagnetic form factors include both connected and disconnected contributions. Such a plot is

Ref.	Sea quarks	Valence quarks	Renormalization	$N_{\Delta t}$	a (fm)	M_π (MeV)	$M_\pi L$
ETMC'18 (Alexandrou *et al.*, 2019a)	2f & 2+1+1f TM	twisted mass	RI'-MOM	3	0.080, 0.094	130-139 MeV	3.0–4.0
ETMC'17 (Alexandrou *et al.*, 2017c)	2f TM	twisted mass	RI'-MOM	3	0.094	130 MeV	3.0
LHPC'14 (Green *et al.*, 2014)	2+1f clover	clover	Schrödinger functional	3	0.09–0.116	149–356	3.6–5.0
LHPC'17 (Hasan *et al.*, 2018)	2+1f clover	clover	vector charge	3	0.093	135	4.0
PACS'18 (Shintani *et al.*, 2019)	2+1f clover	clover	Schrödinger functional	4	0.085	146	8.0
PNDME'19 (Jang *et al.*, 2018)	2+1+1f HISQ	clover	RI-MOM	4	0.09	138	3.9

TABLE XI   The lattice parameters used in calculations of the electromagnetic form factors near physical pion mass. $N_{\Delta t}$ indicates the number of source-sink separation used in the lattice calculation to control the "excited-state" systematics which can be significant for nucleon structure.

a representative example of the state-of-the-art of lattice QCD for calculation of form factors.
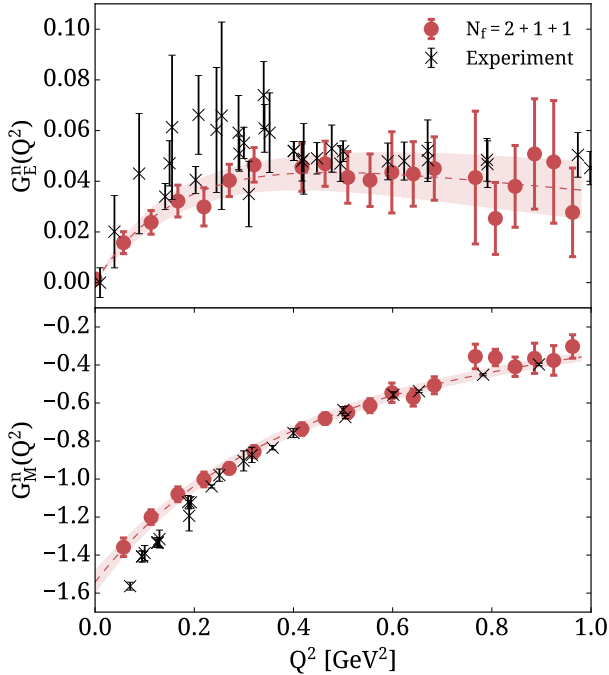
FIG. 19 Neutron electric (top) and magnetic (bottom) form factors as a function of Q^2. Lattice data are shown with red circles obtained by ETMC (Alexandrou *et al.*, 2019a). Experimental data are shown with black stars.

The contributions of strange sea quarks to the nucleon electromagnetic form factors has been of high interest in the last decades. Experimentally, strange electromagnetic form factors can be extracted through the parity-violating asymmetry in the elastic scattering of polarized electrons on unpolarized protons. However, these experimental measurements are difficult and precision determinations of the form factors are not yet available. This is one place where lattice-QCD calculations can provide better results with currently available computational resources. A number of collaborations have studied the strange electromagnetic form factors with lattice QCD (Alexandrou *et al.*, 2020a, 2018d; Babich *et al.*, 2012; Djukanovic *et al.*, 2019;

Doi *et al.*, 2009; Green *et al.*, 2015; Sufian *et al.*, 2017); the details of these calculations can be found in Table XII. Using the form factors' dependence on transfer-momentum (Q), the electric and magnetic radii, as well as the magnetic moment, are obtained via

$$\langle r_{E,M}^2 \rangle^s = -6 \frac{dG_{E,M}^s(Q^2)}{dQ^2}\Big|_{Q^2=0}, \quad \mu^s \equiv G_M^s(0). \quad (26)$$

We summarize the calculations using dynamical sea quarks in Fig. 20. Early studies only used only one ensemble with heavy pion masses to reduce computational costs. There has been great progress made in recent years, including calculations made directly at physical pion mass, such as ETMC's $Nf = 2+1+1$ work in Ref. (Alexandrou *et al.*, 2020a). χQCD (Sufian *et al.*, 2017) used four ensembles of valence overlap fermions on $N_f = 2+1$ domain wall configurations with multiple volumes, lattice spacings, and pion masses to investigate systematic uncertainties. The Mainz group (Djukanovic *et al.*, 2019) used $N_f = 2+1$ flavors of $\mathcal{O}(a)$-improved Wilson fermions, and they also employed an $\mathcal{O}(a)$-improved vector operator, with lattice spacing as small as 0.05 fm. Overall, there is agreement among the lattice data, demonstrating that systematic uncertainties are under control. However, the χQCD result for the magnetic moment disagrees with the other lattice results, and this tension should be further investigated.

III.3.2. Nucleon isovector axial form factors

There has been also rapidly increasing interest in lattice-QCD nucleon axial form factors (G_A) calculations, a key input from the SM for neutrino physics; these form factors can be calculated in terms of the isovector axial current

$$\langle N(p_f)|A_\mu^+(x)|N(p_i)\rangle =$$
$$\bar{u}_N \left[\gamma_\mu\gamma_5 G_A(q^2) + iq_\mu\gamma_5 G_P(q^2)\right] u_N e^{iq\cdot x}. \quad (27)$$

Here, $q = p_f - p_i$ is the momentum transfer between the initial and final state of nucleon; and the isovector current is $A_\mu^+(x) = \bar{u}\gamma_\mu\gamma_5 u - \bar{d}\gamma_\mu\gamma_5 d$. $G_A(q^2)$ and
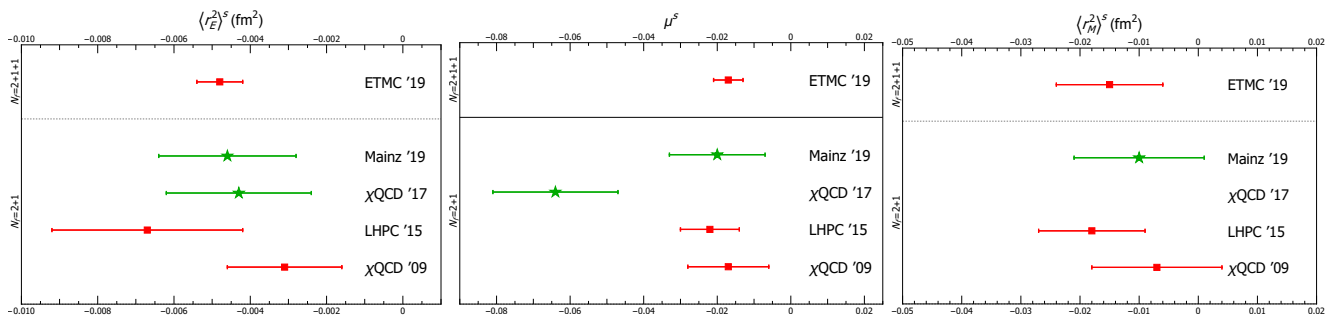
FIG. 20 Summary of lattice calculations of $\langle r_E^2 \rangle^s$ (left), μ^s (middle) and $\langle r_M^2 \rangle^s$ (right) from lattice ensembles with dynamical strange degrees of freedom in the sea. The green symbols show results using multiple ensembles to take the continuum limit $a \to 0$. Details of the lattice input can be found in Tab. XII.

Ref.	Sea quarks	Valence quarks	a (fm)	M_π (MeV)	$M_\pi L$
χQCD'09 (Doi et al., 2009)	2+1f clover	clover	0.12	600–840	5.97
BU'10 (Babich et al., 2012)	2+1f clover	clover	0.11	416	4.79
LHPC'15 (Green et al., 2015)	2+1f clover	clover	0.11	317	5.97
χQCD'16 (Sufian et al., 2017)	2+1f DWF	overlap	0.08–0.14	135–400	3.89–4.82
ETMC'18 (Alexandrou et al., 2018d)	2f twisted mass	twisted mass	0.09	130	2.98
Mainz'19 (Djukanovic et al., 2019)	2+1f clover	clover	0.05–0.09	200–360	4.14–5.35
ETMC'19 (Alexandrou et al., 2020a)	2+1+1f twisted mass	twisted mass	0.080	139	3.62

TABLE XII List of references and details of the lattice-QCD calculations of the nucleon strange form factors. Here, we omit the calculations using quenched approximation, perturbatively renormalized results, and conference proceedings.

$G_P(q^2)$ are known as nucleon axial and induced-pseudoscalar form factors, and $\bar{u}_N$ and u_N are the associated nucleon spinors. In the limit $|\vec{q}| \to 0$, $G_A(q^2 = 0)$ should recover the nucleon axial charge $g_A = -1.2723(23)$, which is well determined from neutron β-decay experiments (Tanabashi et al., 2018). Contrariwise, the axial-charge radius squared r_A^2 is less known; once $G_A(q^2)$ is obtained, one can obtain the radius via

$$r_A^2 \equiv \frac{6}{G_A(0)} \left. \frac{dG_A}{dq^2} \right|_{q^2=0}. \tag{28}$$

Although the first lattice-QCD calculation of the isovector nucleon axial form factors can be traced back to the early '90s, there has been significant progress and improvement by the global lattice community. One of the systematics, excited-state contamination, was not consistently addressed 10 years ago, which resulted in a lower nucleon axial coupling g_A and the wrong form factors. Removing this systematic has become essential for any lattice-QCD nucleon calculation. Another exciting breakthrough in the past decade is the increasing number of lattice nucleon calculations at the physical pion mass, mostly due to recent advances in both algorithms and a worldwide investment in pursuing the first exascale computing machine. Many calculations now comes with high statistics ($\mathcal{O}(100k)$ measurements)

and some with multiple lattice spacings and volumes to control lattice artifacts. Such programs would have been impossible 5 years ago. Figure 21 gives a summary of the recent nucleon axial form factors done near the physical pion mass, and the status of lattice-QCD calculations and examples of the phenomenological determinations of r_A^2 are shown on the right-hand side of Fig. 21. The parameters for each ensemble employed are given in Table XIII. The analysis with the z expansion (Meyer et al., 2016) eliminates the uncertainty estimates of determinations predicated on the dipole form. The model-independent results (red; between the horizontal lines) illustrate the best estimate of r_A^2 without such strong assumptions.

III.3.3. Nucleon isovector generalized form factors

There has been lattice-QCD efforts in moments of GPDs calculations in the past few decades, and in recent years, there has been emerging direct physical pion mass calculation. A common lattice approach is to use the operator product expansion to local operators with the nucleon matrix. Most calculations focusing on the leading-twist operators, computing isovector nucleon matrix elements of the one-derivative operators to obtained the generalized form factors (A_{20}, B_{20}, C_{20}, $\tilde{A}_{20}$, $\tilde{B}_{20}$, $\tilde{C}_{20}$) though:
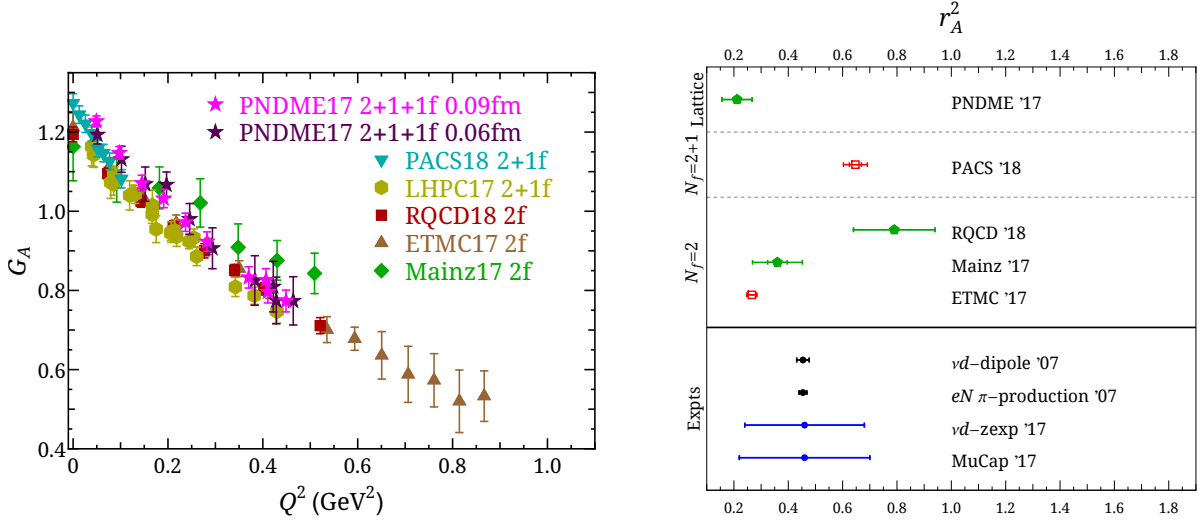
FIG. 21   Left: nucleon isovector axial form factor as functions of q^2. Right: summary of r_A^2 from calculations on ensembles near physical pion mass (Alexandrou *et al.*, 2017b; Bali *et al.*, 2019a; Capitani *et al.*, 2019; Gupta *et al.*, 2017; Hasan *et al.*, 2018; Shintani *et al.*, 2019), together with non-lattice determinations. The color code for r_A^2 is adapted from the Flavor Lattice Averaging Group (Aoki *et al.*, 2017), as specified in the Appendix of Ref. (Bhattacharya *et al.*, 2015). The legends and references for r_A^2 are as follows: νd (dipole) and $eN \to eN'\pi$ (Bodek *et al.*, 2008), νd (z expansion) (Meyer *et al.*, 2016), "MuCap" (Hill *et al.*, 2018).

Ref.	Sea quarks	Valence quarks	Renormalization	$N_{\Delta t}$	a (fm)	M_π (MeV)	$M_\pi L$
ETMC '17 (Alexandrou *et al.*, 2017b)	2f twisted mass	twisted mass	RI'-MOM	3	0.094	130 MeV	3.0
LHPC '17 (Hasan *et al.*, 2018)	2+1f clover	clover	RI'-MOM	3	0.093	135 MeV	4.0
Mainz '17 (Capitani *et al.*, 2019)	2f clover	clover	Schrödinger functional	4–6	0.05–0.08	193– 73	4.0–6.0
PACS '18 (Shintani *et al.*, 2019)	2+1f clover	clover	Schrödinger functional	4	0.085	146	8.0
PNDME '17 (Gupta *et al.*, 2017)	2+1+1f HISQ	clover	RI'-MOM	3–4	0.06–0.12	130–320	3.7–5.5
RQCD '18 (Bali *et al.*, 2019a)	2f clover	clover	RI'-MOM	2–6	0.06–0.08	150–490	3.4–6.7

TABLE XIII   The lattice parameters used in the near physical pion mass axial form-factor calculations

$$\langle N(p',s')|\mathcal{O}_V^{\mu\nu}|N(p,s)\rangle = \bar{u}_N(p',s')\frac{1}{2}\Big[A_{20}(q^2)\,\gamma^{\{\mu}P^{\nu\}} + B_{20}(q^2)\,\frac{i\sigma^{\{\mu\alpha}q_\alpha P^{\nu\}}}{2m_N} + C_{20}(q^2)\,\frac{1}{m_N}q^{\{\mu}q^{\nu\}}\Big]u_N(p,s),$$

$$\langle N(p',s')|\mathcal{O}_A^{\mu\nu}|N(p,s)\rangle = \bar{u}_N(p',s')\frac{i}{2}\Big[\tilde{A}_{20}(q^2)\,\gamma^{\{\mu}P^{\nu\}}\gamma^5 + \tilde{B}_{20}(q^2)\,\frac{q^{\{\mu}P^{\nu\}}}{2m_N}\gamma^5\Big]u_N(p,s), \tag{29}$$

where u_N are nucleon spinors, $q = p'-p$ is the momentum transfer, $P = (p'+p)/2$, m_N is the nucleon mass, and operators

$$\mathcal{O}_V^{\mu\nu} = \bar{\psi}\gamma^{\{\mu}\overleftrightarrow{D}^{\nu\}}\frac{\tau^3}{2}\psi,$$

$$\mathcal{O}_A^{\mu\nu} = \bar{\psi}\gamma_5\gamma^{\{\mu}\overleftrightarrow{D}^{\nu\}}\frac{\tau^3}{2}\psi, \text{ and} \tag{30}$$

where ψ ($\bar{\psi}$) are (anti-)light quark flavor, τ^3 as Pauli matrix, and the curly (square) brackets denote symmetrization (antisymmetrization)

$$\overleftrightarrow{D}_\mu = \frac{1}{2}(\overrightarrow{D}_\mu - \overleftarrow{D}_\mu), \; D_\mu = \frac{1}{2}(\nabla_\mu + \nabla_\mu^*) \tag{31}$$

with ∇_μ (∇_μ^*) denoting the forward (backward) derivatives on the lattice. For space limitations, we do not include the decomposition of the tensor current ($\mathcal{O}_T^{\mu\nu\rho}$), which leads to the GFFs A_{T20}, B_{T20}, C_{T20}, as we do not present any results here.

These nucleon matrix elements can be expanded in terms of generalized form factors (GFFs), which are Lorentz invariant functions of the momentum transfer squared. At zero momentum transfer, these nucleon matrix elements yield the second Mellin moments of the unpolarized, helicity and transversity PDFs. There are very limited calculations on the generalized form factors, as can be seen in Table XIV. In this summary

we exclude calculations using quenched approximation, perturbatively renormalized results, as well as conference proceedings. In Fig. reffig:LatGFF we give the results obtain with simulations at the physical point by ETMC using three ensembles (Alexandrou *et al.*, 2020c), and the near physical point calculation or RQCD (Bali *et al.*, 2019b). We show the unpolarized GFFs (A_{20}, B_{20}) and the linearly polarized GFFs ($\tilde{A}_{20}$, $\tilde{B}_{20}$). The unpolarized GFF C_{20} is found consistent with zero and, thus, not shown here. It is interesting to observe that the two data sets for A_{20} in the ETMC calculation exhibit some tension. This is an indication of systematic uncertainties. Given that the blue points correspond to finer lattice spacing, and larger volume and larger $m_\pi L$ value, we expect that the blue points have suppressed systematic uncertainties. Both ensembles of ETMC lead to compatible results for the remaining GFFs. The comparison between the $N_f = 2$ ETMC data and $N_f = 2$ RQCD data reveals agreement for A_{20}, B_{20} and $\tilde{B}_{20}$. However, the RQCD data have a different slope than the ETMC data, which is attributed to the different analysis methods, and systematic uncertainties.

III.4. x-dependent GPDs from lattice QCD

Information on GPDs from lattice QCD has been available via their form factors and generalized form factors, using Operator Product Expansion (OPE). As in the case of PDFs, such information is limited due to suppression of the signal as the order of the Mellin moments increases, but also as the momentum transfer between the initial and final state increases.

Significant progress has been made towards new methods to access the x- and t-dependence of GPDs ($t = -Q^2$), which is driven by the advances in the calculations of PDFs presented in Sec. II.2. Here we present the methodology for obtaining GPDs from the lattice using the quasi- and pseudo-distributions approach, as well as first results for the nucleon and pion GPDs.

III.4.1. GPDs using the quasi-distribution approach

In the quasi-distribution approach, GPDs can be extracted in the same way as extracting PDFs, except that one needs to take into account the off-forward kinematics. For the unpolarized quark GPDs in the nucleon defined by Eq. (21) for the unpolarized case. On the lattice we can calculate the so-called quasi-GPDs

$$\tilde{F}(x, \tilde{\xi}, t, \bar{P}_3) = \frac{\bar{P}_3}{\bar{P}^0} \int \frac{dz}{4\pi} e^{ixz\bar{P}_3} \langle P' | \tilde{O}_{\gamma^0}(z) | P \rangle$$
$$= \frac{\bar{u}(P')}{2\bar{P}^0} \left\{ \widetilde{H}(x, \tilde{\xi}, t, \bar{P}_3)\gamma^0 + \widetilde{E}(x, \tilde{\xi}, t, \bar{P}_3)\frac{i\sigma^{0\mu}\Delta_\mu}{2M} \right\} u(P),$$
$$(32)$$

as Eq. (21) is not accessible on a Euclidean lattice. The skewness is replaced by the quasi-skewness

$$\tilde{\xi} = -\frac{P'_3 - P_3}{P'_3 + P_3} = -\frac{\Delta_3}{2\bar{P}_3} = \xi + \mathcal{O}\left(\frac{M^2}{(\bar{P}_3)^2}, \frac{t}{(\bar{P}_3)^2}\right) \quad (33)$$

differs from the light-cone skewness ξ by power suppressed corrections. It can be replaced by $\tilde{\xi}$ with the difference being attributed to generic power corrections. Then the quasi-GPDs can be factorized into the GPDs as (Ji *et al.*, 2015a; Liu *et al.*, 2019)

$$\tilde{F}(y, \xi, t, \bar{P}_3, \mu)$$
$$= \int_{-1}^{1} \frac{dx}{|\xi|} C\left(\frac{y}{\xi}, \frac{x}{\xi}, \frac{\mu}{\xi\bar{P}_3}\right) F(x, \xi, t, \mu) + \dots, \quad (34)$$

where $\dots$ denotes power corrections of the form $\mathcal{O}(M^2/\bar{P}_3^2, t/\bar{P}_3^2, \Lambda_{\text{QCD}}^2/(y^2\bar{P}_3^2))$.

Prior to lattice calculations, quasi-GPDs have been studied in models, which provides a qualitative qualitative understanding of GPDs. In Ref. (Bhattacharya *et al.*, 2019b) the quasi-GPDs are studied in the scalar diquark spectator model. Among other, some robust features of quasi-GPDs were revealed concerning the behavior at large x, the behavior around the cross-over points $x = \pm\xi$, as well as their behavior in the ERBL region. In the follow-up work presented in Ref.(Bhattacharya *et al.*, 2019a) the Authors findings include two model-independent results that are interesting for lattice calculations. This regards a discussion of the moments of quasi-GPDs (and quasi-PDFs), and the behavior of quasi-GPDs under $\xi \to -\xi$. While for light-cone GPDs the ξ-symmetry has been of academic interest, for the quasi-GPDs this point could potentially be of practical relevance to decrease statistical uncertainties in lattice calculations.

In lattice QCD, there are several challenges in calculating quasi-GPDs. In contrast with the PDFs, the extraction of GPDs is more challenging because they require momentum transfer, Q^2, between the initial (source) and final (sink) states. Another complication is the fact that the GPDs are defined in the Breit frame, in which the momentum transfer is equally distributed to the initial and final states.

Working in the Breit frame has no conceptual difficulty, however, it increases the computational cost, as separate calculations are necessary for each value of the momentum transfer. The bare matrix element

$$N(P3+Q/2)|\bar{\psi}(z)\Gamma W(0, z)\psi(0)|N(P_3-Q/2)\rangle \quad (35)$$

is calculated using the techniques developed for PDFs, and the use of momentum smearing method (Bali *et al.*, 2016),

Another factor that increases the computational cost is the need of an optimized ratio of 3pt- and 2pt-functions,

Ref.	Sea quarks	Valence quarks	Renormalization	$N_{\Delta t}$	a (fm)	M_π (MeV)	$M_\pi L$
ETMC '19 (Alexandrou *et al.*, 2020c)	2f & 2+1+1f TM	twisted mass	RI'-MOM	3	0.080, 0.094	130–139 MeV	3.0–4.0
ETMC '13 (Alexandrou *et al.*, 2013)	2+1+1f twisted mass	twisted mass	RI'-MOM	1	0.06–0.08	210,370	3.4–5.0
ETMC '11 (Alexandrou *et al.*, 2011)	2f twisted mass	twisted mass	RI'-MOM	1	0.056–0.089	262–470	3.3–5.3
LHPC '10 (Bratt *et al.*, 2010)	2+1f Astad	domain wall	RI'-MOM	1	0.124	293–596	3.7–7.5
LHPC '07 (Hagler *et al.*, 2008)	2+1f staggered	domain wall	RI'-MOM	1	0.124	350–760	4.4–9.6
RQCD '19 (Bali *et al.*, 2019b)	2f clover	clover	RI'-MOM	1–6	0.060–0.081	150–490	2.8–6.7

TABLE XIV   List of references and details of the lattice-QCD moments of generalized form factors calculations. Here we omit the calculations using quenched approximation, perturbatively renormalized results, and conference proceedings.
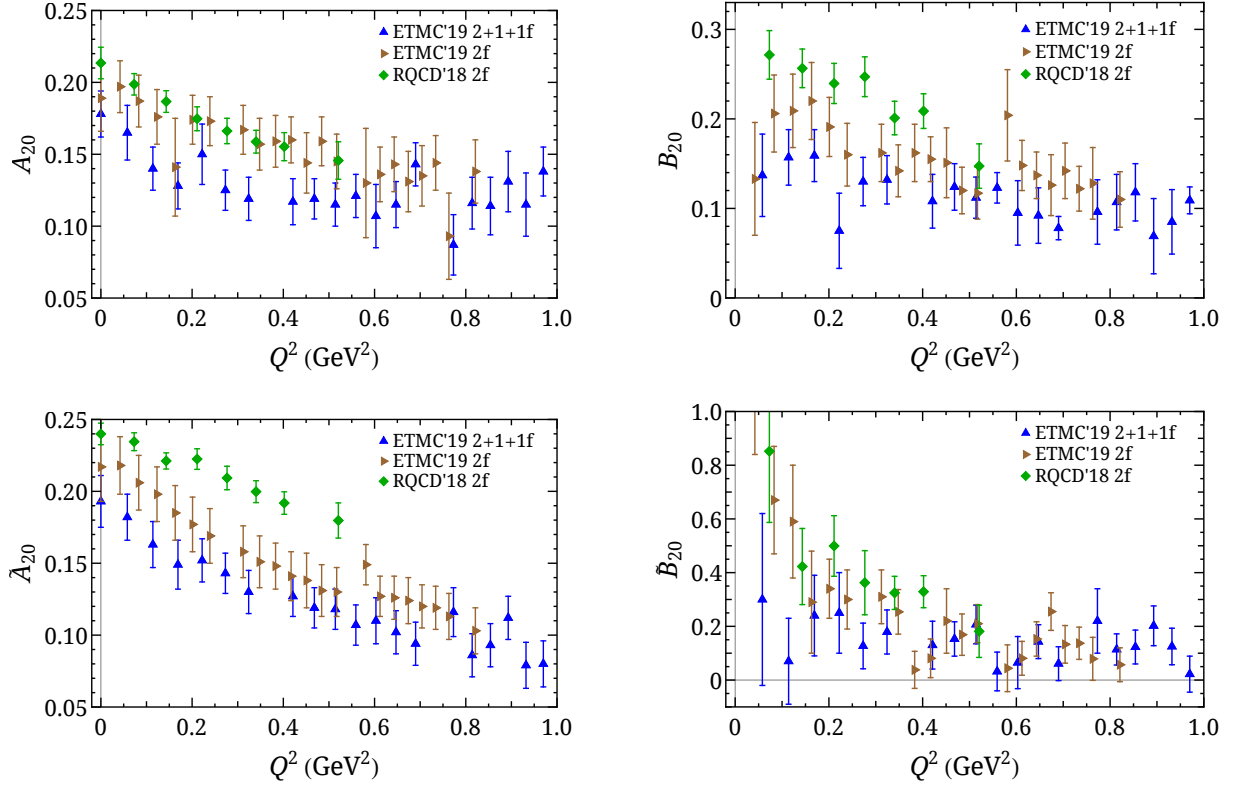
FIG. 22   Unpolarized (left) and linearly polarized (right) nucleon isovector GFFs from near physical pion mass as functions of transferred momentum Q^2. The references corresponding to the above works are: 2+1+1f ETMC19 (Alexandrou *et al.*, 2020c), 2f ETMC19 (Alexandrou *et al.*, 2020c) (only the larger-volume results is quoted here), 2f RQCD19 (Bali *et al.*, 2019b).

that is:

$$R_{\mathcal{O}}(\Gamma; \vec{p}', \vec{p}; t_s, t_{in}) = \frac{C^{3pt}(\Gamma; \vec{p}', \vec{p}; t_s, t_{in})}{C^{2pt}(\Gamma_0; \vec{p}', t_{in})} \times$$

$$\sqrt{\frac{C^{2pt}(\Gamma_0; \vec{p}, t_s - t_{in})\, C^{2pt}(\Gamma_0; \vec{p}', t_{in})\, C^{2pt}(\Gamma_0; \vec{p}', t_s)}{C^{2pt}(\Gamma_0; \vec{p}', t_s - t_{in})\, C^{2pt}(\Gamma_0; \vec{p}, t_{ins})\, C^{2pt}(\Gamma_0; \vec{p}, t_s)}} \quad (36)$$

As can be seen, one needs to calculate the 2pt-functions with momentum boost equal to the source momentum, as well as, the sink momentum. The momentum smearing method is applied on the 2pt-functions, with the exponent of the additional phase, being in parallel to the direction of the momentum boost. In addition to the above, different projectors are needed (for baryons) to disentangle the GPDs.

The aforementioned matrix elements decompose into two form factors, which after the Fourier transform and the matching lead to the light-cone GPDs H, E for the unpolarized case, and $\widetilde{H}$, $\widetilde{E}$ for the helicity case. Therefore one can extract their x dependence at each value of P_3 and momentum transfer. For GPDs, so-called ERBL region is defined for $\xi \neq 0$, via $|x| < \xi$. As discussed in Ref. (Liu *et al.*, 2019), the matching for $\xi = 0$ is the same as the one for PDFs, while $\xi \neq 0$ requires different matching, which is derived in Ref. (Liu *et al.*, 2019) using an RI-type scheme.

To date there has been one calculation for the nucleon GPDs by ETMC, and one for the pion GPDs (Chen *et al.*, 2019b). The former uses one ensemble of $N_f = $
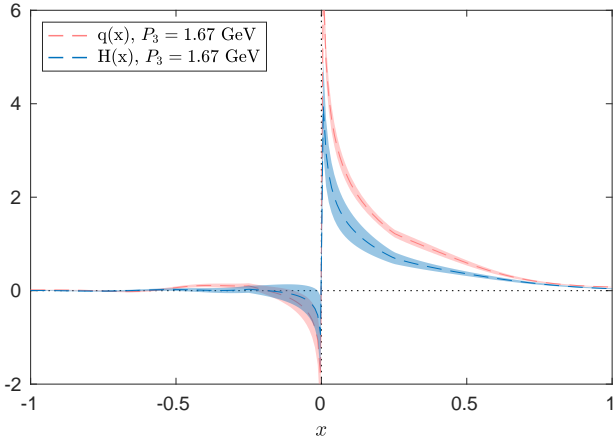
FIG. 23 H-GPD for $P_3 = 1.67$ GeV, $Q^2 = 0.69$ GeV^2, and $\xi = 0$, obtained by the ETM Collaboration.
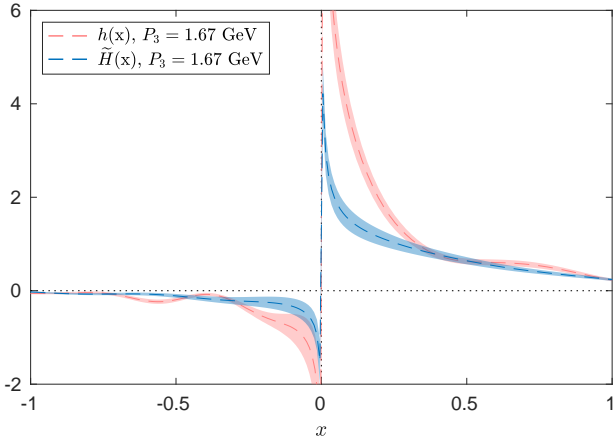

FIG. 24 $\widetilde{H}$-GPD for $P_3 = 1.67$ GeV, $Q^2 = 0.69$ GeV^2, and $\xi = 0$, obtained by the ETM Collaboration.

$2 + 1 + 1$ gauge configurations at a pion mass of 260 MeV. Part of these results have been presented in Ref. (Alexandrou *et al.*, 2019c). This work presents results of the unpolarized and helicity GPDs, for both $\xi = 0$ and $\xi \neq 0$. Here we give results for the GPDs at $\xi = 0$. Note that $\widetilde{E}$-GPD cannot be accessed in this case, as its kinematic factor becomes zero. Fig. 23 compares the H-GPD at $Q^2 = 0.69$ GeV^2 with the unpolarized PDF, in order to see the effect of nonzero Q^2. The momentum boost is 1.67 GeV^2 for both cases. One can see that the H-GPD is suppressed as compared to the PDF, especially in all regions of x. A similar comparison can be seen in Fig. 24 for the $\widetilde{H}$-GPD and the helicity PDF, for $P_3 = 1.67$ GeV. Similar to the case of the H-GPD, the introduction of the momentum transfer suppresses the GPD, as expected from the behavior of the form factors and generalized form factors. For the intermediate- to large-x region we find that the H-GPD is compatible with the helicity PDF.

In (Chen *et al.*, 2019b), the pion valence quark GPD
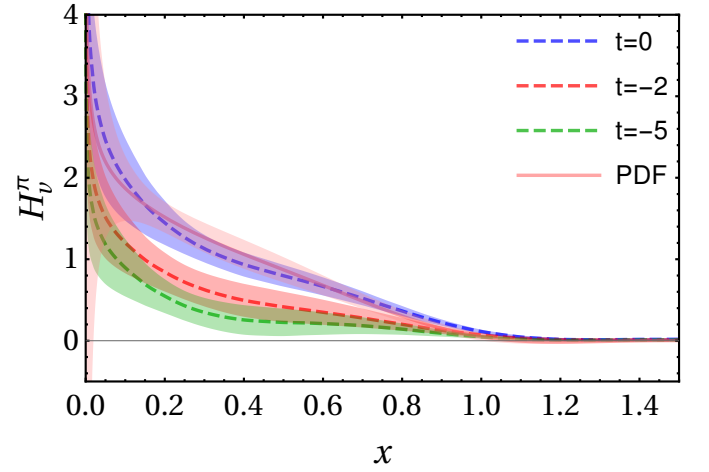
FIG. 25   The zero-skewness pion valence quark GPD $H_v^{\pi^+}(x, \xi = 0, t, \mu = 4\text{GeV})$ for $t = \{0, -2, -5\}(2\pi/L)^2$ after one-loop matching and the meson-mass correction. "PDF" denotes the pion PDF result in Ref. (Zhang *et al.*, 2019a).

at zero skewness was calculated using clover valence fermions on an ensemble of gauge configurations with $2 + 1 + 1$ flavors (degenerate up/down, strange and charm) of highly improved staggered quarks (HISQ) with lattice spacing $a \approx 0.12$ fm, box size $L \approx 3$ fm and pion mass $m_\pi \approx 310$ MeV. The result is shown in Fig. 25. It turns out that, with current uncertainties, the result does not show a clear preference among different model assumptions about the kinematic dependence of the GPD. To disentangle different models, further studies using higher-statistics data will be crucial.

III.4.2. GPDs using pseudo-distribution approach

The generalization of the pseudo-distributions approach to include GPDs was developed recently (Radyushkin, 2019a). For lattice applications, and the discussion presented here we choose $z = z_3$ without loss of generality. Decomposing the hadron momenta p_1 and p_2 into $p_1 = \{E_1, \Delta_{1,\perp}, P_1\}$ and $p_2 = \{E_2, \Delta_{2,\perp}, P_2\}$, one deals with two Ioffe-time invariants $\nu_1 = P_1 z_3$ and $\nu_2 = P_2 z_3$.

The choice of operator γ^0 (instead of the alternative γ^3) eliminates the z^0 and $\Delta_\perp^0$ parts from the parametrization

$$\langle p_2 | \bar{\psi}(-z_3/2) \gamma^0 \dots \psi(z_3/2) | p_1 \rangle = 2\mathcal{P}^0 M(\nu_1, \nu_2, t; z_3^2) \tag{37}$$

defining the *double* Ioffe-time pseudodistribution $M(\nu_1, \nu_2, t; z_3^2)$. After denoting $\nu = (\nu_1 + \nu_2)/2$, the latter converts into the *generalized Ioffe-time pseudodistribution* (pseudo-GITD) $\mathcal{M}(\nu, \xi, t; z_3^2)$. To remove link-related UV divergences, one may introduce

the *reduced* pseudo-GITD (Radyushkin, 2019a)

$$\mathfrak{M}(\nu, \xi, t; z_3^2) \equiv \frac{\mathcal{M}(\nu, \xi, t; z_3^2)}{\mathcal{M}(0, 0, 0; z_3^2)} \ . \qquad (38)$$

For small z_3^2, it may be expressed (see Ref. (Radyushkin, 2019a)) in terms of the light-cone ITD

$$\mathcal{I}(\nu, \xi, t; \mu^2) \equiv \int_{-1}^{1} dx \, e^{ix\nu} \, H\left(x, \xi, t; \mu^2\right) \qquad (39)$$

by a perturbative matching relation that has the usual pQCD factorization form

$$\mathfrak{M}(\nu, \xi, t; z_3^2) = \int_{-1}^{1} dw \, C(w, \xi, z_3^2 \mu^2) \, \mathcal{I}(w\nu, \xi, t; \mu^2)$$
$$+ \, \mathcal{O}(z_3^2) \ . \qquad (40)$$

III.4.3. Extraction of GPDs from data using pseudo-distribution approach

To extract GPDs, it is proposed to model $\mathcal{I}(w\nu, \xi, t; \mu^2)$ from some parametrization for $H(x, \xi, t; \mu^2)$ (Radyushkin, 2019a), and fit its parameters using lattice data on $\mathfrak{M}(\nu, \xi, t; z_3^2)$. The *polynomiality* property (Ji, 1997; Müller *et al.*, 1994; Radyushkin, 1997) of GPDs may be efficiently taken into account by using the *double distribution Ansatz* (Radyushkin, 1999) in the GPD modeling.

An equivalent strategy is to convert (40) into a kernel relation (Cichy *et al.*, 2019; Radyushkin, 2019a,c)

$$\mathfrak{M}(\nu, \xi, t; z_3^2) = \int_{-1}^{1} dx \, R(x\nu, \xi, z_3^2 \mu^2) \, H(x, \xi, t; \mu^2)$$
$$+ \, \mathcal{O}(z_3^2) \qquad (41)$$

obtained by writing $\mathcal{I}(w\nu, \xi, t, \mu^2)$ in terms of $H(x, \xi, t; \mu^2)$ using Eq. (39). Note that Eq. (41) directly relates the light-cone GPD $H(x, \xi, t; \mu^2)$ with the lattice data on $\mathfrak{M}(\nu, \xi, t; z_3^2)$ through a perturbatively calculable kernel $R(x\nu, \xi, z_3^2\mu^2)$. Hence, no intermediaries (like quasi-PDFs) are needed in this approach.

To aid a quantitative analysis one can draw information from models. Building a relatively simple model to evaluate GPDs can help understanding some of the essential features of the pseudo-pdfs approach. For example, the reggeized diquark model (Gonzalez-Hernandez *et al.*, 2013) can be used to have a better understanding of the "off-the-light-cone" behavior of the PDFs/GPDs, and to put more stringent constraints on the onset of perturbative behavior in coordinate space. In models one has the flexibility to perform calculations that mimic the equal time constraint on the lattice. Instead of obtaining the usual light cone PDF, $f(x)$, using this procedure, one obtains the off-the-light-cone PDFs which are a function of k_3 and P_3. Upon performing the Fourier
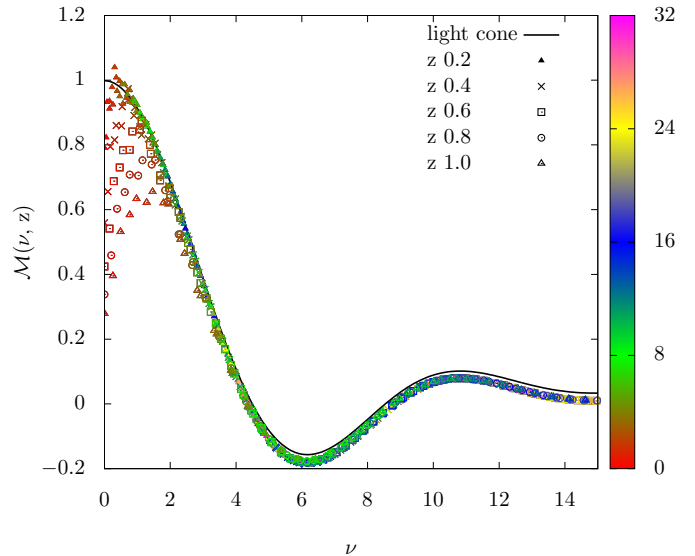

FIG. 26 The proton unpolarized u quark pseudo distribution normalized to one is shown for different values of quark field separation z in GeV^{-1}. P_3 is tagged from 0 to 32 GeV according to color. We see that at small Ioffe time ν, for lower values of P_3, the pseudo pdf deviates substantially from the expected Ioffe time behavior of the light cone parton distribution. The momentum space GPD used to evaluate the curves in this figure was obtained using the reggeized diquark model from Ref. (Gonzalez-Hernandez *et al.*, 2013).

transform in k_3 one obtains the Ioffe time distributions which are now a function of z and P_3 or, equivalently, the two Lorentz scalars $P \cdot z$ and z^2. One expects that as z^2 tends to zero and P_3 increases the pseudo Ioffe time distribution approaches the light cone Ioffe time distribution. This is illustrated in Figure 26.

Moving off forward, a similar exercise can be repeated for the GPDs. The presence of an additional vector Δ introduces, in coordinate space, the dependence on another Lorentz scalar $\Delta \cdot z$. For zero skewness, this quantity is zero for GPDs on the lightcone. For pseudo GPDs, however, this is no longer true. Hence, in addition to z^2, in the case of PDFs, which captures the "off the light-coneness" of pseudo PDFs, in the case of GPDs, one also sees the dependence on $\Delta \cdot z$ for pseudo GPDs at zero skewness. Model calculations of pseudo GPDs at zero skewness reveal that the dependence on $\Delta \cdot z$ is more pronounced at larger t.

III.4.4. Evaluation of GPDs from their Mellin Moments and Ioffe Time Behavior

Complementary to the effort of calculating non-local operators on the lattice is the evaluation of Mellin moments of PDFs. While having their own set of complications in the evaluation of higher moments, they provide valuable input for a completely independent way
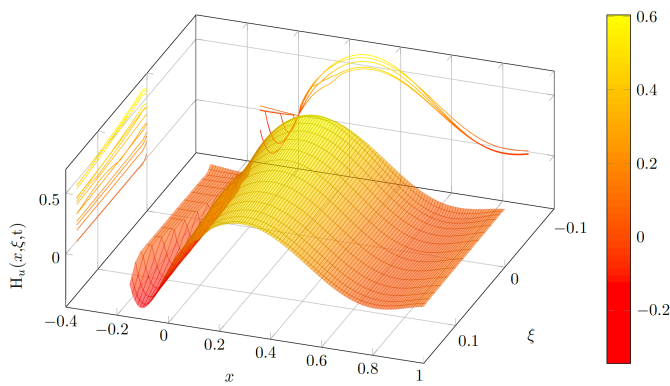
FIG. 27 The GPD H for the u quark at $t = -0.1 GeV^2$ reconstructed using the Generalized Form Factors calculated on the lattice.

of obtaining the PDFs. In the target rest frame, Ioffe time $\nu \equiv P \cdot z$ quantifies the distance along the light-cone that the quark fields describing the PDF are separated by. In this sense, it is a natural candidate for separating the short distance from the long distance physics. Using the Mellin moments, one can map out the Ioffe time behavior of the PDF for smaller values of Ioffe time. Having more moments allows one to describe the Ioffe time behavior of the PDF for higher and higher values of ν. The large Ioffe time behavior, on the other hand, is described by a term of the form $\nu^{-\alpha}$ which essentially captures the small x physics.

In the case of GPDs, polynomiality governs the behavior of the Mellin moments for non-zero skewness. The calculation of Generalized Form Factors on the lattice allows one to reconstruct the GPD in Ioffe time space for a given skewness similar to the case of PDFs as described above. By varying ξ, one obtains the x and ξ dependence of the GPD for a given t. In Fig. 27 we show the GPD H for the u quark evaluated by Fourier transformation from coordinate space. The Ioffe time dependence of the GPD was evaluated using the first three Mellin moments calculations from the lattice (see Section III.3), and assuming Regge behavior for the asymptotic z^- dependence.

III.5. Machine Learning for GPDs

Deeply virtual exclusive processes are measured in coincidence experiments where all the particles in the final state are either directly or indirectly detected. Therefore, extracting GPDs from data involves a much larger number of variables than in inclusive deep inelastic scattering. Furthermore, each experiment can only add a small piece to the picture characterized by a specific polarization configuration. This makes our problem virtually impossible to solve with traditional
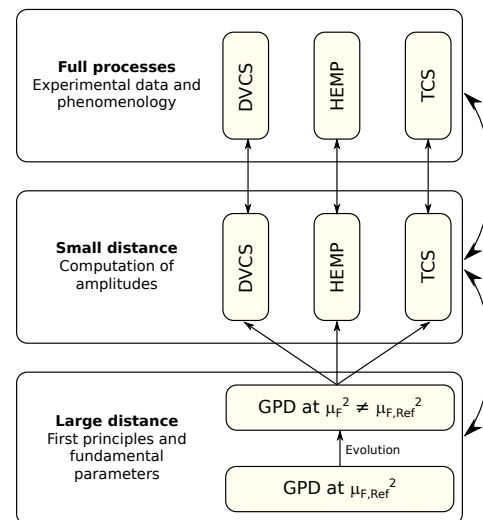

FIG. 28 The computation of an observable in terms of GPDs is generically layered in three basic steps: description of the hadron structure with nonperturbative quantities, computation of coefficient functions, and evaluation of cross sections.

methods: for high precision femtography which is required to obtain proton images, we need to develop more sophisticated analyses. Working towards this goal, recent efforts have focused on developing Machine Learning (ML) tools for the extraction of GPDs from data.

Three different groups have been attacking the problem.

III.5.1. The PARTONS framework

PARTONS (PARtonic Tomography of Nucleon Software) is a platform that handles multiple experimental channels where most of the tasks are automated, allowing the users to set physics assumptions at various point of the computation (Berthou *et al.*, 2018). This is achieved by splitting experimental channels into three pieces (see fig. 28), accordingly to the framework of collinear factorization. The large distance part contains the physics related to GPDs themselves. Various models (Goloskokov and Kroll, 2008; Mezrag *et al.*, 2013) are provided, together with leading-order evolution routines (Vinnikov, 2006). The second step consists in the computations of amplitudes from GPDs. Next-to-leading order computations of Compton Form Factors (CFFs) are also available. Finally, CFFs are connected to observables. PARTONS has been used in recent extractions of CFF from experimental data, using both functional parametrizations (Moutarde *et al.*, 2018) and Artificial Neural Networks (ANNs) (Moutarde *et al.*, 2019). This analysis focuses on the suppression of any model dependence, and on a careful estimation

of uncertainties. This was achieved by using separate neural networks for the real and imaginary parts of each CFF, and by avoiding any pre-factors driving the functional forms of CFFs. The replica method was used for the propagation of uncertainties, while the early-stopping regularisation method was utilised to provide the anticipated growth of uncertainties in the unconstrained kinematic domains. The networks were trained to nearly all available DVCS data with the genetic algorithm.

Work within the PARTONS framework has been also recently extended to estimate time-like Compton scattering (TCS) observables taking advantage of the complementarity between he Leading Order (LO) and Next to Leading Order (NLO) descriptions (Grocholski *et al.*, 2020); for a model free extraction of the subtraction constant entering the dispersion relations approach to GPDs (Diehl and Ivanov, 2007) and its impact on the energy momentum tensor matrix elements (Polyakov, 2003). It is also currently used to model light nuclei GPDs, and to develop a DVCS event generator for the future EIC. This software is free and open-source, released on GPLv3. The code and its documentation can be found on the PARTONS website[3].

III.5.2. Stepwise Regression Method

In a series of papers (Kumericki *et al.*, 2011; Kumerički, 2019a; Kumerički and Müller, 2016; Kumerički *et al.*, 2014), the authors propose to use the stepwise regression method in conjunction with an ANN analysis to address the question of which of the four leading order chiral-even CFFs, $\mathcal{H}$, $\mathcal{E}$, $\widetilde{\mathcal{H}}$, $\widetilde{\mathcal{E}}$ can be reliably extracted from exclusive photon electroproduction data. In stepwise regression, the number of real and imaginary components of the CFFs is gradually increased and all combinations are tried, until there is no statistically significant improvement in the description of the data. It was found (Kumerički, 2019a) that the DVCS data available so far are only sensitive to $\Im m\mathcal{H}$, $\Re e\mathcal{E}$ and $\Im m\widetilde{H}$. This method was used recently to extract the energy momentum tensor pressure form factor from DVCS data. A different conclusion from the one reported in (Burkert *et al.*, 2018) was found using the same set of experimental data (Kumerički, 2019b).

III.5.3. Femtography effort at Jefferson Lab

An ongoing effort at Jefferson Lab follows the footpath of a successful pilot project launched in the Summer 2019 where the physics community was asked

---

[3] http://partons.cea.fr

to address femtography within collaborative projects. These projects are now a reality: computer scientists, data scientists, mathematicians, visualization experts are collaborating to build a platform addressing the computational and theoretical challenges in mapping out the proton's 3D structure. The existent platform will allow us to refine our focus and to take further steps into providing both machine learning based and virtual reality shareable tools for the physics community.

III.6. Towards global fits for GPDs

The cleanest probe of GPDs is DVCS, which is measured in exclusive production of a hard photon in lepton-hadron scattering, $ep \rightarrow e'p'\gamma$. The virtual photon four-momentum squared, $Q^2 = -(k_e - k'_e)^2$, with k_e (k'_e) being the initial (final) electron four-momentum, provides a hard scale in the one photon exchange approximation. The presence of a hard scale allows us to single out the perturbative, short distance reaction from the non-perturbative, long distance matrix elements according to the factorization property of QCD (proofs of factorization for deeply virtual exclusive processes can be found in (Collins *et al.*, 1997; Ji and Osborne, 1998a,b)). Since the DVCS observable is not sensitive to flavor of the parton participating in the hard collision, probed proton GPD is written in terms of a sum of all quark flavor GPDs as,

$$H = \sum_q e_q^2 \, H_q \tag{42}$$

e_q being the quark charge. Gluon GPDs can also contribute to DVCS cross section at high orders. The neutron GPD can be obtained using isospin symmetry.

The exclusive hard photon can also be produced via the Bethe-Heitler (BH) scattering, where the photon is emitted from the electron. The BH process provides a means towards a cleaner extraction of the QCD matrix elements since these appear as linear combinations in the interference contribution to the cross section between the BH and DVCS scattering amplitudes, at variance with their bilinear counterparts in the pure DVCS contribution.

Experimental information on GPDs is also obtained from related channels, namely exclusive photon proton scattering, or timelike Compton scattering, exclusive Drell-Yan processes, and exclusive meson production. GPDs enter the cross section encoded in Compton Form Factors (CFFs) which, using QCD factorization, are defined as convolutions over the parton light cone momentum fraction x, of GPDs and QCD Wilson coefficient functions (Belitsky and Radyushkin, 2005; Diehl, 2003; Goeke *et al.*, 2001; Kumericki *et al.*, 2016).

At leading order one has, in the chiral-even sector,

$$\mathcal{F}_q(\xi,t) = \mathcal{C}\left(C^+ \, F_q\right) \equiv \int_{-1}^{1} dx \, C^+(x,\xi) F_q(x,\xi,t),$$
(43)

$$\widetilde{\mathcal{F}}(\xi,t) = \mathcal{C}\left(C^- \, \widetilde{F}_q\right) \equiv \int_{-1}^{1} dx C^-(x,\xi) \, \widetilde{F}_q(x,\xi,t)$$
.
(44)

where $\mathcal{F}_q = (\mathcal{H}_q, \, \mathcal{E}_q)$, and $\widetilde{\mathcal{F}}_q = (\widetilde{\mathcal{H}}_q \, \widetilde{\mathcal{E}}_q)$, respectively, with leading order coefficients functions given by,

$$C^{\pm}(x,\xi) = \frac{1}{x - \xi - i\epsilon} \mp \frac{1}{x + \xi - i\epsilon}.$$
(45)

GPDs observe crossing symmetry relations with respect to $x \rightarrow -x$, which allow us to introduce valence (symmetric) and quark singlet (anti-symmetric) distributions.

Traditional QCD global fits to extract GPDs from data are particularly challenging because of the complexity of the higher order Wilson coefficient functions (replacing $C^{\pm}$ in Eqs. (43) and (44)), and of the fact that the relative momentum fraction, x, of GPDs is not directly accessible from experiment but only indirectly relevant through the ξ-dependence of CFFs. In particular, it is very difficult to extract GPDs with an accurate flavor separation and determination of the scale dependence, with a similar accuracy level to what has been accomplished for PDFs. With the present kinematic coverage of experiments worldwide, at the best of our knowledge, it has not been possible to perform global fits of GPDs that span from the valence region measured in fixed target experiments, to the small-x which is accessible at high energy colliders. What makes such a global analysis very demanding is first of all, as mentioned above, that GPDs need to fulfill a set of properties derived from the symmetries of QCD, such as positivity and polynomiality. Fulfilling both at the same time has been a long issue for GPD phenomenologists. Recently, new modeling techniques have been introduced that might solve this longstanding issue (Chouika et al., 2017b), but have not been applied in practical fits. Another important difference with PDFs is that the CFFs from which GPDs are extracted, enter the cross section in bilinear forms. Therefore, GPDs corresponding to different polarization configurations all contribute to specific helicity states of the various observables: for example, in DVCS, the unpolarized structure function, $F_{UU,T}$ (Kriesten et al., 2020), contains both the vector, H, E, and axial-vector, $\widetilde{H}, \widetilde{E}$, GPDs (the other polarization configurations behave similarly). As a result, in order to extract information from experiment, many more observables need to be analyzed simultaneously. This is what motivated, for instance, the first attempts to global fits in (Kumerički, 2019b; Kumerički and Müller, 2016). To determine the various

observables that are necessary to extract GPDs from data, current experimental programs at Jefferson Lab, COMPASS at CERN and J-PARC are set to measure DVCS and the crossed channel reactions to DVCS, namely both TCS, $\gamma p \rightarrow p'\mu^+\mu^-$ (Berger et al., 2002b; Boër et al., 2015; Moutarde et al., 2013), and the exclusive Drell-Yan process, $\pi^{\pm}p \rightarrow p'\mu^+\mu^-$ (Sawada et al., 2016). On the other side, GPDs can also be extracted from deeply virtual meson production although this requires a clear understanding of the meson distribution amplitudes.

NLO corrections in α_S to CFFs and evolution of GPDs are also challenging in a global fit. Gluon GPDs are, in fact, expected to bring a significant contribution to both DVCS and TCS CFFs (Moutarde et al., 2013). In the perspective of the upcoming EIC, NLO studies will become more and more pressing. Furthermore, many available data present a virtuality Q^2 of few GeV^2, i.e. of the same order of magnitude as the square of the proton mass. Therefore, target mass corrections, but also finite t corrections (Braun et al., 2012) need to be taken into account. They could be responsible for half of the signal measured at some kinematical bins at JLab (Defurne et al., 2015), and may, therefore, be an essential piece to connect the lower Q^2 data (few GeV^2) with higher ones at the EIC.

The four additional GPDs appearing in the chiral-odd sector, $H_T, E_T, \widetilde{H}_T, \widetilde{E}_T$, can be measured in processes that allow for quark helicity flip at the amplitude level, for instance in π^o and η photoproduction (Ahmad et al., 2009; Goldstein et al., 2015; Goloskokov and Kroll, 2011) (π^o electroproduction also constitutes the main background process for DVCS). It should also be noticed that factorization has not been proven for transversely polarized virtual photon exchange which dominates the process in this case, and that the quark flip process involves a beyond leading-twist pion lightfront wave function. Exclusive π^0 production data seem to indicate that standard colinear factorization might not be working at JLab kinematics (Defurne et al., 2016). A similar situation has been found for the Q^2 dependence of recent DVCS data (Georges, 2018). Future experiments will help clarifying the issue of the scale dependence in both processes.

Chiral-odd gluon GPDs, contribute to DVCS at NLO, generating a $\cos 2\phi$ modulation in the cross section. Although a hint of this modulations is consistent with the data in Ref.(Defurne et al., 2017), the experimental precision remains too low to disentangle it from possible higher-twist contributions.

In summary, at a time when the US EIC project is getting off the ground, GPD phenomenologists are facing many challenges, both theoretical and in setting up an appropriate computational framework. The solutions that will be brought forward to the various issues mentioned in this report will certainly impact our

understanding of the future EIC measurements, but first and foremost they will be key to interpreting the data that are already being taken at fixed target facilities. A better control of the cross section structure for DVCS and its crossed channels, TCS and exclusive Drell Yan, of higher-twist terms and their factorization, of kinematic and target mass corrections and NLO evolution, will allow for significant steps towards mapping out the 3D structure of the nucleon.

IV. TRANSVERSE MOMENTUM DEPENDENT PDFS (TMD PDFS)

IV.1. Introduction to TMD PDFs

The TMD PDF concept, in the most basic sense, directly extends the ordinary PDF concept to incorporate dependence on the parton's transverse momentum. That is, instead of having a number density $f(x)$ of partons per unit of lightcone momentum fraction x, one has a density $f(x, \mathbf{k}_T)$ of partons per unit of both the momentum fraction x *and* the (small) transverse momentum components. A similar relation exists between standard fragmentation functions and TMD fragmentation functions. Standard factorization theorems involve collinear PDFs (and fragmentation functions) only, whereas situations that use TMD PDFs require a different kind of "TMD" factorization theorem (Collins *et al.*, 1985).

Collinear factorization relies on processes being rather inclusive, such that the details of small variations in parton transverse momentum are not important. Transverse-momentum–dependent PDFs (TMD PDFs), by contrast, arise in less inclusive processes, particularly where low, and especially nonperturbative, transverse momentum transfer is important. There are a number of processes where a complete QCD treatment calls for the TMD PDF concept. These include especially cross sections differential in a measured transverse momentum — so-called multiscale processes, where there is an overall physical hard scale (usually labeled Q) and a transverse momentum which may also be hard in some regions but is typically very different from Q. Drell-Yan scattering is a classic example of this. There, the overall hard scale is set by the invariant energy Q of the produced dilepton pair, while the total transverse momentum of the pair $\mathbf{q_T}$ provides the transverse momentum dependence. For a cross section integrated over $\mathbf{q_T}$, collinear factorization is relevant, whereas cross sections differential in $\mathbf{q_T}$ require a form of TMD factorization, especially in the region $q_T \ll Q$ (we denote $|\mathbf{q_T}| \equiv q_T$ here and in the following). More on this example follows below. The information about transverse degrees of freedom is essential in many non-inclusive collider observables (Angeles-Martinez *et al.*, 2015). The sensitivity to a nonperturbative intrinsic transverse momentum is especially exciting from the perspective of hadron structure also because the intrinsic transverse momentum may couple in nontrivial ways with spin degrees of freedom. Early classic work on TMD structures (Mulders and Tangerman, 1996) enumerated the large number of TMD PDF structures that can arise once a transverse momentum degree of freedom is allowed for the parton.

The TMD PDF concept also arises in many other areas of QCD physics. Another approach to determine the transverse momentum dependence, valid at low x, can be developed within the color-glass condensate (Gelis *et al.*, 2010) framework, an effective model formulated within QCD. A special limit, so-called improved transverse-momentum–dependent (Altinoluk *et al.*, 2019; Kotko *et al.*, 2015) factorization, addresses the situation where one of the colliding hadrons is dilute and is characterized by collinear PDFs, and the other one (the target) is dense and is parametrized by a set of gluon densities dependent on longitudinal and transverse momentum. The processes where this factorization applies are limited to forward production. There is also a Monte Carlo approach to obtain TMD distributions called Parton Branching TMD(Bermudez Martinez *et al.*, 2019; Hautmann *et al.*, 2018). It is essentially based on DGLAP dynamics.

In this section, we elaborate on the TMD PDF concept, giving a brief introduction to situations where TMD PDFs appear instead of collinear PDFs, leaving technical details of their definition to Sec. IV.2.

It is instructive to contrast TMD PDFs with the collinear PDFs studied in Sec. II, and so we consider the specific case of the Drell-Yan process, the production of a lepton pair with momentum q^μ through the process $pp \to Z/\gamma* \to \ell^+\ell^-$ at a hadron collider, while noting that a similar situation also arises in semi-inclusive DIS and electron-positron annihilation such as will be studied at a future EIC (Accardi *et al.*, 2016b).

First, consider the case that one is only interested in measuring the invariant mass $Q = \sqrt{q^2}$ of the lepton pair, but not its transverse momentum $\mathbf{q_T}$. This is described by collinear factorization, which allows one to factorize the cross section as

$$\frac{d\sigma}{dQ^2} = \sum_{i,j} \int_0^1 d\xi_a d\xi_b \, f_{i/P_a}(\xi_a) f_{j/P_b}(\xi_b) \frac{d\hat{\sigma}_{ij}(\xi_a, \xi_b)}{dQ^2}$$
$$\times \left[1 + \mathcal{O}\left(\frac{\Lambda_{\text{QCD}}}{Q} \right) \right] . \qquad (46)$$

Here, $f_{i/P}(\xi)$ is the PDF for a parton of type i carrying the fraction ξ of the momentum of its parent hadron P, we sum over all possible flavors i and j, and $\hat{\sigma}_{ij}$ is the partonic cross section for the Drell-Yan process. In an observable like (46), that has been averaged over all allowed transverse momenta $\mathbf{q_T}$ of the lepton pair, it is reasonable to assume that the intrinsic transverse motion of partons in the proton is numerically not relevant, and thus the PDFs in (46) are functions of longitudinal momentum components only. Note that (46) receives corrections in Λ_{QCD}/Q, which are typically negligible at high-energy experiments, but may become important at low-energy colliders.

The aim of TMD factorization is to generalize Eq. (46) to also measure the transverse momentum $\mathbf{q_T}$ of the produced lepton pair. For very large $\mathbf{q_T}$, it is again reasonable to assume that the intrinsic motion of partons

inside the hadrons is small, and collinear factorization applies:

$$q_T \sim Q \gg \Lambda_{\rm QCD} : \tag{47}$$

$$\frac{d\sigma}{dQ^2 d^2\mathbf{q_T}} = \sum_{i,j} \int_0^1 d\xi_a d\xi_b \, f_{i/P_a}(\xi_a) f_{j/P_b}(\xi_b) \frac{d\hat{\sigma}_{ij}(\xi_a,\xi_b)}{dQ^2 d^2\mathbf{q_T}}$$

$$\times \left[1 + \mathcal{O}\left(\frac{\Lambda_{\rm QCD}}{Q}, \frac{\Lambda_{\rm QCD}}{q_T} \right) \right].$$

In this case, $\mathbf{q_T}$ is dominantly generated by the hard partonic process $\hat{\sigma}_{ij}$, which is perturbatively calculable, while the only nonperturbative input to (47) is through the standard PDFs. Compared to (46), (47) also receives corrections in $\Lambda_{\rm QCD}/q_T$, signaling that it breaks down for small q_T. Indeed, the situation becomes drastically different if one considers transverse momenta much smaller than the invariant mass of the lepton pair, $q_T \ll Q$. This is the realm of *TMD factorization*, where one has

$$q_T \ll Q : \tag{48}$$

$$\frac{d\sigma}{dQ^2 d^2\mathbf{q_T}} = \sum_{i,j} H_{ij}(Q) \int_0^1 d\xi_a d\xi_b \int d^2\mathbf{b_T} \, e^{i\mathbf{b_T}\cdot\mathbf{q_T}}$$

$$\times f_{i/P}(\xi_a,\mathbf{b_T}) f_{j/P}(\xi_b,\mathbf{b_T})$$

$$\times \left[1 + \mathcal{O}\left(\frac{\Lambda_{\rm QCD}}{Q}, \frac{q_T}{Q} \right) \right].$$

Here, the hard factor $H_{ij}(Q)$ describes the underlying partonic process $q_i q_j \rightarrow Z/\gamma^* \rightarrow \ell^+\ell^-$, and the $f_{i/P}(\xi,\mathbf{b_T})$ are TMD PDFs in Fourier space, describing the probability to find a parton of type i with a longitudinal momentum fraction ξ and transverse momentum conjugate to[4] $\mathbf{b_T}$. Upon taking the inverse Fourier transform in (48), one then recovers the $\mathbf{q_T}$ distribution of the lepton pair. (48) is valid both in the nonperturbative regime, where $q_T \sim \Lambda_{\rm QCD} \ll Q$ and the TMD PDFs are intrinsically nonperturbative objects, and in the perturbative regime where $\Lambda_{\rm QCD} \ll q_T \ll Q$ and the TMD PDFs can be perturbatively calculated. It also receives corrections in q_T/Q, which in the literature are often included as the so-called Y term. These corrections are important to smoothly transition between the regimes described by (47) and (48).

---

[4] The unfortunate overlapping use of the notation $\mathbf{b_T}$ for two distinct objects in the TMD PDF and GPD literatures should be noted. In the GPD literature, $\mathbf{b_T}$ denotes the impact parameter of the struck quark with respect to the center of momentum of the hadron; it is Fourier conjugate to the momentum transfer Δ_T. In the TMD PDF literature, $\mathbf{b_T}$ denotes the Fourier conjugate to the transverse momentum $\mathbf{k_T}$ of the struck quark, corresponding to a *relative* separation in the relevant quark bilinear operator, cf. the definition (51) below. Put succinctly, the relation between the conventions in the two literatures is akin to the relation between center-of-mass and relative coordinates. In the present section, the impact parameter will instead be denoted by $\mathbf{r_T}$, cf. the discussion at the end of section IV.3.

IV.2. Definitions of TMD PDFs

Setting up consistent definitions for TMD PDFs, useful beyond the most basic parton model approaches, involves a significant number of subtleties beyond what are encountered directly in the more standard collinear factorization. The history of these efforts is long (Collins, 2003) and we will not be able to cover all aspects here. See, however, reviews in (Diehl, 2016; Rogers, 2016) for somewhat broader summaries that highlight some of the more subtle aspects.

In this section, we provide more details on the definition of TMD PDFs.

Classification of TMD PDFs. First, we note that TMD PDFs can be classified according to the scheme used for the hard factor H_{ij} in (48). In the original formulation by Collins, Soper and Sterman, often referred to as CSS1, one has $H_{ij} = 1$ such that the hard factor is effectively absorbed into the TMD PDFs (Collins *et al.*, 1985). In its revised formulation (CSS2) due to Collins (Collins, 2011), see also (Aybat and Rogers, 2011), H_{ij} is defined as the form factor of the Drell-Yan process in the $\overline{\rm MS}$ scheme. This scheme choice is also adopted by formulations of TMD factorization employing soft-collinear effective theory (SCET) (Becher and Neubert, 2011; Chiu *et al.*, 2012; Echevarría *et al.*, 2013; Li *et al.*, 2016). Lastly, TMD PDFs as introduced by Ji, Ma and Yuan (JMY) (Ji *et al.*, 2005) employ a scheme where H_{ij} depends not only on the $\overline{\rm MS}$-renormalization scale μ, but also on an additional parameter ρ related to the regulation of rapidity divergences, which we discuss below. All of these formulations are perturbatively related to each other, and explicit relations are given in (Collins and Rogers, 2017; Prokudin *et al.*, 2015).

Definitions of TMD PDFs. Consider a hadron p with momentum $P^\mu = (\sqrt{M^2 + P_z^2}, 0, 0, P^z)$. It is useful to introduce a basis of lightlike vectors

$$n^\mu = \frac{1}{\sqrt{2}}(1,0,0,1), \quad \bar{n}^\mu = \frac{1}{\sqrt{2}}(1,0,0,-1), \tag{49}$$

such that p is moving close to the n direction. The TMD PDF can then be defined as

$$f_{i/P}(x,\mathbf{b_T},\mu,\zeta) = \lim_{\substack{\epsilon\to 0 \\ \tau\to 0}} Z_{\rm uv}^i(\mu,\zeta,\epsilon) \frac{f_{i/P}^{0\,(u)}(x,\mathbf{b_T},\epsilon,\tau,xP^+)}{S_{n\bar{n}}^{0\,{\rm sub}}(\mathbf{b_T},\epsilon,\tau)}$$

$$\times \sqrt{S_{n\bar{n}}^0(\mathbf{b_T},\epsilon,\tau)}. \tag{50}$$

Here, i denotes the parton flavor, x is its longitudinal momentum fraction, $\mathbf{b_T}$ is Fourier-conjugate to the transverse momentum of the struck quark, μ denotes the $\overline{\rm MS}$-renormalization, and ζ is the so-called Collins-Soper scale (Collins and Soper, 1982). On the right-hand side, ϵ is the UV regularization parameter, and UV divergences in $1/\epsilon$ are absorbed by the $\overline{\rm MS}$-counterterm $Z_{\rm uv}^i$. $f_{i/P}^{0\,(u)}$

is the bare unsubtracted TMD PDF, $S^0_{n\bar{n}}$ is the bare soft function, and the factor $S^{0\,\mathrm{sub}}$ removes overlap between $f^{0\,(u)}_{i/P}$ and $S^0_{n\bar{n}}$.[5] All these functions are plagued by additional so-called rapidity divergences (Becher and Neubert, 2011; Chiu *et al.*, 2012; Collins, 2008; Collins and Soper, 1981; Collins and Tkachov, 1992; Echevarria *et al.*, 2012), which are regulated by τ. There are many different rapidity regulators τ employed in the literature, leading to different results for the individual ingredients on the right-hand side of (50), but the final TMD PDF is well-defined and unique up to choice of scheme for H_{ij} as discussed above.

The unsubtracted TMD PDF $f^{0\,(u)}_{i/P}$ is defined as a hadron matrix element, and as such is sensitive to both x and $\mathbf{b_T}$, while the soft factor $S^0_{n\bar{n}}$ is a vacuum matrix element only sensitive to $\mathbf{b_T}$. Their definitions read

$$f^{0\,(u)}_{i/P}(x,\mathbf{b_T},\epsilon,\tau,xP^+) = \int \frac{db^-}{2\pi} e^{-ib^-(xP^+)}\Big\langle p(P)\Big|\Big[\bar{q}(b^\mu)W_{\bar{n}}(b^\mu;-\infty,0)\frac{\gamma^+}{2}W^\dagger_{n_\perp}(-\infty\bar{n},\mathbf{b_T},0)W^\dagger_{\bar{n}}(0;-\infty,0)q(0)\Big]_\tau\Big|p(P)\Big\rangle,$$

$$S^0_{n\bar{n}}(\mathbf{b_T},\epsilon,\tau) = \frac{1}{N_c}\Big\langle 0\Big|\mathrm{Tr}\big[W^\dagger_n(\mathbf{b_T};-\infty,0)W_{\bar{n}}(\mathbf{b_T};-\infty,0)W^\dagger_{n_\perp}(-\infty\bar{n};\mathbf{b_T},0)$$
$$\times W^\dagger_{\bar{n}}(0;-\infty,0)W_n(0;-\infty,0)W_{n_\perp}(-\infty n;\mathbf{b_T},0)\big]_\tau\Big|0\Big\rangle. \tag{51}$$

with Tr denoting the color trace. Here, $b^\mu = b^-\bar{n}^\mu + b^\mu_T$, lightcone coordinates are defined as $x^\pm = (x^0 \pm x^3)/\sqrt{2}$, and the W_n are path-ordered Wilson lines defined as

$$W_n(x;a,b) = P\exp\left[-ig_s\int_a^b ds\, n\cdot A(x^\mu + sn^\mu)\right]. \tag{52}$$

The paths of the Wilson lines in (51) are illustrated in Fig. 29. They form a closed path between the quark fields in the TMD PDF and a closed loop in the soft function, thereby rendering these functions gauge invariant.

In (51), the regulator τ is not specified, but is typically implemented to modify the Wilson line structure. The regulator most closely connected to the lattice studies presented in section IV.3 is that of Collins, which is implemented by taking the lightlike reference vectors n and $\bar{n}$ off the lightcone as (Collins, 2011)

$$n^\mu \quad\rightarrow\quad n^\mu_{y_A} \equiv n^\mu - e^{-2y_A}\bar{n}^\mu,$$
$$\bar{n}^\mu \quad\rightarrow\quad \bar{n}^\mu_{y_B} \equiv \bar{n}^\mu - e^{+2y_B}n^\mu. \tag{53}$$

The regulator is removed through the limit $y_A \rightarrow \infty$, $y_B \rightarrow -\infty$. Concretely, in this regulator scheme the TMD PDF is obtained as

$$f_{i/P}(x,\mathbf{b_T},\mu,\zeta) = \lim_{y_B\rightarrow-\infty} Z_{\mathrm{uv}}\frac{f^{0\,(u)}_{i/P}(x,\mathbf{b_T},\epsilon,y_B,xP^+)}{\sqrt{S^0_{n_{y_n}\bar{n}_{y_B}}(\mathbf{b_T},\epsilon)}}. \tag{54}$$

Here, y_n is a free parameter appearing only in the Wilson lines of the soft function, and the Collins-Soper (CS) scale

is defined as $\zeta = (xP^+e^{-y_n})^2$. In the TMD PDF for a proton moving along the $\bar{n}$ direction, the roles of y_A and y_B will be reversed.

Evolution equations. The TMD PDF defined in the $\overline{\mathrm{MS}}$-scheme depends on two scales, namely the $\overline{\mathrm{MS}}$-renormalization scale μ and the Collins-Soper scale ζ. The all-order form of its evolution is given by

$$\frac{d\ln f_{i/P}(x,\mathbf{b_T},\mu,\zeta)}{d\ln\mu} = \gamma^i_\mu(\mu,\zeta)$$
$$= \Gamma^i_{\mathrm{cusp}}[\alpha_s(\mu)]\ln\frac{\mu^2}{\zeta} + \gamma^i_\mu[\alpha_s(\mu)], \tag{55}$$
$$\frac{d\ln f_{i/P}(x,\mathbf{b_T},\mu,\zeta)}{d\ln\zeta} = \frac{1}{2}\gamma^i_\zeta(\mu,b_T)$$
$$= -2\int_{1/b_T}^\mu \frac{d\mu'}{\mu'}\Gamma^i_{\mathrm{cusp}}[\alpha_s(\mu')] + \gamma^i_\zeta[\alpha_s(1/b_T)]. \tag{56}$$

Here, Γ^i_{cusp} is the so-called cusp anomalous dimension, and the $\gamma^i[\alpha_s]$ denote the non-cusp anomalous dimensions. Note, however, that the CS kernel γ_ζ, which in the literature is also often referred to as K, becomes nonperturbative when $q_T \sim b_T^{-1} \sim \Lambda_{\mathrm{QCD}}$, independent of the choice of μ. In perturbation theory, γ_ζ is known at three loops (Li and Zhu, 2017; Vladimirov, 2017).

A solution to Eqs. (55) and (56) is given by

$$f_{i/P}(x,\mathbf{b_T},\mu,\zeta) = f_{i/P}(x,\mathbf{b_T},\mu_0,\zeta_0) \tag{57}$$
$$\times \exp\left[\int_{\mu_0}^\mu \frac{d\mu'}{\mu'}\gamma^i_\mu(\mu',\zeta_0)\right]\exp\left[\frac{1}{2}\gamma^i_\zeta(\mu,b_T)\ln\frac{\zeta}{\zeta_0}\right].$$

Note that the Collins-Soper evolution in ζ governs the energy dependence of the TMD PDF, as $\zeta \propto (xP^+)^2$ corresponds to the momentum of the struck quark. Thus, since γ_ζ itself becomes nonperturbative, TMD PDFs at different energies are related through a nonperturbative

---

[5] In the SCET-based literature, the combination $f^{0\,(u)}_{i/P}/S^{0\,\mathrm{sub}}_{n\bar{n}}$ is often referred to as the beam function.
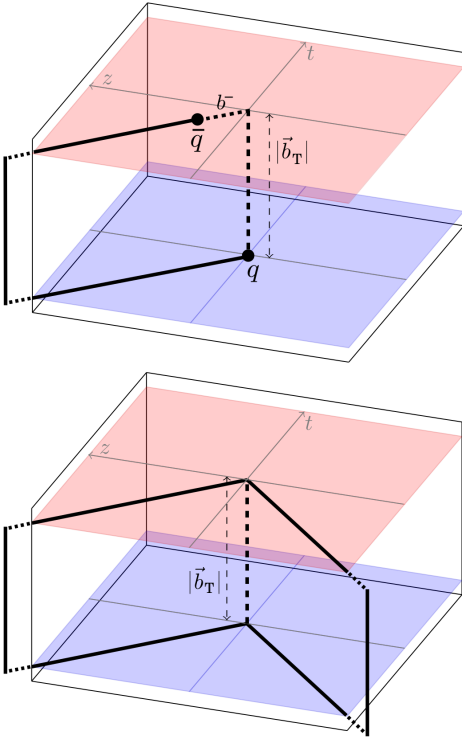
FIG. 29 Illustration of the Wilson-line structures of the unsubtracted TMD PDF (top) and soft function (bottom), as defined in Eq. (51). Figure taken from (Ebert *et al.*, 2019b), with slight adjustment of the b-component labeling to match the notation used in the present work.

evolution, and hence calculating γ_ζ from lattice QCD is of major interest to TMD physics.

Spin-dependent TMD PDFs. For simplicity, we have so far restricted ourselves to unpolarized processes. However, due to the vector nature of $\mathbf{q_T}$, or equivalently $\mathbf{b_T}$, TMD PDFs are sensitive to both the polarization of the hadron and the spin of the struck parton. This is especially useful and can be exploited when nucleon or hadron structure is the target topic of interest.

In the language and notation of Mulders, Tangerman, and collaborators (Bomhof and Mulders, 2008; Mulders and Tangerman, 1996; Tangerman and Mulders, 1995), the leading TMD PDFs arise through the following decomposition,

$$
\Phi(x, \mathbf{k}_T, P, S) = \frac{1}{2} \left\{ f_1(x, k_T^2)\slashed{P} + \frac{1}{2}h_{1T}(x, k_T^2)\gamma_5 [\slashed{S}_T, \slashed{P}] \right.
$$

$$
+ S_L g_{1L}(x, k_T^2)\gamma_5\slashed{P} + \frac{\mathbf{k}_T \cdot \mathbf{S}_T}{M} g_{1T}(x, k_T^2)\gamma_5\slashed{P}
$$

$$
+ S_L h_{1L}^\perp(x, k_T^2)\gamma_5\frac{[\slashed{k}_T, \slashed{P}]}{2M} + \frac{\mathbf{k}_T \cdot \mathbf{S}_T}{M} h_{1T}^\perp(x, k_T^2)\gamma_5\frac{[\slashed{k}_T, \slashed{P}]}{2M}
$$

$$
+ i h_1^\perp(x, k_T^2)\frac{[\slashed{k}_T, \slashed{P}]}{2M} - \frac{\epsilon_T^{k_T S_T}}{M} f_{1T}^\perp(x, k_T^2)\slashed{P} \right\}, \tag{58}
$$

where Φ is, up to normalization conventions, the momentum space version of the unsubtracted TMD

PDF definition on the first line of Eq. (51), but with a general Dirac structure rather than the trace over Γ. Equation (58) displays the eight different TMD PDF functions that parametrize the range of possible combinations of correlations between parton polarization, hadron polarization, and transverse momentum. Their contribution to, for example, the SIDIS cross section can be seen directly in (Bacchetta *et al.*, 2007). By contrast, only three correlation functions survive the reduction to the collinear factorization case.

Several of the polarization-dependent TMD correlation functions have attracted particular attention for having novel properties unique to QCD with TMD factorization. For example, the Sivers function $f_{1T}^\perp(x, k_T^2)$ vanishes in naive definitions of the TMD PDF by PT invariance (Collins, 1993). A nonzero contribution is only made possible by the nontrivial Wilson line in Fig. 29 (Brodsky *et al.*, 2002). The Wilson line introduces a pattern of non-universality in the form of a sign change of the Sivers TMD function between Drell-Yan-like processes and SIDIS-like processes (Collins, 2002).

Large Transverse Momentum. The TMD factorization treatment discussed above is derived for the limit that parton transverse momentum is much smaller than the overall hard scale of the problem. Approximations made in this limit are no longer valid when q_T becomes of order or larger than the hard scale Q. There, a purely fixed-order collinear perturbative treatment that takes into account nonfactorizable transverse momentum behavior is the appropriate approach. Understanding the transition between these two different types of transverse-momentum dependence is important for understanding the TMD PDFs in particular, especially at moderate Q, where there is higher sensitivity to nonperturbative transverse momentum but a less-clear demarcation between large and small transverse momentum.

Schematically, the contributions from small and large transverse momentum are combined in the following additive way:

$$
\frac{d\sigma}{dQ^2 d^2\mathbf{q_T}} = W + Y, \tag{59}
$$

where the "W-term" is the factorization formula involving TMD PDFs, Eq. (48), while the second "Y-term" is the correction for large transverse momentum, perturbatively calculable using collinear factorization techniques. Achieving a robust matching between the two regions is critical for establishing that each region is under theoretical control. A current challenge is that calculations done with existing collinear parton distribution and fragmentation functions produce significant tension with data in the Y-term region of transverse momentum (Bacchetta *et al.*, 2019b; Gonzalez-Hernandez *et al.*, 2018; Moffat *et al.*, 2019;

Wang *et al.*, 2019a). Work is needed to understand and resolve this tension.

One consequence of the large transverse momentum contribution is that the relationship between the TMD and collinear versions of factorization is not a simple integration over transverse momentum. That is, from Eq. (59),

$$\int d^2\mathbf{q_T} \frac{d\sigma}{dQ^2 d^2\mathbf{q_T}} \neq \int d^2\mathbf{q_T}\, W\,. \qquad (60)$$

Ultra-violet divergences in the transverse momentum integrals of TMD functions are one symptom of the absence of a Y term in the treatment. The sensitivity to the ultraviolet transverse momentum can be nontrivial (Qiu *et al.*, 2020). More work in the direction of quantifying and understanding these ultraviolet effects is needed.

When the large transverse momentum q_T becomes even larger than Q, both observed momentum scales are in the perturbative regime. In the case of the Drell-Yan process, since the transverse momentum of the colliding partons is sufficiently smaller than both Q and q_T, the Drell-Yan cross section can be factorized in terms of PDFs convoluted with a perturbatively calculable short-distance hard part. However, due to the large difference of the two observed momentum scales, $q_T \gg Q$, the large logarithms $\log(q_T/Q)$ of the short-distance hard part need to be resummed, and can be systematically subsumed into an effective fragmentation function for a parton to fragment into a Drell-Yan lepton pair (Berger *et al.*, 2002a; Fai *et al.*, 2003).

IV.3. TMD observables from lattice QCD

An ongoing program of evaluating transverse-momentum–dependent observables in hadrons within lattice QCD has been reported in Refs. (Engelhardt, 2017; Engelhardt *et al.*, 2018, 2016; Hagler *et al.*, 2009; Musch *et al.*, 2012, 2011; Yoon *et al.*, 2017). These studies are based on calculating hadron matrix elements of the type

$$\widetilde{\Phi}^{[\Gamma]} \equiv \frac{1}{2}\langle P', S'|\bar{q}(-b/2)\Gamma\,\mathcal{U}[-b/2,b/2]q(b/2)|P,S\rangle\;; \qquad (61)$$

$\widetilde{\Phi}$ is a version of the unsubtracted TMD PDF defined in the first line of (51) cast purely in terms of spacetime separations, i.e., even the dependence on momentum fraction x has been replaced by a dependence on the Fourier-conjugate longitudinal separation b^- (cf. also the complementary definition (58), which instead is cast purely in momentum space). Several generalizations and adjustments are made to arrive at a formulation suitable for lattice calculations. An arbitrary Dirac structure Γ is allowed for, and the states can also carry

definite spin in addition to momentum. Also off-forward matrix elements, $P' \neq P$, are of interest, as will be detailed further below. In a concrete lattice calculation, the staple-shaped gauge connection between the quark operators $\bar{q}$, q, summarized here by $\mathcal{U}$, has finite extent; in the following, the vector v specifies the direction of the staple legs, with their length scaled by the parameter η. For $\eta = 0$, the path becomes a straight link between the quark operators. Standard TMD observables are obtained by extrapolating the obtained data to $\eta \to \infty$.

As discussed further above, unsubstracted matrix elements of the type (61) contain divergences, which have to be absorbed into corresponding multiplicative soft factors. The TMD observables considered in the following are, however, appropriate ratios in which the soft factors cancel. As a result, the soft factors do not need to be specified in detail for present purposes. To regulate rapidity divergences, the staple direction v is taken off the lightcone into the spacelike domain (Collins, 2011). This scheme is particularly suited for the connection to lattice QCD, as will become clear presently. A useful parameter characterizing how close v is to the lightcone is the Collins-Soper type parameter $\hat{\zeta} = v \cdot P/(|v||P|)$, in terms of which the lightcone is approached for $\hat{\zeta} \to \infty$.

The application of standard lattice QCD methods to evaluate (61) requires the operator in (61) to exist at a single time; given that b and v are spacelike (the latter by virtue of the rapidity regulator scheme), there is no obstacle to boosting the problem to a Lorentz frame in which this is the case. The transformation of the results back to the original frame is facilitated by a decomposition of (61) into Lorentz invariants that parallels the decomposition (58) of the momentum space correlator into TMD PDFs. For example, in the $\Gamma = \gamma^+$ channel, for a proton (Musch *et al.*, 2012),

$$\frac{1}{2P^+}\widetilde{\Phi}^{[\gamma^+]} = \widetilde{A}_{2B} + im_N\epsilon_{ij}b_i S_j\widetilde{A}_{12B} \qquad (62)$$

The invariants $\widetilde{A}_{iB}$ essentially correspond to Fourier-transformed TMD PDFs. Through them, one can finally define observables such as the generalized Sivers shift (Musch *et al.*, 2012),

$$\langle k_T\rangle_{TU}(b^2, b \cdot P, \hat{\zeta}, \eta v \cdot P, \ldots) =$$
$$- m_N \frac{\widetilde{A}_{12B}(b^2, b \cdot P, \hat{\zeta}, \eta v \cdot P, \ldots)}{\widetilde{A}_{2B}(b^2, b \cdot P, \hat{\zeta}, \eta v \cdot P, \ldots)}\,. \qquad (63)$$

In the $b_T \to 0$ limit, (63) formally represents the average transverse momentum k_T of unpolarized ("U") quarks orthogonal to the transverse ("T") spin of the proton, normalized to the corresponding number of valence quarks. Note that any multiplicative soft factors renormalizing the $\widetilde{A}_{iB}$ are canceled by forming this type of ratio.
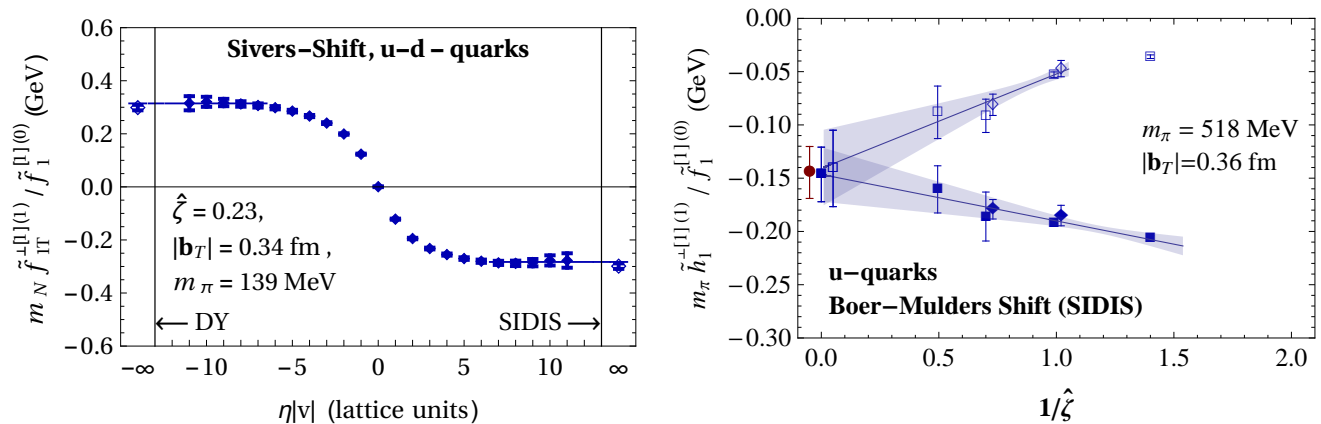
FIG. 30 Left: Proton Sivers shift as a function of staple length for fixed b_T and $\hat{\zeta}$; $\eta \to \infty$ defines the SIDIS limit. Right: Extrapolation of the SIDIS-limit data for the pion Boer-Mulders shift to large $\hat{\zeta}$ at fixed b_T (Engelhardt *et al.*, 2016). Open symbols represent a partial contribution that dominates at large $\hat{\zeta}$, providing further insight into the approach to the asymptotic regime.

Lattice calculations to date have predominantly focused on the special case $b \cdot P = 0$, corresponding to evaluating integrals of the TMD PDFs in question over the longitudinal quark momentum fraction x, and thus concentrating purely on the transverse-momentum dependence. Some example results are exhibited below. Generalizing these calculations to a scan of the $(b \cdot P)$-dependence allows one to access also the dependence on x, which is Fourier conjugate to $b \cdot P$. Note that, since soft factors do not depend on $b \cdot P$, they can be factored outside the corresponding Fourier transforms and still canceled in ratios. Cast in Lorentz-invariant form, the lattice geometries relevant for TMD observables must obey the relation (Musch *et al.*, 2012)

$$\frac{v \cdot b}{v \cdot P} = \frac{b \cdot P}{m_N^2} \left(1 - \sqrt{1 + 1/\hat{\zeta}^2} \right) , \qquad (64)$$

which forces one to use general off-axis directions on the lattice, significantly complicating the analysis. Data from a preliminary scan of the $(b \cdot P)$-dependence indicate that it is feasible to obtain also the x-dependence of TMD ratios such as (63). A corresponding comprehensive data production effort is currently in progress. A complementary approach to the x-dependence of TMD PDFs based on quasi-TMD PDFs is presented in detail in the next section.

In a concrete lattice calculation, one must extrapolate the data to the $\eta \to \infty$ limit in order to make contact with standard TMD PDFs. This extrapolation is typically under good control, as shown in Fig. 30 (left), exhibiting first data recently obtained directly at the physical pion mass. Moreover, the lattice data need to be extrapolated to the regime of large $\hat{\zeta}$. This presents a considerable challenge, since it requires data at sufficiently high hadron momenta. Figure 30 (right) displays results of a corresponding dedicated study of

the Boer-Mulders shift in a pion (Engelhardt *et al.*, 2016); the Boer-Mulders shift is a counterpart to the Sivers shift in which the hadron is unpolarized, but the quark is transversely polarized. A further question to be faced is whether the multiplicative renormalization pattern of continuum TMD PDFs carries over to the lattice formulation. This issue was explored in Ref. (Yoon *et al.*, 2017) by varying the discretization scheme and testing for violations of a multiplicative renormalization pattern; a sample comparison is shown in Fig. 32 (left), corroborating that soft factors cancel in the Sivers shift ratio to the accuracy accessible in the calculation. Note that, for selected Dirac structures and discretization schemes, operator mixing has been shown to occur for quark bilinear operators with staple-shaped gauge connections (Constantinou *et al.*, 2019; Green *et al.*, 2020; Shanahan *et al.*, 2020b), invalidating simple multiplicative renormalization. Fig. 31 illustrates the mixing pattern in the RI'/MOM scheme for quark bilinear operators constructed using improved Wilson fermions with staple-shaped gauge connections in the case of a purely transverse quark operator separation b (Shanahan *et al.*, 2020b).

Finally, by extending calculations of (61) to nonzero transverse momentum transfer $\Delta_T = P' - P$, one can correlate quark transverse momentum with position; Δ_T is Fourier conjugate to the quark impact parameter $\mathbf{r_T}$. This allows one to directly access longitudinal quark orbital angular momentum (OAM), $\langle \mathbf{r_T} \times \mathbf{k_T} \rangle$. The choice of gauge link $\mathcal{U}$ corresponds to different decompositions of proton spin. A staple link extending to infinity, such as used in standard TMD PDF studies, yields Jaffe-Manohar OAM, whereas the $\eta = 0$ limit yields Ji OAM (Burkardt, 2013; Hatta, 2012; Ji *et al.*, 2012; Rajan *et al.*, 2016, 2018). By varying η within a lattice calculation, a continuous, gauge-invariant
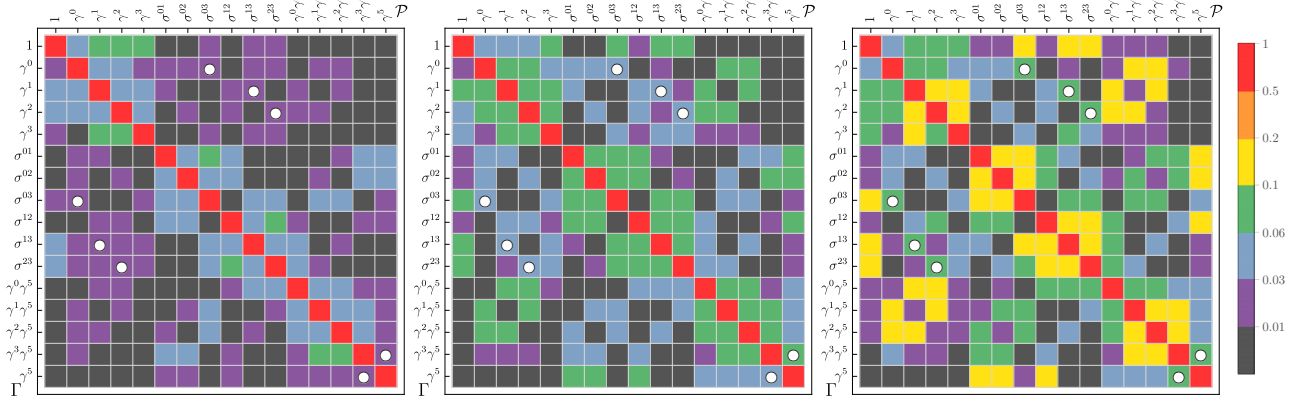
FIG. 31 Mixing pattern in the RI'/MOM scheme for quark bilinear operators constructed using improved Wilson fermions with staple-shaped gauge connections. The quark operator separation b is purely transverse, with $b_T/a = 3, 7, 11$ from left to right, where $a = 0.06$ fm denotes the lattice spacing. The staple length is given by $\eta/a = 14$. Colors indicate mixing strengths. White circles indicate mixings already obtained in one-loop lattice perturbation theory (Constantinou *et al.*, 2019).

interpolation between the two is obtained (Engelhardt, 2017). Fig. 32 (right) displays corresponding results reported in Ref. (Engelhardt *et al.*, 2018). Jaffe-Manohar orbital angular momentum is enhanced in magnitude compared to its Ji counterpart.

IV.4. Quasi-TMD PDFs

An alternative approach to calculating TMD PDFs from lattice QCD using so-called quasi-TMD PDFs (Ji, 2013, 2014) has been been explored recently by several groups (Ebert *et al.*, 2020a, 2019a,b, 2020b; Ji *et al.*, 2019a,b,c, 2020, 2015b; Vladimirov and Schäfer, 2020). Here, the key idea is to construct an equal-time correlator by replacing lightlike separations in (51) by a spacelike separation along the z direction alone. Under a Lorentz boost, these spacelike directions approach the lightcone, with the mismatch being accounted for by a perturbative matching.

Following the notation of Ref. (Ebert *et al.*, 2019b), we define the quasi-TMD PDF analogous to (50) as

$$
\tilde{f}_{i/P}(x, \mathbf{b_T}, \mu, P^z) = \lim_{\substack{a \to 0 \\ \eta \to \infty}} \tilde{Z}^i_{\text{uv}}(\mu, a)
$$
$$
\times \tilde{f}^{0\,(u)}_{i/P}(x, \mathbf{b_T}, a, \eta, P^z) \tilde{\Delta}^q_S(\mathbf{b_T}, a, \eta). \quad (65)
$$

Here, the lattice spacing a acts as UV regulator, η limits the length of the Wilson lines, and $\tilde{\Delta}^q_S$ is a quasi-soft factor required to cancel divergences as $\eta/b_T \to \infty$. While it has been shown in Ref. (Ebert *et al.*, 2019b) that there is no straightforward construction of a quasi-soft factor directly related to the soft functions appearing in (50), Ref. (Ji *et al.*, 2019b) recently proposed to calculate it within lattice QCD, employing a formulation based on heavy-quark effective theory. Importantly, this factor cancels in ratios of quasi-TMD PDFs, and

hence, similarly to the method discussed in IV.3, a determination of $\tilde{\Delta}^q_S$ is not needed to access such ratios.

The unsubtracted quasi-TMD PDF is defined as

$$
\tilde{f}^{0\,(u)}_{i/P}(x, \mathbf{b_T}, a, \eta, P^z) = \int \frac{db^z}{2\pi} e^{ib^z(xP^z)} N_{\tilde{\Gamma}}
$$
$$
\times \left\langle P \middle| \bar{q}(b/2) \tilde{\mathcal{U}} \frac{\tilde{\Gamma}}{2} q(-b/2) \middle| P \right\rangle, \quad (66)
$$

where $b^\mu = (0, \mathbf{b_T}, b^z)$, and the Wilson line path $\tilde{\mathcal{U}}$ is chosen such that it connects $b/2 \to (0, \mathbf{b_T}/2, \eta) \to (0, -\mathbf{b_T}/2, \eta) \to -b/2$. For unpolarized TMD PDFs, the Dirac structure can be chosen as $\tilde{\Gamma} = \gamma^0, \gamma^3$, with the normalization factor $N_{\gamma^0} = 1$, $N_{\gamma^3} = P^z/P^0$.

For polarized quarks and protons, one can generalize (66) using different Dirac structures $\tilde{\Gamma}$. However, the relation between quasi-TMD PDFs and TMD PDFs has been argued to be spin-independent (Ebert *et al.*, 2020a; Vladimirov and Schäfer, 2020), and hence the following results also apply to the polarized case.

The key relation between quasi-TMD PDFs and TMD PDFs is (Ebert *et al.*, 2019b; Ji *et al.*, 2019c, 2020; Vladimirov and Schäfer, 2020)

$$
\tilde{f}_{\text{ns}}(x, \mathbf{b_T}, \mu, P^z) = C_{\text{ns}}(\mu, xP^z) g^S_q(b_T, \mu)
$$
$$
\times \exp\left[\frac{1}{2} \gamma^q_\zeta(\mu, b_T) \ln \frac{(2xP^z)^2}{\zeta}\right] f_{\text{ns}}(x, \mathbf{b_T}, \mu, \zeta), \quad (67)
$$

which holds up to corrections in b_T/η, $1/(b_T P^z)$ and $1/(P^z\eta)$. In (67), the quasi-TMD PDF $\tilde{f}_{\text{ns}}$ in the nonsinglet ns $= u - d$ channel is related to the TMD PDF f_{ns} through a perturbative kernel C_{ns}, which is known at one loop (Ebert *et al.*, 2019b). It also involves a nonperturbative factor g^S_q because the quasi-TMD PDF was not defined with the physical soft function. In the approach of Ref. (Ji *et al.*, 2019b), it corresponds to the reduced soft factor, $g^S_q = \sqrt{S_r}$, see also
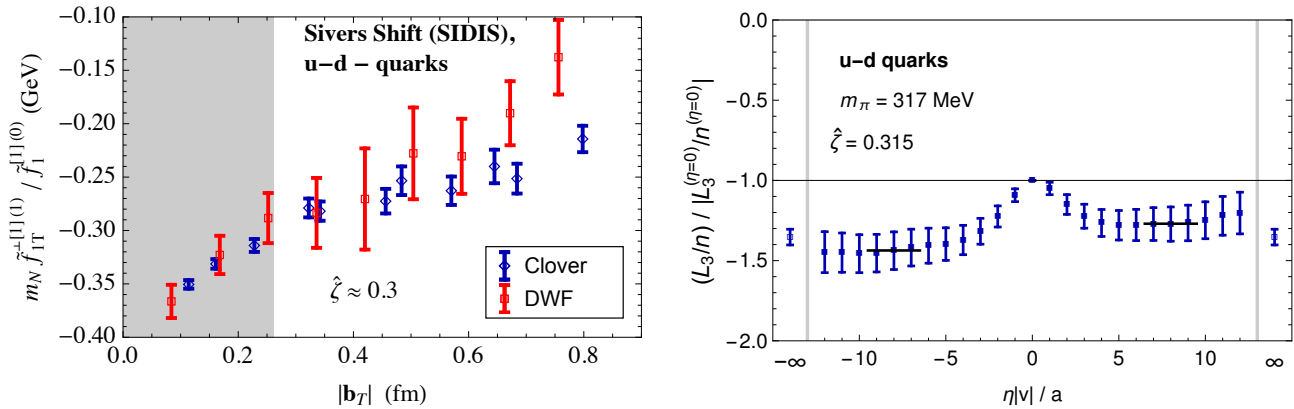
FIG. 32 Left: Comparison between SIDIS-limit data for the proton Sivers shift obtained for two distinct lattice discretizations, as a function of b_T at fixed $\hat{\zeta}$ (Yoon *et al.*, 2017). The data are compatible within uncertainties, suggesting that no significant violations of multiplicative renormalization are present. Right: Longitudinal quark OAM in the proton L_3 as a function of staple length at fixed $\hat{\zeta}$ (Engelhardt *et al.*, 2018). The limit $\eta = 0$ yields Ji OAM, $\eta \to \pm\infty$ Jaffe-Manohar OAM. The ratio of L_3 to the number of valence quarks n is evaluated to cancel multiplicative renormalizations, analogous to Eq. (63). Data are shown in units of the absolute value of Ji OAM.

Ref. (Ji *et al.*, 2020). Once calculations of this reduced soft factor become available, quasi-TMD PDFs can be formulated without this nonperturbative factor (Ji *et al.*, 2019b,c). Lastly, (67) also involves the nonperturbative CS evolution kernel, see (56), which relates the hadron energies P^z and ζ.

The Collins-Soper kernel γ_ζ is required to relate TMD PDFs at different hadron energies, and thus its nonperturbative determination from lattice QCD is of key interest. Based on (67), Refs. (Ebert *et al.*, 2019a,b) proposed to determine it from ratios of quasi-TMD PDFs at different momenta $P_1^z \neq P_2^z$,

$$\gamma_\zeta^q(\mu, b_T) = \frac{1}{\ln(P_1^z/P_2^z)} \ln \frac{C_{\mathrm{ns}}(\mu, xP_2^z)\, \tilde{f}_{\mathrm{ns}}(x, \mathbf{b_T}, \mu, P_1^z)}{C_{\mathrm{ns}}(\mu, xP_1^z)\, \tilde{f}_{\mathrm{ns}}(x, \mathbf{b_T}, \mu, P_2^z)}, \tag{68}$$

see also Ref. (Vladimirov and Schäfer, 2020) for a related proposal. In the ratio in (68), the quasi-soft factor $\tilde{\Delta}_S^q$ cancels, and thus the Collins-Soper kernel can be obtained from a ratio of unsubtracted (but renormalized) quasi-TMD PDFs alone. Another key advantage is the independence of (68) on the hadron state, and hence it can be calculated in a pion state rather than a proton state.

Without $\tilde{\Delta}_S^q$, both numerator and denominator in (68) suffer from divergences associated with Wilson-line self energies, that is, divergences in η/b_T. These divergences cancel in the ratio, but in practice it can be numerically more reliable to enforce this cancellation separately in numerator and denominator. In Ref. (Ebert *et al.*, 2020b), it was suggested to insert a common renormalization factor determined nonperturbatively in the RI'/MOM scheme on the lattice, and its conversion to the $\overline{\mathrm{MS}}$ scheme was calculated at one loop. The first lattice studies of this renormalization factor were explored in Ref. (Shanahan *et al.*, 2020b), revealing significant operator mixing on the lattice, cf. Fig. 31, which was treated by diagonalizing the renormalization and matching matrices for the RI'/MOM scheme.

The feasibility of the above method of determining the Collins-Soper kernel was demonstrated in Ref. (Shanahan *et al.*, 2020a) using a lattice of size $L^3 \times T = (2 \text{ fm})^3 \times 4$ fm and lattice spacing $a = 0.06$ fm with a heavy pion mass $m_\pi = 1.2$ GeV. Taking advantage of (68) being independent of the hadron state, the Collins-Soper kernel for $n_f = 0$ quark flavors was extracted from a quenched calculation of quasi TMD PDFs in a pion state with momenta $P^z \in \{1.29, 1.94, 2.58\}$ GeV. The study found that the extrapolation of the position-space matrix element to $b^z \to \infty$ poses a key challenge in the Fourier transform in (66). Two different fits to the lattice data were performed using Bernstein and Hermite polynomials, and strong sensitivity to the finite size of the lattice was observed by comparing the extrapolations of the two polynomial fits to $b^z > L/2$. Additional systematic effects from the power corrections mentioned below (67) could not be resolved with the limited data from the employed lattice simulation. Nevertheless, promising results were obtained, demonstrating that lattice results for the CS kernel in the nonperturbative region up to $b_T \sim 1$ fm are tractable provided that future calculations are performed on significantly larger lattice volumes.

Figure 33 shows the result of Ref. (Shanahan *et al.*, 2020a) for the b_T-dependence of the CS kernel, comparing their two extractions using Bernstein and Hermite polynomials to perturbative predictions of the same quantity. The perturbative results diverge at $b_T \approx 0.25$ fm due to the Landau pole of the strong coupling, while the lattice calculation yields encouraging results for
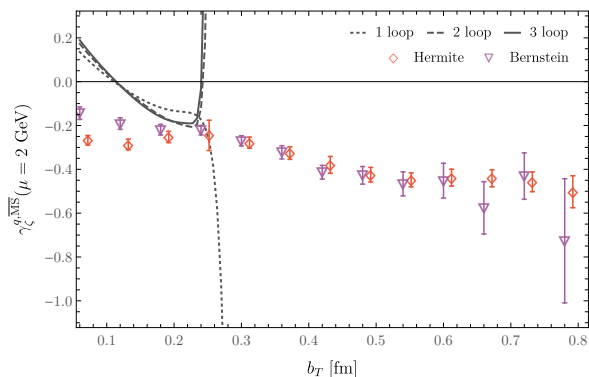
FIG. 33 Results of Ref. (Shanahan *et al.*, 2020a) for the b_T-dependence of Collins-Soper evolution. The red and purple data exhibit results using two different interpolations of the unsubtracted quasi-TMD PDF. The dashed and solid lines indicate perturbative results for the same quantity, which break down at the Landau pole at $b_T \approx 0.25$ fm. Both in the small-b_T limit as well as in the large-b_T region there are additional systematic uncertainties owing to power corrections that have not been estimated in the figure.

all values of b_T, except for very small b_T where $1/(b_T P^z)$ power corrections become important.

It will also be interesting to consider other ratios of TMD PDFs obtained from lattice QCD, for example ratios of (quasi-)TMD PDFs in different hadron states, or ratios of spin-dependent (quasi-)TMD PDFs. Such ratios of quasi-TMD PDFs are independent of the soft factor, and, when evaluated at equal momenta, are furthermore independent of the CS evolution in (67); they can thus be related perturbatively to corresponding ratios of TMD PDFs. Of particular value will be lattice results of sufficient quality, and in the relevant kinematical regimes, to be useful as auxiliary input to phenomenological fits of TMD PDFs, discussed in the next section.

IV.5. Status of global TMD fits

TMD PDFs carry rich information on parton confined motion inside a bound hadron, as well as on correlations between the motion of quarks and gluons and the direction of hadron spin. Their information can be extracted from data on QCD factorizable hadronic cross sections or lattice observables (such as quasi- or pseudo-TMD PDFs), and their properties could also be studied in terms of model calculations. The limited kinematic coverage for the differential cross sections provided by experimental data leads to a challenging inverse problem; it is unlikely, if not impossible, that one can completely fix the TMD PDFs as continuous functions over the full range of kinematics. To pin down TMD PDFs to the best possible accuracy, we need data from multiple observables, experimentally measured or calculated within Lattice QCD, that are related to

the same universal set of TMD PDFs, covering a wide kinematic regime, and to perform QCD global analyses and fits, similar to what is done to extract the PDFs as described in Sec. II.3.

However, there are fundamental differences between global fits to extract PDFs and the global fits for extracting TMD PDFs. With the linear DGLAP evolution equations, PDFs are uniquely determined once we have a set of input PDFs as a function of x at a lowest possible input hard scale $Q_0 \sim$ GeV, since all DGLAP evolution kernels are perturbatively calculable for scales larger than Q_0. Then, PDFs at $Q > Q_0$ *can* be generated by the DGLAP evolution, which is the predictive power of QCD dynamics and its factorization formalism.

For TMD PDFs with two momentum scales, Q and k_T (or its Fourier conjugate b_T), QCD evolution involves two coupled evolution equations and covers a two-dimensional phase space, e.g., (Q, b_T), where $b_T \in [0, \infty)$ (Collins *et al.*, 1985). As a consequence, the path used in solving these two coupled equations is not unique, which could affect the size of higher order corrections, leading to an additional scheme dependence of the TMD PDFs (Scimemi and Vladimirov, 2019). However, the fundamental and most important difference from DGLAP evolution is that evolution kernels for evolving TMD PDFs from an input scale Q_0 to any higher observed scale Q, referred as the Collins-Soper kernels (cf. Sec. IV.2), depend on the value of b_T, and are not perturbatively calculable for the region where $b_T > 1/Q_0$. That is, if the Fourier transform to obtain momentum space k_T-dependent TMD PDFs, which are needed for evaluating momentum-space cross sections, is sensitive to the large b_T-region of the evolved b_T-distributions, QCD perturbation theory and its factorization formalism *cannot* uniquely generate TMD PDFs at a large scale Q from input TMD PDFs at Q_0 as a function of x and k_T (or b_T in Fourier space) (Collins *et al.*, 1985).

In high energy collisions, a parton shower develops following the breaking up of the colliding hadron(s), and the characteristics of the shower depend on the hard scale of the collision Q and the available phase space for the shower, which is sensitive to probed parton momentum fraction x (Grewal *et al.*, 2020). Consequently, the probed active parton's k_T in hard collisions, described by the measured TMD PDFs, is not the same as the intrinsic transverse momentum k_{T_0} of the same parton inside a bound hadron. The difference is encoded in the QCD evolution of TMD PDFs. For physical observables whose momentum transfer Q is large and active parton x is effectively small, such as the transverse momentum $\mathbf{q_T}$-dependence of W/Z or Higgs production at collider energies, QCD evolution (or the effect of the shower) is dominated by perturbatively calculable large logarithms, or equivalently, the $\mathbf{b_T}$-dependence of the relevant TMD PDFs in Fourier space is completely dominated by the perturbative small-b_T region (Grewal

et al., 2020; Qiu and Zhang, 2001b). In this case, non-perturbative evolution kernels from the large-b_T region are effectively irrelevant, the extracted k_T-dependence of TMD PDFs for these observables is perturbatively generated (by the calculable part of the shower), and the only relevant non-perturbative information is given by normal collinear PDFs. Physically, for such observables and the corresponding TMD PDFs, the information on non-perturbative partonic motion (or intrinsic k_{T_0}-dependence) inside a bound hadron was diluted by the tremendous shower developed during the collision (or the effective $\langle \mathbf{k_{T_0}}^2 \rangle \ll \langle \mathbf{q_T}^2 \rangle$). In this case, QCD perturbation theory and its TMD factorization formalism should have excellent predictive power similar to that of collinear factorization (Berger and Qiu, 2003; Grewal *et al.*, 2020; Qiu and Zhang, 2001a). QCD global analyses and fits of data on this kind of observable at high energy colliders should provide excellent precision tests of QCD factorization and resummation of large logarithms, and additional opportunities or channels to explore new physics; they should be pursued for LHC physics.

On the other hand, for extracting information on the motion of quarks and gluons inside a bound hadron, a fundamental emergent QCD phenomenon, we need to probe TMD PDFs through scattering processes with relatively less dilution from partonic showers, and observables with a relatively smaller momentum transfer Q. In this case, QCD evolution (or the connection between the measured k_T-dependence at the hard collision scale Q and the intrinsic k_{T_0} dependence inside a bound hadron) is very much sensitive to the non-perturbative large b_T region (Grewal *et al.*, 2020; Qiu and Zhang, 2001b; Scimemi and Vladimirov, 2019). Any global analyses of TMD PDFs and fits of data from this kinematic regime have to clearly define how the non-perturbative evolution in the large b_T-regime is treated (Collins and Rogers, 2015).

There have been three types of approaches to treating the non-perturbative evolution in the large-b_T regime. As originally proposed in the pioneering paper on TMD physics (or physics of two-scale observables) (Collins *et al.*, 1985), the evolution is completely taken care of by perturbative Collins-Soper evolution kernels in the small b_T-regime by introducing a "b^*-prescription",

$$f_{i/P}(x, \mathbf{b_T}, Q) \equiv f_{i/P}(x, \mathbf{b_T}^*, Q)\, F^{\mathrm{NP}}(x, \mathbf{b_T}, Q)\,, \quad (69)$$

where $\mathbf{b_T}^* \equiv \mathbf{b_T}/\sqrt{1 + (b_T/b_{T_{\max}})^2}$, such that $b_T^* < b_{T_{\max}}$ for $b_T \in [0, \infty)$, and $F^{\mathrm{NP}}(x, \mathbf{b_T}, Q)$ is a nonperturbative function to be fitted through data from global fits (Collins and Rogers, 2015; Davies *et al.*, 1985; Landry *et al.*, 2003; Meng *et al.*, 1996). The second approach is to keep the perturbatively evolved TMD PDFs in the small-b_T region as they are, and introduce a model evolution kernel for the large-b_T region whose parameters are fitted by experimental data (Qiu and

Zhang, 2001b; Scimemi and Vladimirov, 2019). The third approach is to calculate these non-perturbative evolution kernels within lattice QCD, as discussed in the previous subsection, an approach which needs to be explored further. In view of the reach of lattice TMD calculations performed to date, it seems plausible to anticipate that, in the medium term, obtaining non-perturbative evolution kernels with an accuracy in the range of 10-20% up to $b_T \sim 1$ fm at hadron momenta up to about $2\,\mathrm{GeV}$ at the physical pion mass will be possible. The restriction in the hadron momentum is likely to remain a significant source of systematic uncertainty, engendering higher-twist power corrections that must be brought under numerical control. Also effects of the finite size of the lattice are still only rudimentarily understood. Nonetheless, such input could provide valuable additional information for global fits.

Phenomenologically, most efforts to extract TMD PDFs from existing data are concentrated on the unpolarized $f_1(x, k_T^2)$ in Eq. (58). In recent years, there has been tremendous progress both in the accuracy of the theoretical framework and in the dimension of the data set included in the fit. Extractions of $f_1(x, k_T^2)$ from SIDIS data were performed in the so-called extended parton model (Anselmino *et al.*, 2014; Signori *et al.*, 2013) (the latter being the only analysis so far with an explicit flavor dependence in the fitting parameters of the functional form), and were followed by extractions in the appropriate TMD framework but limited to Drell-Yan and Z-boson production data. In these cases, the description of the TMD evolution formula (57) was continuously improved, moving from the NLL level (Bacchetta *et al.*, 2017; Echevarria *et al.*, 2014; Sun *et al.*, 2018) through the NNLL one (Bertone *et al.*, 2019; D'Alesio *et al.*, 2014; Scimemi and Vladimirov, 2018), up to the NNNLL level (Bacchetta *et al.*, 2019a; Scimemi and Vladimirov, 2019) that matches the accuracy of standard phenomenology at the LHC (see Table 1 and Sec. 2.3 of Ref. (Bacchetta *et al.*, 2019a) for more details on the perturbative expansion). In the most recent analyses (Bacchetta *et al.*, 2019a; Bertone *et al.*, 2019; Scimemi and Vladimirov, 2018, 2019), very precise data from the LHC (in particular, from ATLAS) were included in the fit and turned out to have a large impact on the behaviour of $f_1(x, k_T^2)$ at small x. Conversely, the impact of a flavor-dependent TMD (as obtained from the low-energy analysis of Ref. (Signori *et al.*, 2013)) on the extraction of Standard Model parameters at the LHC was explored in Ref. (Bacchetta *et al.*, 2019c) using the template-fit technique, reaching the conclusion that flavor sensitivity in the intrinsic quark transverse momentum might induce an additional uncertainty in the extraction of the W boson mass that is comparable to the error correlated to PDF uncertainties.

The first extraction of $f_1(x, k_T^2)$ in the TMD framework from a global fit of both SIDIS data and measurements

of the Drell-Yan and Z-boson production processes can be found in Ref. (Bacchetta *et al.*, 2017). The approach is based on the description at NLL of the perturbative Collins-Soper evolution kernel plus a modified "b^*-prescription". The fit includes 8059 data points with a quality of $\chi^2/\text{d.o.f.} = 1.55 \pm 0.05$ with only 11 parameters. The results confirm the universality of TMD PDFs but show a marked anti-correlation between TMD PDFs and TMD FFs, calling for an independent extraction of transverse-momentum dependent fragmentation functions from e^+-e^- annihilation data (which is still missing). The same finding is obtained in the more recent global fit of Ref. (Scimemi and Vladimirov, 2019), where the perturbative accuracy of the TMD at small b_T is pushed to the NNNLO level and the nonperturbative part of the evolution at large b_T is fitted to data. The analysis of Ref. (Scimemi and Vladimirov, 2019) includes recent very precise LHC data, although the total number of analyzed data points (1039) falls short of the hitherto largest set of 8059 analyzed in Ref. (Bacchetta *et al.*, 2017).

As for polarized TMD PDFs in Eq. (58), the best known is the Sivers function $f_{1T}^\perp(x, k_T^2)$. It describes how the k_T distribution of an unpolarized quark is distorted in a transversely polarized hadron (Sivers, 1990). In fact, for a nucleon with mass M moving along the $\hat{z}$ direction and transversely polarized along the $\hat{y}$ direction, the probability density of a quark with flavor q is given, at a certain (understood) scale Q, by

$$f_{q/N\uparrow}(x, k_x, k_y) = f_1^q(x, k_T^2) - f_{1T}^{\perp q}(x, k_T^2)\frac{k_x}{M}, \quad (70)$$

cf. Eq. (58). If the nucleon were unpolarized, the $f_{q/N}$ would be determined only by the unpolarized TMD PDF f_1 and the density would be perfectly symmetric around the $\hat{z}$ direction. The transverse polarization of the nucleon induces a distortion of the density along the $\hat{x}$ direction through the Sivers TMD PDF $f_{1T}^\perp$. Evidently, $f_{1T}^\perp$ describes a spin-orbit effect at the partonic level. The Sivers function is representative of the class of naïve T-odd TMDs, namely of those TMDs that are not constrained by T-reversal invariance (Boer and Mulders, 1998). Their universality is broken but in a calculable way. For example, the Sivers function extracted in a Drell-Yan process with a transversely polarized proton should turn out opposite to the one that is extracted in SIDIS. The $f_{1T}^\perp|_{\text{DY}} = -f_{1T}^\perp|_{\text{SIDIS}}$ prediction is based on very general assumptions, and it represents a fundamental test of QCD (Collins, 2002). Therefore, it is the subject of intense experimental investigation. Preliminary results hint to statistically favor the prediction (Adamczyk *et al.*, 2016; Aghasyan *et al.*, 2017; Anselmino *et al.*, 2017) although more precise data are needed to draw a sharp conclusion. Many parametrizations of the Sivers function are available (for example, see Refs. (Anselmino *et al.*, 2012; Aybat *et al.*,
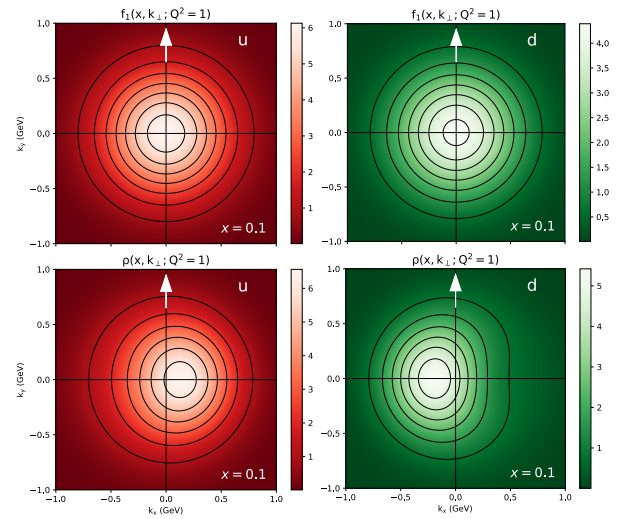

FIG. 34 Upper panels: quark density $f_{q/N} = f_1(x = 0.1, k_T^2)$ at $Q^2 = 1$ GeV^2 for an unpolarized proton moving ideally towards the reader; left panel for up quark, right panel for down quark. Lower panels: quark density $f_{q/N\uparrow} = f_1(x = 0.1, k_T^2) - f_{1T}^{\perp q}(x = 0.1, k_T^2)k_x/M$ in the same conditions but for a proton transversely polarized along the $\hat{y}$ direction (see text).

2012; Bacchetta and Radici, 2011; Boer, 2013; Collins *et al.*, 2006; Sun and Yuan, 2013; Vogelsang and Yuan, 2005)). In Ref. (Bacchetta *et al.*, 2020b), the density $f_{q/N\uparrow}$ of Eq. (70) is reconstructed by combining the extraction of the unpolarized f_1 from Ref. (Bacchetta *et al.*, 2017) with the extraction of the Sivers $f_{1T}^\perp$ from SIDIS data in the same approach. In this way, the quark density is reconstructed in a consistent way from real experimental data for nucleons with or without transverse polarization. In Fig. 34, $f_{q/N\uparrow}$ is represented at $x = 0.1$ and $Q^2 = 1$ GeV^2 for a proton ideally moving towards the reader. The upper panels correspond to the symmetric situation of an unpolarized proton. The lower panels show the distortion along the $\hat{x}$ direction induced by the transverse polarization along the $\hat{y}$ direction, which turns out opposite for the up quark (left panel) and the down quark (right panel). The tomography depicted in Fig. 34 gives a realistic estimate of the non-trivial correlation between the motion of quarks and the spin direction of the parent proton.

As for the transversity TMD PDF $h_1(x, k_T^2)$ in Eq. (58), we refer to Sec. II.1.4. Very recently, a global fit of all single-spin asymmetries involving polarized TMDs in SIDIS, Drell-Yan, e^+-e^- annihilation, and hadron-hadron collision processes has been presented in Ref. (Cammarota *et al.*, 2020), extracting a universal set of TMD functions including the Sivers and the transversity distributions. However, the analysis was not performed in the TMD framework, thus neglecting the effects of TMD evolution which might be important when

connecting experimental data collected at very different scales.

In summary, it has now become possible to build the first accurate tomography in momentum space of quarks inside (polarized) nucleons, and we can describe how this picture evolves with the hard scale Q and how it changes with the quark longitudinal momentum fraction x. However, we have no similar results for the gluon TMD PDFs. Several studies have explored useful channels at RHIC and the LHC with $p - p$ collisions leading to $J/\psi + X$, or $J/\psi + \gamma + X$, or $\eta_c + X$ final states (Boer et al., 2016; D'Alesio et al., 2019, 2017; den Dunnen et al., 2014). At the EIC, it would be possible to consider also SIDIS processes like $e - p$ collisions leading to $J/\psi + X$, $h_1 + h_2 + X$, jet+jet+X, J/ψ+jet+X final states (Bacchetta et al., 2020a; Boer et al., 2016; Mukherjee and Rajesh, 2017; Rajesh et al., 2018).

With more and higher quality data becoming available from Jefferson Lab at 12GeV, COMPASS at CERN, and the future EIC, and a better understanding of non-perturbative evolution at large b_T from lattice QCD calculations, the community should be able to perform much more accurate global fits of TMD PDFs to learn about the "true" confined partonic motion in hadrons, isolating it from the contamination from parton showers triggered by high energy collisions. In addition to the specific issue of the Collins-Soper evolution kernel highlighted above, lattice QCD can provide further auxiliary input for future global fits. TMD observables at separations up to $b_T \sim 1$ fm at hadron momenta up to about 2 GeV will be accessible at the physical pion mass in the medium term, where it can be expected that moments in the momentum fraction x will continue to be obtained with better precision than the x-dependent quantities, even as determinations of the latter are developed. Used to anchor phenomenological fits, such moments may represent the most accessible avenue for lattice QCD to contribute to global fit efforts.

V. OUTLOOK, CHALLENGES & CONCLUSIONS

V.1. Outlook

The study of the distributions of partons into hadrons is an active interdisciplinary research field lying at the crossroads of high-energy, hadronic and nuclear physics. In this report, we have provided a succinct review of recent developments concerning PDFs, GPDs and TMD PDFs from both nonperturbative lattice QCD and perturbative global analysis. Throughout, we have highlighted the synergy between these two distinct approaches and provided examples of where each can reinforce the other.

From the perspective of QCD global analysis, fits of PDFs, GPDs and TMD PDFs are often limited by kinematical regions which have either been weakly probed experimentally or are inaccessible to contemporary measurements, such as (very) high or (very) low x, in the case of PDFs. Similarly, precise extractions of the flavor dependence of the PDFs and related quantities are frequently hindered by the sparsity of data with direct sensitivity. For instance, in studies of unpolarized PDFs, determinations of the nucleon's strangeness content commonly require final-state tagging of charm quarks in dimuon production off nuclei or other semi-inclusive processes for which various ambiguities exist regarding the treatment of nuclear medium effects, hadronization, and other issues. Due to these complexities, lattice-QCD data on PDF moments or quasi-/pseudo-distributions can already have a valuable impact as fitted data or theoretical priors in global PDF fits. In contrast, contemporary data informing the u- and d-quark distributions are sufficiently constraining that lattice calculations on the lowest PDFs moments do not yet possess the needed precision to be quite as informative in a global analysis. All the same, technical improvements in the evaluation of PDF moments, the extension of lattice calculations to higher moments, and supplementation of this information with quasi- and pseudo-PDFs will gain pace in coming years. These developments suggest the possibility of future global PDF fits in which extractions of unpolarized PDFs are augmented by an array of lattice calculations that provide enhanced precision.

Strategies and theory developments for this approach can be guided by lattice calculations and QCD analyses for the comparatively less constrained partonic distributions, such as the helicity and transversity collinear distributions, GPDs, and TMD PDFs.. The impact of lattice calculations in QCD global fits can be reciprocally enhanced by the phenomenological determinations themselves, which, by their precision, can provide benchmarks for many standard lattice observables. We therefore envision a PDF-Lattice synergy deriving from the ability of QCD global fitters

to drive improvements in lattice calculations with benchmarks informed by high-energy data, while the lattice provides informative constraints in kinematical regions that are otherwise challenging to constrain empirically.

As an essential ingredient for this relationship, both communities must establish a common basis for comparing results from lattice QCD and global fits — a challenging undertaking given the complex contemporary landscape of lattice calculations and global fits, which involve a patchwork of theoretical settings, systematic assumptions, and, in the case of QCD analyses, empirical data sets. This is a primary goal of this report, which, in addition to numerous updates, aimed to extend the comparative PDF-lattice basis from the arena of collinear distributions developed in the 2017 PDFLattice white paper to multidimensional distributions for which lattice information can more immediately drive global fits. The study of 1-dimensional collinear unpolarized PDFs is a very mature field and benefits from decades of intense experimental and theoretical accomplishments. By contrast, study of the collinear helicity and transversity PDFs and of the 3-dimensional hadronic structure represents a comparatively new field which offers a wealth of opportunities for new measurements, tools, and ideas.

The TMD PDFs and GPDs discussed in this report are examples of how we can augment our current collinear PDFs to more fully map out the hadronic structure. These generalized distributions provide a special opportunity with new facilities on the horizon such as the HL-LHC, LHeC, and EIC. For example, the EIC is well suited to perform hadron tomography measurements, given its high-luminosity coverage of the low Q^2 quark-hadron transition region in the kinematical parameter space. These hadron tomography measurements can be crucial in unfolding the nucleon's collinear and transverse structure at scales adjacent to the nucleon mass, and for constraining the quantities accessible in next-generation lattice-QCD calculations.

V.2. Challenges

Looking ahead to the next decade, what will we need to accomplish?.

- For the unpolarized proton PDFs, the goal is to continue reducing uncertainties so these are no longer a limiting factor for many precision measurements. These analyses are performed at NNLO as standard. It will take a concerted effort on both the experimental and theoretical fronts to move these analyses to the next desired precision.

- For the helicity and transversity PDFs, knowledge is significantly more limited than for unpolarized PDFs, both theoretically and experimentally. The standard accuracy for global analyses of these PDFs is currently NLO and LO, respectively. The quality and quantity of data limit their sensitivity to only a limited subset of partons in a fairly restricted kinematic region. This state of affairs will be overcome by the advent of an EIC.

- For the nuclear PDFs, the uncertainties are significantly larger than those for the proton PDFs. The nuclear PDF analyses have more degrees of freedom, but typically have less data points than the proton PDFs; hopefully, this situation will be remedied by the proposed experimental facilities. Additionally, new Lattice QCD efforts are beginning to explore light nuclei; this could be helpful in describing nPDFs as simple A-dependent interpolations in this region may be insufficient. As the nPDF precision increases, we can being to investigate collective effects and other phenomena that are present for nuclei but may not be evident in the proton.

- In lattice QCD, calculations of PDF moments have improved for both unpolarized, helicity and transversity moments. Additionally, new ideas on QCD factorizable and lattice-QCD calculable quantities, such as quasi- and pseudo-PDFs and correlations of currents, offer new avenues of inquiry and the possibility to extract PDFs over a broader range of x. Theoretical efforts in identifying new QCD factorizable quantities, especially those difficult to measure experimentally, would allow us to leverage the the power of lattice QCD to map out unknown structures.

- The study of GPDs offers insight into the 3D structure of the nucleon via exclusive processes such as DVCS and meson production. A significant challenge of these measurements is that they involve a larger number of variables as compared to collinear PDFs. As such, progress on this topic will require a multifaceted effort combining new experimental data with a variety of theoretical methods including Mellin moments, quasi- and pseudo-distributions, and Machine Learning to provide a 3D tomographic image of the nucleon structure.

- The extension of collinear PDFs to TMD PDFs provides a new and fertile area for research, and there are a number of topics which are particularly well suited to the Lattice QCD approach. Recent progress has enabled these calculations to scan the $(b \cdot P)$-dependence of the hadronic matrix elements to access the x-dependence of the TMD PDFs. Further extensions of the calculations to nonzero transverse momentum transfer offer the possibility to measure the quark orbital angular momentum. These advances, combined with recent work that provides a rigorous theoretical formalism for the TMD PDF framework, indicate a promising future for this line of research.

V.3. Conclusions

This report is the outcome of a 2019 workshop which brought the perturbative and non-perturbative PDF communities together to address how a combined effort from these complementary perspectives can advance our knowledge of the nucleon structure. In addition to providing an update of the traditional collinear PDFs, we have extended our analysis to include both the GPDs and TMD PDFs which, when taken together, can provide a complete description of both the transverse motion and position of the partons inside a nucleon.

The broader scope of our investigations highlights areas where perturbative global PDF analyses and the Lattice QCD calculations can benefit each other. For example, the global analyses of the unpolarized collinear PDFs are very mature and can thus provide constraints which can be utilized by the Lattice QCD calculations. Conversely, for some of the polarized and generalized PDF measurements, the Lattice QCD approach can provide important inputs.

With the prospect of new facilities and experiments in the near future, there is a urgent need for improved theoretical tools to keep pace with the experimental data. This work is ongoing, and the techniques and methods described here will not only form the basis of next-generation PDFs, but also afford a deeper understanding of the QCD theory which will facilitate precision measurements and new discoveries for future experiments.

REFERENCES

Aad, G., *et al.* (ATLAS) (2014), JHEP **05**, 068, arXiv:1402.6263 [hep-ex].

Abdel-Rehim, A., *et al.* (ETM) (2017), Phys. Rev. **D95** (9), 094515, arXiv:1507.05068 [hep-lat].

Abdul Khalek, R., J. J. Ethier, and J. Rojo (NNPDF) (2019a), Eur. Phys. J. **C79** (6), 471, arXiv:1904.00018 [hep-ph].

Abdul Khalek, R., *et al.* (NNPDF) (2019b), Eur. Phys. J. **C**, 79:838, arXiv:1905.04311 [hep-ph].

Abdul Khalek, R., *et al.* (NNPDF) (2019c), Eur. Phys. J. **C79** (11), 931, arXiv:1906.10698 [hep-ph].

Abdul Khalek, R., *et al.* (2020), arXiv:2005.11327 [hep-ph].

Abelleira Fernandez, J. L., *et al.* (LHeC Study Group) (2012), J. Phys. **G39**, 075001, arXiv:1206.2913 [physics.acc-ph].

Abramowicz, H., *et al.* (H1, ZEUS) (2015), Eur. Phys. J. C **75** (12), 580, arXiv:1506.06042 [hep-ex].

Accardi, A., L. T. Brady, W. Melnitchouk, J. F. Owens, and N. Sato (2016a), Phys. Rev. **D93** (11), 114017, arXiv:1602.03154 [hep-ph].

Accardi, A., *et al.* (2016b), Eur. Phys. J. **A52** (9), 268, arXiv:1212.1701 [nucl-ex].

Adam, J., *et al.* (STAR) (2018), Phys. Rev. **D98** (3), 032011, arXiv:1805.09742 [hep-ex].

Adamczyk, L., *et al.* (STAR) (2015), Phys. Rev. Lett. **115**, 242501, arXiv:1504.00415 [hep-ex].

Adamczyk, L., *et al.* (STAR) (2016), Phys. Rev. Lett. **116** (13), 132301, arXiv:1511.06003 [nucl-ex].

Adamczyk, L., *et al.* (STAR) (2017), Phys. Rev. **D95** (7), 071103, arXiv:1610.06616 [hep-ex].

Adamczyk, L., *et al.* (STAR) (2018), Phys. Lett. **B780**, 332, arXiv:1710.10215 [hep-ex].

Adolph, C., *et al.* (COMPASS) (2012), Phys. Lett. **B713**, 10, arXiv:1202.6150 [hep-ex].

Adolph, C., *et al.* (COMPASS) (2014), Phys. Lett. **B736**, 124, arXiv:1401.7873 [hep-ex].

Aghasyan, M., *et al.* (COMPASS) (2017), Phys. Rev. Lett. **119** (11), 112002, arXiv:1704.00488 [hep-ex].

Aglietti, U., M. Ciuchini, G. Corbo, E. Franco, G. Martinelli, and L. Silvestrini (1998), Phys. Lett. **B441**, 371, arXiv:hep-ph/9806277 [hep-ph].

Ahmad, S., G. R. Goldstein, and S. Liuti (2009), Phys. Rev. **D79**, 054014, arXiv:0805.3568 [hep-ph].

Airapetian, A., *et al.* (HERMES) (2008), JHEP **06**, 017, arXiv:0803.2367 [hep-ex].

Alarcon, R. (BLAST) (2007), *Proceedings, 3rd International Workshop on From parity violation to hadronic structure and more (PAVI 2006): Milos, Greece, May 16-20, 2006*, Eur. Phys. J. **A32** (4), 477, [Eur. Phys. J.A32,477(2007)].

Alekhin, S., J. Blümlein, S. Moch, and R. Placakyte (2017), Phys. Rev. **D96** (1), 014011, arXiv:1701.05838 [hep-ph].

Alexandrou, C., S. Bacchio, K. Cichy, M. Constantinou, K. Hadjiyiannakou, K. Jansen, G. Koutsou, A. Scapellato, and F. Steffens (2018a), EPJ Web Conf. **175**, 14008, arXiv:1710.06408 [hep-lat].

Alexandrou, C., S. Bacchio, M. Constantinou, J. Finkenrath, K. Hadjiyiannakou, K. Jansen, and G. Koutsou (2020a), Phys. Rev. **D101** (3), 031501, arXiv:1909.10744 [hep-lat].

Alexandrou, C., S. Bacchio, M. Constantinou, J. Finkenrath, K. Hadjiyiannakou, K. Jansen, G. Koutsou, H. Panagopoulos, and G. Spanoudes (2020b), arXiv:2003.08486 [hep-lat].

Alexandrou, C., S. Bacchio, M. Constantinou, J. Finkenrath, K. Hadjiyiannakou, K. Jansen, G. Koutsou, and A. Vaquero Aviles-Casco (2019a), Phys. Rev. **D100** (1), 014509, arXiv:1812.10311 [hep-lat].

Alexandrou, C., S. Bacchio, M. Constantinou, J. Finkenrath, K. Hadjiyiannakou, K. Jansen, G. Koutsou, and A. Vaquero Aviles-Casco (2019b), arXiv:1909.00485 [hep-lat].

Alexandrou, C., J. Carbonell, M. Constantinou, P. A. Harraud, P. Guichon, K. Jansen, C. Kallidonis, T. Korzec, and M. Papinutto (2011), Phys. Rev. **D83**, 114513, arXiv:1104.1600 [hep-lat].

Alexandrou, C., K. Cichy, M. Constantinou, K. Hadjiyiannakou, K. Jansen, H. Panagopoulos, and F. Steffens (2017a), Nucl. Phys. **B923**, 394, arXiv:1706.00265 [hep-lat].

Alexandrou, C., K. Cichy, M. Constantinou, K. Hadjiyiannakou, K. Jansen, A. Scapellato, and F. Steffens (2019c), in *37th International Symposium on Lattice Field Theory (Lattice 2019) Wuhan, Hubei, China, June 16-22, 2019*, arXiv:1910.13229 [hep-lat].

Alexandrou, C., K. Cichy, M. Constantinou, K. Hadjiyiannakou, K. Jansen, A. Scapellato, and F. Steffens (2019d), Phys. Rev. **D99** (11), 114504, arXiv:1902.00587 [hep-lat].

Alexandrou, C., K. Cichy, M. Constantinou, K. Jansen, A. Scapellato, and F. Steffens (2018b), Phys. Rev. Lett. **121** (11), 112001, arXiv:1803.02685 [hep-lat].

Alexandrou, C., K. Cichy, M. Constantinou, K. Jansen, A. Scapellato, and F. Steffens (2018c), Phys. Rev. **D98** (9), 091503, arXiv:1807.00232 [hep-lat].

Alexandrou, C., K. Cichy, V. Drach, E. Garcia-Ramos, K. Hadjiyiannakou, K. Jansen, F. Steffens, and C. Wiese (2014), *Proceedings, 32nd International Symposium on Lattice Field Theory (Lattice 2014): Brookhaven, NY, USA, June 23-28, 2014*, PoS **LATTICE2014**, 135, arXiv:1411.0891 [hep-lat].

Alexandrou, C., K. Cichy, V. Drach, E. Garcia-Ramos, K. Hadjiyiannakou, K. Jansen, F. Steffens, and C. Wiese (2015), Phys. Rev. **D92**, 014502, arXiv:1504.07455 [hep-lat].

Alexandrou, C., M. Constantinou, S. Dinter, V. Drach, K. Jansen, C. Kallidonis, and G. Koutsou (2013), Phys. Rev. **D88** (1), 014509, arXiv:1303.5979 [hep-lat].

Alexandrou, C., M. Constantinou, K. Hadjiyiannakou, K. Jansen, C. Kallidonis, G. Koutsou, and A. Vaquero Aviles-Casco (2017b), Phys. Rev. **D96** (5), 054507, arXiv:1705.03399 [hep-lat].

Alexandrou, C., M. Constantinou, K. Hadjiyiannakou, K. Jansen, C. Kallidonis, G. Koutsou, and A. Vaquero Aviles-Casco (2017c), Phys. Rev. **D96** (3), 034503, arXiv:1706.00469 [hep-lat].

Alexandrou, C., M. Constantinou, K. Hadjiyiannakou, K. Jansen, C. Kallidonis, G. Koutsou, and A. Vaquero Avilés-Casco (2018d), Phys. Rev. **D97** (9), 094504, arXiv:1801.09581 [hep-lat].

Alexandrou, C., *et al.* (2017d), Phys. Rev. **D95** (11), 114514, [erratum: Phys. Rev.D96,no.9,099906(2017)], arXiv:1703.08788 [hep-lat].

Alexandrou, C., *et al.* (2020c), Phys. Rev. **D101** (3), 034519, arXiv:1908.10706 [hep-lat].

Altarelli, G., and G. Parisi (1977), Nucl. Phys. **B126**, 298.

Altinoluk, T., R. Boussarie, and P. Kotko (2019), JHEP **05**, 156, arXiv:1901.01175 [hep-ph].

Amoroso, S., *et al.* (2020), in *11th Les Houches Workshop on Physics at TeV Colliders: PhysTeV Les Houches (PhysTeV 2019) Les Houches, France, June 10-28, 2019*, arXiv:2003.01700 [hep-ph].

Anderson, B., *et al.* (Jefferson Lab E95-001) (2007), Phys. Rev. **C75**, 034003, arXiv:nucl-ex/0605006 [nucl-ex].

Angeles-Martinez, R., *et al.* (2015), Acta Phys. Polon. **B46** (12), 2501, arXiv:1507.05267 [hep-ph].

Anklin, H., *et al.* (1994), Phys. Lett. **B336**, 313.

Anklin, H., *et al.* (1998), Phys. Lett. **B428**, 248.

Anselmino, M., M. Boglione, U. D'Alesio, A. Kotzinian, F. Murgia, A. Prokudin, and C. Turk (2007), Phys. Rev. **D75**, 054032, arXiv:hep-ph/0701006 [hep-ph].

Anselmino, M., M. Boglione, U. D'Alesio, S. Melis, F. Murgia, and A. Prokudin (2013), Phys. Rev. **D87**, 094019, arXiv:1303.3822 [hep-ph].

Anselmino, M., M. Boglione, U. D'Alesio, F. Murgia, and A. Prokudin (2017), JHEP **04**, 046, arXiv:1612.06413 [hep-ph].

Anselmino, M., M. Boglione, J. Gonzalez Hernandez, S. Melis, and A. Prokudin (2014), JHEP **04**, 005, arXiv:1312.6261 [hep-ph].

Anselmino, M., M. Boglione, and S. Melis (2012), Phys.Rev. **D86**, 014028, arXiv:1204.1239 [hep-ph].

Aoki, S., *et al.* (2017), Eur. Phys. J. **C77** (2), 112, arXiv:1607.00299 [hep-lat].

Aoki, S., *et al.* (Flavour Lattice Averaging Group) (2020), Eur. Phys. J. **C80** (2), 113, arXiv:1902.08191 [hep-lat].

Artru, X., and M. Mekhfi (1990), Z. Phys. **C45**, 669.

Asakawa, M., T. Hatsuda, and Y. Nakahara (2001), Prog. Part. Nucl. Phys. **46**, 459, arXiv:hep-lat/0011040 [hep-lat].

Aschenauer, E. C., T. Burton, T. Martini, H. Spiesberger, and M. Stratmann (2013), Phys. Rev. **D88**, 114025, arXiv:1309.5327 [hep-ph].

Aschenauer, E. C., S. Fazio, M. A. C. Lamont, H. Paukkunen, and P. Zurita (2017), Phys. Rev. **D96** (11), 114005, arXiv:1708.05654 [nucl-ex].

Aschenauer, E. C., R. Sassot, and M. Stratmann (2012), Phys. Rev. **D86**, 054020, arXiv:1206.6014 [hep-ph].

Aschenauer, E. C., R. Sassot, and M. Stratmann (2015), Phys. Rev. **D92** (9), 094030, arXiv:1509.06489 [hep-ph].

Aybat, S. M., A. Prokudin, and T. C. Rogers (2012), Phys.Rev.Lett. **108**, 242003, arXiv:1112.4423 [hep-ph].

Aybat, S. M., and T. C. Rogers (2011), Phys. Rev. **D83**, 114042, arXiv:1101.5057 [hep-ph].

Babich, R., R. C. Brower, M. A. Clark, G. T. Fleming, J. C. Osborn, C. Rebbi, and D. Schaich (2012), Phys. Rev. D **85**, 054510, arXiv:1012.0562 [hep-lat].

Bacchetta, A., V. Bertone, C. Bissolotti, G. Bozzi, F. Delcarro, F. Piacenza, and M. Radici (2019a), arXiv:1912.07550 [hep-ph].

Bacchetta, A., D. Boer, C. Pisano, and P. Taels (2020a), Eur. Phys. J. **C80** (1), 72, arXiv:1809.02056 [hep-ph].

Bacchetta, A., G. Bozzi, M. Lambertsen, F. Piacenza, J. Steiglechner, and W. Vogelsang (2019b), Phys. Rev. **D100** (1), 014018, arXiv:1901.06916 [hep-ph].

Bacchetta, A., G. Bozzi, M. Radici, M. Ritzmann, and A. Signori (2019c), Phys. Lett. **B788**, 542, arXiv:1807.02101 [hep-ph].

Bacchetta, A., F. A. Ceccopieri, A. Mukherjee, and M. Radici (2009), Phys. Rev. **D79**, 034029, arXiv:0812.0611 [hep-ph].

Bacchetta, A., A. Courtoy, and M. Radici (2011), Phys. Rev. Lett. **107**, 012001, arXiv:1104.3855 [hep-ph].

Bacchetta, A., A. Courtoy, and M. Radici (2013), JHEP **03**, 119, arXiv:1212.3568 [hep-ph].

Bacchetta, A., F. Delcarro, C. Pisano, and M. Radici (2020b), arXiv:2004.14278 [hep-ph].

Bacchetta, A., F. Delcarro, C. Pisano, M. Radici, and A. Signori (2017), JHEP **06**, 081, [Erratum: JHEP06,051(2019)], arXiv:1703.10157 [hep-ph].

Bacchetta, A., M. Diehl, K. Goeke, A. Metz, P. J. Mulders, and M. Schlegel (2007), JHEP **02**, 093, arXiv:hep-ph/0611265 [hep-ph].

Bacchetta, A., and M. Radici (2003), Phys. Rev. **D67**, 094002, arXiv:hep-ph/0212300 [hep-ph].

Bacchetta, A., and M. Radici (2004), Phys. Rev. **D70**, 094032, arXiv:hep-ph/0409174 [hep-ph].

Bacchetta, A., and M. Radici (2011), Phys.Rev.Lett. **107**, 212001, arXiv:1107.5755 [hep-ph].

Backus, G., and F. Gilbert (1968), Geophysical Journal International **16** (2), 169.

Backus, G., and F. Gilbert (1970), Philosophical Transactions of the Royal Society of London A: Mathematical, Physical and Engineering Sciences **266** (1173), 123.

Bailey, S., and L. Harland-Lang (2020), Eur. Phys. J. **C80** (1), 60, arXiv:1909.10541 [hep-ph].

Bali, G. S., V. M. Braun, B. Gläßle, M. Göckeler, M. Gruber, F. Hutzler, P. Korcyl, A. Schäfer, P. Wein, and J.-H. Zhang (2018), Phys. Rev. **D98** (9), 094507, arXiv:1807.06671 [hep-lat].

Bali, G. S., S. Collins, B. Glässle, M. Göckeler, J. Najjar, R. H. Rödl, A. Schäfer, R. W. Schiel, W. Söldner, and A. Sternbeck (2015), Phys. Rev. **D91** (5), 054501, arXiv:1412.7336 [hep-lat].

Bali, G. S., S. Collins, M. Gruber, A. Schäfer, P. Wein, and T. Wurm (2019a), Phys. Lett. **B789**, 666, arXiv:1810.05569 [hep-lat].

Bali, G. S., S. Collins, M. Göckeler, R. Rödl, A. Schäfer, and A. Sternbeck (2019b), Phys. Rev. **D100** (1), 014507, arXiv:1812.08256 [hep-lat].

Bali, G. S., B. Lang, B. U. Musch, and A. Schäfer (2016), Phys. Rev. **D93** (9), 094515, arXiv:1602.05525 [hep-lat].

Balitsky, I. (1996), Nucl. Phys. **B463**, 99, arXiv:hep-ph/9509348 [hep-ph].

Balitsky, I., W. Morris, and A. Radyushkin (2019), arXiv:1910.13963 [hep-ph].

Balitsky, I. I., and V. M. Braun (1989), Nucl. Phys. **B311**, 541.

Ball, R. D., V. Bertone, M. Bonvini, S. Marzani, J. Rojo, and L. Rottoli (2018), Eur. Phys. J. C **78** (4), 321, arXiv:1710.05935 [hep-ph].

Ball, R. D., and A. Deshpande (2019), in *From My Vast Repertoire ...: Guido Altarelli's Legacy*, edited by A. Levy, S. Forte, and G. Ridolfi, pp. 205–226, arXiv:1801.04842 [hep-ph].

Ball, R. D., S. Forte, A. Guffanti, E. R. Nocera, G. Ridolfi, and J. Rojo (NNPDF) (2014), Phys. Lett. **B728**, 524, arXiv:1310.0461 [hep-ph].

Ball, R. D., E. R. Nocera, and R. L. Pearson (NNPDF) (2019), Eur. Phys. J. **C79** (3), 282, arXiv:1812.09074 [hep-ph].

Ball, R. D., *et al.* (NNPDF) (2017), Eur. Phys. J. **C77** (10), 663, arXiv:1706.00428 [hep-ph].

Barshay, S., C. B. Dover, and J. P. Vary (1975), Phys. Rev. **C11**, 360.

Bazavov, A., *et al.* (MILC) (2013), Phys. Rev. **D87** (5), 054505, arXiv:1212.4768 [hep-lat].

Becher, T., and M. Neubert (2011), Eur. Phys. J. **C71**, 1665, arXiv:1007.4005 [hep-ph].

Becker, J., *et al.* (1999), Eur. Phys. J. **A6**, 329.

Belitsky, A. V., and A. V. Radyushkin (2005), Phys. Rept. **418**, 1, arXiv:hep-ph/0504030 [hep-ph].

Benel, J., A. Courtoy, and R. Ferro-Hernandez (2020), Eur. Phys. J. C **80** (5), 465, arXiv:1912.03289 [hep-ph].

Berger, E. L., and J.-w. Qiu (2003), Phys. Rev. **D67**, 034026, arXiv:hep-ph/0210135 [hep-ph].

Berger, E. L., J.-w. Qiu, and X.-f. Zhang (2002a), Phys. Rev. **D65**, 034006, arXiv:hep-ph/0107309 [hep-ph].

Berger, E. R., M. Diehl, and B. Pire (2002b), Eur. Phys. J. **C23**, 675, arXiv:hep-ph/0110062 [hep-ph].

Bermudez Martinez, A., P. Connor, H. Jung, A. Lelek, R. ˘ Zleb˘ cík, F. Hautmann, and V. Radescu (2019), Phys. Rev. D **99** (7), 074008, arXiv:1804.11152 [hep-ph].

Bermuth, J., *et al.* (2003), Phys. Lett. **B564**, 199, arXiv:nucl-ex/0303015 [nucl-ex].

Berthou, B., *et al.* (2018), Eur. Phys. J. **C78** (6), 478, arXiv:1512.06174 [hep-ph].

Bertone, V., I. Scimemi, and A. Vladimirov (2019), JHEP **06**, 028, arXiv:1902.08474 [hep-ph].

Bhat, M., K. Cichy, M. Constantinou, and A. Scapellato (2020), arXiv:2005.02102 [hep-lat].

Bhattacharya, S., K. Cichy, M. Constantinou, A. Metz, A. Scapellato, and F. Steffens (2020a), arXiv:2004.04130 [hep-lat].

Bhattacharya, S., K. Cichy, M. Constantinou, A. Metz, A. Scapellato, and F. Steffens (2020b), arXiv:2005.10939 [hep-ph].

Bhattacharya, S., C. Cocuzza, and A. Metz (2019a), arXiv:1903.05721 [hep-ph].

Bhattacharya, S., C. Cocuzza, and A. Metz (2019b), Phys. Lett. B **788**, 453, arXiv:1808.01437 [hep-ph].

Bhattacharya, T., V. Cirigliano, S. Cohen, R. Gupta, A. Joseph, H.-W. Lin, and B. Yoon (PNDME) (2015), Phys. Rev. **D92** (9), 094511, arXiv:1506.06411 [hep-lat].

Bhattacharya, T., V. Cirigliano, S. D. Cohen, A. Filipuzzi, M. Gonzalez-Alonso, M. L. Graesser, R. Gupta, and H.-W. Lin (2012), Phys. Rev. **D85**, 054512, arXiv:1110.6448 [hep-ph].

Bianconi, A., S. Boffi, R. Jakob, and M. Radici (2000), Phys. Rev. **D62**, 034008, arXiv:hep-ph/9907475 [hep-ph].

Bjorken, J. (1966), Phys. Rev. **148**, 1467.

Bjorken, J. (1970), Phys. Rev. D **1**, 1376.

Blum, T., *et al.* (RBC, UKQCD) (2016), Phys. Rev. **D93** (7), 074505, arXiv:1411.7017 [hep-lat].

Blumlein, J. (2013), Prog. Part. Nucl. Phys. **69**, 28, arXiv:1208.6087 [hep-ph].

Bodek, A., S. Avvakumov, R. Bradford, and H. S. Budd (2008), Eur. Phys. J. C **53**, 349, arXiv:0708.1946 [hep-ex].

Boer, D. (2013), Nucl.Phys. **B874**, 217, arXiv:1304.5387 [hep-ph].

Boer, D., R. Jakob, and M. Radici (2003), Phys. Rev. **D67**, 094003, [Erratum: Phys. Rev.D98,no.3,039902(2018)], arXiv:hep-ph/0302232 [hep-ph].

Boer, D., and P. J. Mulders (1998), Phys. Rev. **D57**, 5780, hep-ph/9711485.

Boer, D., P. J. Mulders, C. Pisano, and J. Zhou (2016), JHEP **08**, 001, arXiv:1605.07934 [hep-ph].

Bomhof, C. J., and P. J. Mulders (2008), Nucl. Phys. **B795**, 409, arXiv:0709.1390 [hep-ph].

Boër, M., M. Guidal, and M. Vanderhaeghen (2015), Eur. Phys. J. **A51** (8), 103.

Bratt, J. D., *et al.* (LHPC) (2010), Phys. Rev. **D82**, 094502, arXiv:1001.3620 [hep-lat].

Braun, V., and D. Müller (2008), Eur. Phys. J. **C55**, 349, arXiv:0709.1348 [hep-ph].

Braun, V. M., A. N. Manashov, and B. Pirnay (2012), Phys. Rev. Lett. **109**, 242001, arXiv:1209.2559 [hep-ph].

Brodsky, S. J., D. S. Hwang, and I. Schmidt (2002), Phys. Lett. **B530**, 99, arXiv:hep-ph/0201296 [hep-ph].

Burkardt, M. (2000), Phys. Rev. **D62**, 071503, [Erratum: Phys. Rev.D66,119903(2002)], arXiv:hep-ph/0005108 [hep-ph].

Burkardt, M. (2013), Phys. Rev. **D88** (1), 014014, arXiv:1205.2916 [hep-ph].

Burkert, V. D., L. Elouadrhiri, and F. X. Girod (2018), Nature **557** (7705), 396.

Burnier, Y., and A. Rothkopf (2013), Phys. Rev. Lett. **111**, 182003, arXiv:1307.6106 [hep-lat].

Butterworth, J., *et al.* (2016), J. Phys. **G43**, 023001, arXiv:1510.03865 [hep-ph].

Cammarota, J., L. Gamberg, Z.-B. Kang, J. A. Miller, D. Pitonyak, A. Prokudin, T. C. Rogers, and N. Sato (2020), arXiv:2002.08384 [hep-ph].

Campbell, J. M., J. Rojo, E. Slade, and C. Williams (2018), Eur. Phys. J. **C78** (6), 470, arXiv:1802.03021 [hep-ph].

Capitani, S., M. Della Morte, D. Djukanovic, G. M. von Hippel, J. Hua, B. Jäger, P. M. Junnarkar, H. B. Meyer, T. D. Rae, and H. Wittig (2019), Int. J. Mod. Phys. **A34** (02), 1950009, arXiv:1705.06186 [hep-lat].

Chambers, A. J., R. Horsley, Y. Nakamura, H. Perlt, P. E. L. Rakow, G. Schierholz, A. Schiller, K. Somfleth, R. D. Young, and J. M. Zanotti (2017), Phys. Rev. Lett. **118** (24), 242001, arXiv:1703.01153 [hep-lat].

Chang, C. C., *et al.* (2018), Nature **558** (7708), 91, arXiv:1805.12130 [hep-lat].

Chen, J.-W., S. D. Cohen, X. Ji, H.-W. Lin, and J.-H. Zhang (2016), Nucl. Phys. **B911**, 246, arXiv:1603.06664 [hep-ph].

Chen, J.-W., T. Ishikawa, L. Jin, H.-W. Lin, Y.-B. Yang, J.-H. Zhang, and Y. Zhao (2018a), Phys. Rev. D **97** (1), 014505, arXiv:1706.01295 [hep-lat].

Chen, J.-W., T. Ishikawa, L. Jin, H.-W. Lin, J.-H. Zhang, and Y. Zhao (LP3) (2019a), Chin. Phys. C **43** (10), 103101, arXiv:1710.01089 [hep-lat].

Chen, J.-W., X. Ji, and J.-H. Zhang (2017), Nucl. Phys. B **915**, 1, arXiv:1609.08102 [hep-ph].

Chen, J.-W., L. Jin, H.-W. Lin, Y.-S. Liu, Y.-B. Yang, J.-H. Zhang, and Y. Zhao (2018b), arXiv:1803.04393 [hep-lat].

Chen, J.-W., H.-W. Lin, and J.-H. Zhang (2019b), 10.1016/j.nuclphysb.2020.114940, arXiv:1904.12376 [hep-lat].

Chiu, J.-Y., A. Jain, D. Neill, and I. Z. Rothstein (2012), JHEP **05**, 084, arXiv:1202.0814 [hep-ph].

Chouika, N., C. Mezrag, H. Moutarde, and J. Rodríguez-Quintero (2017a), *Proceedings, 12th Conference on Quark Confinement and the Hadron Spectrum (Confinement XII): Thessaloniki, Greece*, EPJ Web Conf. **137**, 05020.

Chouika, N., C. Mezrag, H. Moutarde, and J. Rodríguez-Quintero (2017b), Eur. Phys. J. **C77** (12), 906, arXiv:1711.05108 [hep-ph].

Cichy, K., and M. Constantinou (2019), Adv. High Energy Phys. **2019**, 3036904, arXiv:1811.07248 [hep-lat].

Cichy, K., L. Del Debbio, and T. Giani (2019), JHEP **10**, 137, arXiv:1907.06037 [hep-ph].

Collins, J. (2008), *Proceedings, International Workshop on Relativistic nuclear and particle physics (Light Cone 2008): Mulhouse, France, July 7-11, 2008*, PoS **LC2008**, 028, arXiv:0808.2665 [hep-ph].

Collins, J. (2011), Camb. Monogr. Part. Phys. Nucl. Phys. Cosmol. **32**, 1.

Collins, J., and T. Rogers (2015), Phys. Rev. **D91** (7), 074020, arXiv:1412.3820 [hep-ph].

Collins, J., and T. C. Rogers (2017), Phys. Rev. **D96** (5), 054011, arXiv:1705.07167 [hep-ph].

Collins, J. C. (1993), Nucl. Phys. **B396**, 161, arXiv:hep-ph/9208213 [hep-ph].

Collins, J. C. (2002), Phys. Lett. **B536**, 43, arXiv:hep-ph/0204004 [hep-ph].

Collins, J. C. (2003), Acta Phys. Polon. **B34**, 3103, arXiv:hep-ph/0304122 [hep-ph].

Collins, J. C., L. Frankfurt, and M. Strikman (1997), Phys. Rev. **D56**, 2982, arXiv:hep-ph/9611433 [hep-ph].

Collins, J. C., and G. A. Ladinsky (1994), arXiv:hep-ph/9411444 [hep-ph].

Collins, J. C., and D. E. Soper (1981), Nucl. Phys. **B193**, 381, [Erratum: Nucl. Phys.B213,545(1983)].

Collins, J. C., and D. E. Soper (1982), Nucl. Phys. **B197**, 446.

Collins, J. C., D. E. Soper, and G. F. Sterman (1985), Nucl. Phys. **B250**, 199.

Collins, J. C., D. E. Soper, and G. F. Sterman (1989), Adv. Ser. Direct. High Energy Phys. **5**, 1, arXiv:hep-ph/0409313 [hep-ph].

Collins, J. C., and F. V. Tkachov (1992), Phys. Lett. **B294**, 403, arXiv:hep-ph/9208209 [hep-ph].

Collins, J. C., *et al.* (2006), Phys. Rev. **D73**, 014021, hep-ph/0509076.

Constantinou, M., and H. Panagopoulos (2017), Phys. Rev. **D96** (5), 054506, arXiv:1705.11193 [hep-lat].

Constantinou, M., H. Panagopoulos, and G. Spanoudes (2019), Phys. Rev. **D99** (7), 074508, arXiv:1901.03862 [hep-lat].

Cooper-Sarkar, A. M. (H1, ZEUS) (2019), *Proceedings, 27th International Workshop on Deep Inelastic Scattering and Related Subjects (DIS 2019): Torino, Italy, April 8-12, 2019*, PoS **DIS2019**, 029, arXiv:1906.01884 [hep-ph].

Courtoy, A., A. Bacchetta, M. Radici, and A. Bianconi (2012), Phys. Rev. **D85**, 114023, arXiv:1202.0323 [hep-ph].

Courtoy, A., S. Baeßler, M. González-Alonso, and S. Liuti (2015), Phys. Rev. Lett. **115**, 162001, arXiv:1503.06814 [hep-ph].

D'Alesio, U., M. G. Echevarria, S. Melis, and I. Scimemi (2014), JHEP **11**, 098, arXiv:1407.3311 [hep-ph].

D'Alesio, U., C. Flore, and A. Prokudin (2020), Phys. Lett. **B**, 135347, arXiv:2001.01573 [hep-ph].

D'Alesio, U., F. Murgia, C. Pisano, and S. Rajesh (2019), Eur. Phys. J. **C79** (12), 1029, arXiv:1910.09640 [hep-ph].

D'Alesio, U., F. Murgia, C. Pisano, and P. Taels (2017), Phys. Rev. **D96** (3), 036011, arXiv:1705.04169 [hep-ph].

Davies, C. T. H., B. R. Webber, and W. J. Stirling (1985), *22nd International Conference on High Energy Physics. Vol. 1: Leipzig, Germany, July 19-25, 1984*, Nucl. Phys. **B256**, 413, [1,I.95(1984)].

De Florian, D., G. A. Lucero, R. Sassot, M. Stratmann, and W. Vogelsang (2019), Phys. Rev. **D100** (11), 114027, arXiv:1902.10548 [hep-ph].

Defurne, M., *et al.* (Jefferson Lab Hall A) (2015), Phys. Rev. **C92** (5), 055202, arXiv:1504.05453 [nucl-ex].

Defurne, M., *et al.* (Jefferson Lab Hall A) (2016), Phys. Rev. Lett. **117** (26), 262001, arXiv:1608.01003 [hep-ex].

Defurne, M., *et al.* (2017), Nature Commun. **8** (1), 1408, arXiv:1703.09442 [hep-ex].

Detmold, W., I. Kanamori, C. J. D. Lin, S. Mondal, and Y. Zhao (2018), *Proceedings, 36th International Symposium on Lattice Field Theory (Lattice 2018): East Lansing, MI, United States, July 22-28, 2018*, PoS **LATTICE2018**, 106, arXiv:1810.12194 [hep-lat].

Detmold, W., and C. J. D. Lin (2006), Phys. Rev. **D73**, 014501, arXiv:hep-lat/0507007 [hep-lat].

Diehl, M. (2003), Phys. Rept. **388**, 41, arXiv:hep-ph/0307382 [hep-ph].

Diehl, M. (2016), Eur. Phys. J. **A52** (6), 149, arXiv:1512.01328 [hep-ph].

Diehl, M., and D. Yu. Ivanov (2007), Eur. Phys. J. **C52**, 919, arXiv:0707.0351 [hep-ph].

Djukanovic, D., K. Ottnad, J. Wilhelm, and H. Wittig (2019), Phys. Rev. Lett. **123** (21), 212001, arXiv:1903.12566 [hep-lat].

Doi, T., M. Deka, S.-J. Dong, T. Draper, K.-F. Liu, D. Mankame, N. Mathur, and T. Streuer (2009), Phys. Rev. D **80**, 094503, arXiv:0903.3232 [hep-ph].

Dokshitzer, Y. L. (1977), Sov. Phys. JETP **46**, 641, [Zh. Eksp. Teor. Fiz.73,1216(1977)].

Dubbers, D., and M. G. Schmidt (2011), Rev. Mod. Phys. **83**, 1111, arXiv:1105.3694 [hep-ph].

Dulat, S., T.-J. Hou, J. Gao, M. Guzzi, J. Huston, P. Nadolsky, J. Pumplin, C. Schmidt, D. Stump, and C. P. Yuan (2016), Phys. Rev. **D93** (3), 033006, arXiv:1506.07443 [hep-ph].

den Dunnen, W. J., J. P. Lansberg, C. Pisano, and M. Schlegel (2014), Phys. Rev. Lett. **112**, 212001, arXiv:1401.7611 [hep-ph].

Ebert, M. A., S. T. Schindler, I. W. Stewart, and Y. Zhao (2020a), arXiv:2004.14831 [hep-ph].

Ebert, M. A., I. W. Stewart, and Y. Zhao (2019a), Phys. Rev. **D99** (3), 034505, arXiv:1811.00026 [hep-ph].

Ebert, M. A., I. W. Stewart, and Y. Zhao (2019b), JHEP **09**, 037, arXiv:1901.03685 [hep-ph].

Ebert, M. A., I. W. Stewart, and Y. Zhao (2020b), JHEP **03**, 099, arXiv:1910.08569 [hep-ph].

Echevarria, M. G., A. Idilbi, Z.-B. Kang, and I. Vitev (2014), Phys. Rev. **D89**, 074013, arXiv:1401.5078 [hep-ph].

Echevarria, M. G., A. Idilbi, and I. Scimemi (2012), JHEP **07**, 002, arXiv:1111.4996 [hep-ph].

Echevarría, M. G., A. Idilbi, and I. Scimemi (2013), Phys. Lett. **B726**, 795, arXiv:1211.1947 [hep-ph].

Eden, T., *et al.* (1994), Phys. Rev. **C50** (4), R1749.

Engelhardt, M. (2017), Phys. Rev. **D95** (9), 094505, arXiv:1701.01536 [hep-lat].

Engelhardt, M., J. Green, N. Hasan, S. Krieg, S. Meinel, J. Negele, A. Pochinsky, and S. Syritsyn (2018), *Proceedings, 23rd International Symposium on Spin Physics (SPIN2018): Ferrara, Italy, September 10-14, 2018*, PoS **SPIN2018**, 047.

Engelhardt, M., P. Hägler, B. Musch, J. Negele, and A. Schäfer (2016), Phys. Rev. **D93** (5), 054501, arXiv:1506.07826 [hep-lat].

Eskola, K. J., P. Paakkinen, and H. Paukkunen (2019), Eur. Phys. J. **C79** (6), 511, arXiv:1903.09832 [hep-ph].

Eskola, K. J., P. Paakkinen, H. Paukkunen, and C. A. Salgado (2017), Eur. Phys. J. **C77** (3), 163, arXiv:1612.05741 [hep-ph].

Ethier, J. J., and E. R. Nocera (2020), Ann. Rev. Nucl. Part. Sci. (70), 1, arXiv:2001.07722 [hep-ph].

Ethier, J. J., N. Sato, and W. Melnitchouk (2017), Phys. Rev. Lett. **119** (13), 132001, arXiv:1705.05889 [hep-ph].

Evans, L., and P. Bryant (2008), JINST **3**, S08001.

Fai, G. I., J.-w. Qiu, and X.-f. Zhang (2003), Phys. Lett. **B567**, 243, arXiv:hep-ph/0303021 [hep-ph].

Fan, Z.-Y., Y.-B. Yang, A. Anthony, H.-W. Lin, and K.-F. Liu (2018), Phys. Rev. Lett. **121** (24), 242001, arXiv:1808.02077 [hep-lat].

Fischer, C. S., J. M. Pawlowski, A. Rothkopf, and C. A. Welzbacher (2018), Phys. Rev. **D98** (1), 014009, arXiv:1705.03207 [hep-ph].

de Florian, D., R. Sassot, M. Stratmann, and W. Vogelsang (2009), Phys. Rev. **D80**, 034030, arXiv:0904.3821 [hep-ph].

de Florian, D., R. Sassot, M. Stratmann, and W. Vogelsang (2014), Phys. Rev. Lett. **113** (1), 012001, arXiv:1404.4293 [hep-ph].

Follana, E., Q. Mason, C. Davies, K. Hornbostel, G. P. Lepage, J. Shigemitsu, H. Trottier, and K. Wong (HPQCD, UKQCD) (2007), Phys. Rev. **D75**, 054502, arXiv:hep-lat/0610092 [hep-lat].

Gao, H., *et al.* (1994), Phys. Rev. **C50**, R546.

Gehrmann, T., *et al.* (2018), *Proceedings, 13th International Symposium on Radiative Corrections: Application of Quantum Field Theory to Phenomenology (RADCOR2017): St. Gilgen, Austria, September 24-29, 2017*, PoS **RADCOR2017**, 074, arXiv:1801.06415 [hep-ph].

Gelis, F., E. Iancu, J. Jalilian-Marian, and R. Venugopalan (2010), Ann. Rev. Nucl. Part. Sci. **60**, 463, arXiv:1002.0333 [hep-ph].

Georges, F. (2018), *Deeply virtual Compton scattering at Jefferson Lab*, Ph.D. thesis (Institut de Physique Nucléaire d'Orsay, France).

Glazier, D. I., *et al.* (2005), Eur. Phys. J. **A24**, 101, arXiv:nucl-ex/0410026 [nucl-ex].

Goeke, K., M. V. Polyakov, and M. Vanderhaeghen (2001), Prog. Part. Nucl. Phys. **47**, 401, arXiv:hep-ph/0106012 [hep-ph].

Golak, J., G. Ziemer, H. Kamada, H. Witala, and W. Gloeckle (2001), Phys. Rev. **C63**, 034006, arXiv:nucl-th/0008008 [nucl-th].

Goldstein, G. R., J. O. Gonzalez Hernandez, and S. Liuti (2015), Phys. Rev. **D91** (11), 114013, arXiv:1311.0483 [hep-ph].

Goldstein, G. R., R. L. Jaffe, and X.-D. Ji (1995), Phys. Rev. **D52**, 5006, arXiv:hep-ph/9501297 [hep-ph].

Goloskokov, S. V., and P. Kroll (2008), Eur. Phys. J. **C53**, 367, arXiv:0708.3569 [hep-ph].

Goloskokov, S. V., and P. Kroll (2011), Eur. Phys. J. **A47**, 112, arXiv:1106.4897 [hep-ph].

Gonzalez-Hernandez, J. O., S. Liuti, G. R. Goldstein, and K. Kathuria (2013), Phys. Rev. **C88** (6), 065206, arXiv:1206.1876 [hep-ph].

Gonzalez-Hernandez, J. O., T. C. Rogers, N. Sato, and B. Wang (2018), Phys. Rev. **D98** (11), 114005, arXiv:1808.04396 [hep-ph].

Green, J., S. Meinel, M. Engelhardt, S. Krieg, J. Laeuchli, J. Negele, K. Orginos, A. Pochinsky, and S. Syritsyn (2015), Phys. Rev. **D92** (3), 031501, arXiv:1505.01803 [hep-lat].

Green, J. R., K. Jansen, and F. Steffens (2020), Phys. Rev. **D101** (7), 074509, arXiv:2002.09408 [hep-lat].

Green, J. R., J. W. Negele, A. V. Pochinsky, S. N. Syritsyn, M. Engelhardt, and S. Krieg (2014), Phys. Rev. **D90**, 074507, arXiv:1404.4029 [hep-lat].

Grewal, M., Z.-B. Kang, J.-W. Qiu, and A. Signori (2020), arXiv:2003.07453 [hep-ph].

Gribov, V. N., and L. N. Lipatov (1972), Sov. J. Nucl. Phys. **15**, 438, [Yad. Fiz.15,781(1972)].

Grocholski, O., H. Moutarde, B. Pire, P. Sznajder, and J. Wagner (2020), Eur. Phys. J. **C80** (2), 171, arXiv:1912.09853 [hep-ph].

Gupta, R., Y.-C. Jang, H.-W. Lin, B. Yoon, and T. Bhattacharya (2017), Phys. Rev. **D96** (11), 114503, arXiv:1705.06834 [hep-lat].

Gupta, R., Y.-C. Jang, B. Yoon, H.-W. Lin, V. Cirigliano, and T. Bhattacharya (2018), Phys. Rev. **D98**, 034503, arXiv:1806.09006 [hep-lat].

Hagler, P., B. U. Musch, J. W. Negele, and A. Schafer (2009), EPL **88** (6), 61001, arXiv:0908.1283 [hep-lat].

Hagler, P., *et al.* (LHPC) (2008), Phys. Rev. **D77**, 094502, arXiv:0705.4295 [hep-lat].

Hansen, M. T., H. B. Meyer, and D. Robaina (2017), arXiv:1704.08993 [hep-lat].

Harland-Lang, L. A., A. D. Martin, P. Motylinski, and R. S. Thorne (2015), Eur. Phys. J. **C75** (5), 204, arXiv:1412.3989 [hep-ph].

Harland-Lang, L. A., A. D. Martin, P. Motylinski, and R. S. Thorne (2016), Eur. Phys. J. **C76** (4), 186, arXiv:1601.03413 [hep-ph].

Harland-Lang, L. A., A. D. Martin, and R. S. Thorne (2018), Eur. Phys. J. **C78** (3), 248, arXiv:1711.05757 [hep-ph].

Harris, T., G. von Hippel, P. Junnarkar, H. B. Meyer, K. Ottnad, J. Wilhelm, H. Wittig, and L. Wrang (2019), Phys. Rev. **D100** (3), 034513, arXiv:1905.01291 [hep-lat].

Hasan, N., J. Green, S. Meinel, M. Engelhardt, S. Krieg, J. Negele, A. Pochinsky, and S. Syritsyn (2018), Phys. Rev. **D97** (3), 034504, arXiv:1711.11385 [hep-lat].

Hasan, N., J. Green, S. Meinel, M. Engelhardt, S. Krieg, J. Negele, A. Pochinsky, and S. Syritsyn (2019), Phys. Rev. **D99** (11), 114505, arXiv:1903.06487 [hep-lat].

Hasenfratz, A., and F. Knechtli (2001), Phys. Rev. **D64**, 034504, arXiv:hep-lat/0103029 [hep-lat].

Hatta, Y. (2012), Phys. Lett. **B708**, 186, arXiv:1111.3547 [hep-ph].

Hautmann, F., H. Jung, A. Lelek, V. Radescu, and R. Zlebcik (2018), JHEP **01**, 070, arXiv:1708.03279 [hep-ph].

Herberg, C., *et al.* (1999), Eur. Phys. J. **A5**, 131.

Hill, R. J., P. Kammel, W. J. Marciano, and A. Sirlin (2018), Rept. Prog. Phys. **81** (9), 096301, arXiv:1708.08462 [hep-ph].

Hobbs, T. J., B.-T. Wang, P. M. Nadolsky, and F. I. Olness (2019), Phys. Rev. **D100** (9), 094040, arXiv:1904.00022 [hep-ph].

Horkel, D., Y. Bi, M. Constantinou, T. Draper, J. Liang, K.-F. Liu, Z. Liu, and Y.-B. Yang (χQCD) (2020), Phys. Rev. D **101** (9), 094501, arXiv:2002.06699 [hep-lat].

Hou, T.-J., S. Dulat, J. Gao, M. Guzzi, J. Huston, P. Nadolsky, J. Pumplin, C. Schmidt, D. Stump, and C. P. Yuan (2017), Phys. Rev. **D95** (3), 034003, arXiv:1609.07968 [hep-ph].

Hou, T.-J., Z. Yu, S. Dulat, C. Schmidt, and C. P. Yuan (2019a), Phys. Rev. **D100** (11), 114024, arXiv:1907.12177 [hep-ph].

Hou, T.-J., *et al.* (2019b), arXiv:1912.10053 [hep-ph].

Ioffe, B. L. (1969), Phys. Lett. **30B**, 123.

Ishikawa, T., Y.-Q. Ma, J.-W. Qiu, and S. Yoshida (2016), arXiv:1609.02018 [hep-lat].

Izubuchi, T., X. Ji, L. Jin, I. W. Stewart, and Y. Zhao (2018), Phys. Rev. D **98** (5), 056004, arXiv:1801.03917 [hep-ph].

Jaffe, R. L., and X.-D. Ji (1991), Phys. Rev. Lett. **67**, 552.

Jaffe, R. L., X.-m. Jin, and J. Tang (1998), Phys. Rev. Lett. **80**, 1166, arXiv:hep-ph/9709322 [hep-ph].

Jalilian-Marian, J., A. Kovner, A. Leonidov, and H. Weigert (1997), Nucl. Phys. **B504**, 415, arXiv:hep-ph/9701284 [hep-ph].

Jalilian-Marian, J., A. Kovner, A. Leonidov, and H. Weigert (1998a), Phys. Rev. **D59**, 014014, arXiv:hep-ph/9706377 [hep-ph].

Jalilian-Marian, J., A. Kovner, and H. Weigert (1998b), Phys. Rev. **D59**, 014015, arXiv:hep-ph/9709432 [hep-ph].

Jang, Y.-C., T. Bhattacharya, R. Gupta, H.-W. Lin, and B. Yoon (PNDME) (2018), *Proceedings, 36th International Symposium on Lattice Field Theory (Lattice 2018): East Lansing, MI, United States, July 22-28, 2018*, PoS **LATTICE2018**, 123, arXiv:1901.00060 [hep-lat].

Ji, X. (2013), Phys. Rev. Lett. **110**, 262002, arXiv:1305.1539 [hep-ph].

Ji, X. (2014), Sci. China Phys. Mech. Astron. **57**, 1407, arXiv:1404.6680 [hep-ph].

Ji, X., L.-C. Jin, F. Yuan, J.-H. Zhang, and Y. Zhao (2019a), Phys. Rev. **D99** (11), 114006, arXiv:1801.05930 [hep-ph].

Ji, X., Y. Liu, and Y.-S. Liu (2019b), arXiv:1910.11415 [hep-ph].

Ji, X., Y. Liu, and Y.-S. Liu (2019c), arXiv:1911.03840 [hep-ph].

Ji, X., Y.-S. Liu, Y. Liu, J.-H. Zhang, and Y. Zhao (2020), arXiv:2004.03543 [hep-ph].

Ji, X., A. Schäfer, X. Xiong, and J.-H. Zhang (2015a), Phys. Rev. **D92**, 014039, arXiv:1506.00248 [hep-ph].

Ji, X., P. Sun, X. Xiong, and F. Yuan (2015b), Phys. Rev. **D91**, 074009, arXiv:1405.7640 [hep-ph].

Ji, X., X. Xiong, and F. Yuan (2012), Phys. Rev. Lett. **109**, 152005, arXiv:1202.2843 [hep-ph].

Ji, X., and J.-H. Zhang (2015), Phys. Rev. D **92**, 034006, arXiv:1505.07699 [hep-ph].

Ji, X., J.-H. Zhang, and Y. Zhao (2017), Nucl. Phys. B **924**, 366, arXiv:1706.07416 [hep-ph].

Ji, X., J.-H. Zhang, and Y. Zhao (2018), Phys. Rev. Lett. **120** (11), 112001, arXiv:1706.08962 [hep-ph].

Ji, X.-D. (1997), Phys. Rev. Lett. **78**, 610, arXiv:hep-ph/9603249 [hep-ph].

Ji, X.-d., J.-p. Ma, and F. Yuan (2005), Phys. Rev. **D71**, 034005, arXiv:hep-ph/0404183 [hep-ph].

Ji, X.-D., and J. Osborne (1998a), Phys. Rev. **D58**, 094018, arXiv:hep-ph/9801260 [hep-ph].

Ji, X.-D., and J. Osborne (1998b), Phys. Rev. **D57**, 1337, arXiv:hep-ph/9707254 [hep-ph].

Joó, B., J. Karpie, K. Orginos, A. Radyushkin, D. Richards, and S. Zafeiropoulos (2019a), JHEP **12**, 081, arXiv:1908.09771 [hep-lat].

Joó, B., J. Karpie, K. Orginos, A. V. Radyushkin, D. G. Richards, R. S. Sufian, and S. Zafeiropoulos (2019b), Phys. Rev. **D100** (11), 114512, arXiv:1909.08517 [hep-lat].

Joó, B., J. Karpie, K. Orginos, A. V. Radyushkin, D. G. Richards, and S. Zafeiropoulos (2020), arXiv:2004.01687 [hep-lat].

Kanazawa, K., Y. Koike, A. Metz, D. Pitonyak, and M. Schlegel (2016), Phys. Rev. **D93** (5), 054024, arXiv:1512.07233 [hep-ph].

Kang, Z.-B., A. Prokudin, F. Ringer, and F. Yuan (2017), Phys. Lett. **B774**, 635, arXiv:1707.00913 [hep-ph].

Kang, Z.-B., A. Prokudin, P. Sun, and F. Yuan (2016), Phys. Rev. **D93** (1), 014009, arXiv:1505.05589 [hep-ph].

Karpie, J., K. Orginos, A. Rothkopf, and S. Zafeiropoulos (2019), JHEP **04**, 057, arXiv:1901.05408 [hep-lat].

Karpie, J., K. Orginos, and S. Zafeiropoulos (2018), JHEP **11**, 178, arXiv:1807.10933 [hep-lat].

Kim, S., P. Petreczky, and A. Rothkopf (2018), JHEP **11**, 088, arXiv:1808.08781 [hep-lat].

Kotko, P., K. Kutak, C. Marquet, E. Petreska, S. Sapeta, and A. van Hameren (2015), JHEP **09**, 106, arXiv:1503.03421 [hep-ph].

Kovarik, K., *et al.* (2016), Phys. Rev. **D93** (8), 085037, arXiv:1509.00792 [hep-ph].

Kovařík, K., P. M. Nadolsky, and D. E. Soper (2019), arXiv:1905.06957 [hep-ph].

Kovchegov, Y. V. (1999), Phys. Rev. **D60**, 034008, arXiv:hep-ph/9901281 [hep-ph].

Kriesten, B., S. Liuti, L. Calero-Diaz, D. Keller, A. Meyer, G. R. Goldstein, and J. Osvaldo Gonzalez-Hernandez (2020), Phys. Rev. **D101** (5), 054021, arXiv:1903.05742 [hep-ph].

Kubon, G., *et al.* (2002), Phys. Lett. **B524**, 26, arXiv:nucl-ex/0107016 [nucl-ex].

Kumericki, K., T. Lautenschlager, D. Mueller, K. Passek-Kumericki, A. Schaefer, and M. Meskauskas (2011), arXiv:1105.0899 [hep-ph].

Kumericki, K., S. Liuti, and H. Moutarde (2016), Eur. Phys. J. **A52** (6), 157, arXiv:1602.02763 [hep-ph].

Kumerički, K. (2019a), arXiv:1910.04806 [hep-ph].

Kumerički, K. (2019b), Nature **570** (7759), E1.

Kumerički, K., and D. Müller (2016), *Proceedings, 6th International Conference on Physics Opportunities at an ElecTron-Ion Collider (POETIC 2015): Palaiseau, France, September 7-11, 2015*, EPJ Web Conf. **112**, 01012, arXiv:1512.09014 [hep-ph].

Kumerički, K., D. Müller, and M. Murray (2014), Phys. Part. Nucl. **45** (4), 723, arXiv:1301.1230 [hep-ph].

Kusina, A., J.-P. Lansberg, I. Schienbein, and H.-S. Shao (2018), Phys. Rev. Lett. **121** (5), 052004, arXiv:1712.07024 [hep-ph].

Kusina, A., F. Lyonnet, D. B. Clark, E. Godat, T. Jezo, K. Kovarik, F. I. Olness, I. Schienbein, and J. Y. Yu (2017), Eur. Phys. J. **C77** (7), 488, arXiv:1610.02925 [nucl-th].

Landry, F., R. Brock, P. M. Nadolsky, and C. P. Yuan (2003), Phys. Rev. **D67**, 073016, arXiv:hep-ph/0212159 [hep-ph].

Leader, E., and C. Lorcé (2014), Phys. Rept. **541** (3), 163, arXiv:1309.4235 [hep-ph].

Li, Y., D. Neill, and H. X. Zhu (2016), Submitted to: Phys. Rev. D arXiv:1604.00392 [hep-ph].

Li, Y., and H. X. Zhu (2017), Phys. Rev. Lett. **118** (2), 022004, arXiv:1604.01404 [hep-ph].

Liang, J., T. Draper, K.-F. Liu, A. Rothkopf, and Y.-B. Yang (XQCD) (2019), arXiv:1906.05312 [hep-ph].

Liang, J., T. Draper, K.-F. Liu, A. Rothkopf, and Y.-B. Yang (2020), Physical Review D **101** (11), 10.1103/physrevd.101.114503.

Liang, J., K.-F. Liu, and Y.-B. Yang (2018a), *Proceedings, 35th International Symposium on Lattice Field Theory (Lattice 2017): Granada, Spain, June 18-24, 2017*, EPJ Web Conf. **175**, 14014, arXiv:1710.11145 [hep-lat].

Liang, J., Y.-B. Yang, T. Draper, M. Gong, and K.-F. Liu (2018b), Phys. Rev. **D98** (7), 074505, arXiv:1806.08366 [hep-ph].

Lin, H.-W. (2014a), *Proceedings, 31st International Symposium on Lattice Field Theory (Lattice 2013): Mainz, Germany, July 29-August 3, 2013*, PoS **LATTICE2013**, 293.

Lin, H.-W. (2014b), *Proceedings, QCD Evolution Workshop: Newport News, VA, May 6-10, 2013*, Int. J. Mod. Phys. Conf. Ser. **25**, 1460039.

Lin, H.-W., J.-W. Chen, S. D. Cohen, and X. Ji (2015), Phys. Rev. **D91**, 054510, arXiv:1402.1462 [hep-ph].

Lin, H.-W., J.-W. Chen, T. Ishikawa, and J.-H. Zhang (LP3) (2018a), Phys. Rev. **D98** (5), 054504, arXiv:1708.05301 [hep-lat].

Lin, H.-W., J.-W. Chen, X. Ji, L. Jin, R. Li, Y.-S. Liu, Y.-B. Yang, J.-H. Zhang, and Y. Zhao (2018b), Phys. Rev. Lett. **121** (24), 242003, arXiv:1807.07431 [hep-lat].

Lin, H.-W., W. Melnitchouk, A. Prokudin, N. Sato, and H. Shows (2018c), Phys. Rev. Lett. **120** (15), 152502, arXiv:1710.09858 [hep-ph].

Lin, H.-W., and R. Zhang (2019), Phys. Rev. **D100** (7), 074502.

Lin, H.-W., *et al.* (2018d), Prog. Part. Nucl. Phys. **100**, 107, arXiv:1711.07916 [hep-ph].

Liu, K.-F. (2000), Phys. Rev. **D62**, 074501, arXiv:hep-ph/9910306 [hep-ph].

Liu, K.-F. (2016), *Proceedings, 33rd International Symposium on Lattice Field Theory (Lattice 2015): Kobe, Japan, July 14-18, 2015*, PoS **LATTICE2015**, 115, arXiv:1603.07352 [hep-ph].

Liu, K.-F., W.-C. Chang, H.-Y. Cheng, and J.-C. Peng (2012), Phys. Rev. Lett. **109**, 252002, arXiv:1206.4339 [hep-ph].

Liu, K.-F., and S.-J. Dong (1994), Phys. Rev. Lett. **72**, 1790, arXiv:hep-ph/9306299 [hep-ph].

Liu, K. F., S. J. Dong, T. Draper, D. Leinweber, J. H. Sloan, W. Wilcox, and R. M. Woloshyn (1999), Phys. Rev. **D59**, 112001, arXiv:hep-ph/9806491 [hep-ph].

Liu, Y.-S., J.-W. Chen, L. Jin, R. Li, H.-W. Lin, Y.-B. Yang, J.-H. Zhang, and Y. Zhao (2018), arXiv:1810.05043 [hep-lat].

Liu, Y.-S., W. Wang, J. Xu, Q.-A. Zhang, J.-H. Zhang, S. Zhao, and Y. Zhao (2019), Phys. Rev. **D100** (3), 034006, arXiv:1902.00307 [hep-ph].

Ma, Y.-Q., and J.-W. Qiu (2015), *Proceedings, QCD Evolution Workshop (QCD 2014): Santa Fe, USA, May 12-16, 2014*, Int. J. Mod. Phys. Conf. Ser. **37**, 1560041, arXiv:1412.2688 [hep-ph].

Ma, Y.-Q., and J.-W. Qiu (2018a), Phys. Rev. Lett. **120** (2), 022003, arXiv:1709.03018 [hep-ph].

Ma, Y.-Q., and J.-W. Qiu (2018b), Phys. Rev. **D98** (7), 074021, arXiv:1404.6860 [hep-ph].

Madey, R., *et al.* (E93-038) (2003), Phys. Rev. Lett. **91**, 122002, arXiv:nucl-ex/0308007 [nucl-ex].

Martin, A. D., W. J. Stirling, R. S. Thorne, and G. Watt (2009), Eur. Phys. J. **C63**, 189, arXiv:0901.0002 [hep-ph].

Martinelli, G., C. Pittori, C. T. Sachrajda, M. Testa, and A. Vladikas (1995), Nucl. Phys. **B445**, 81, arXiv:hep-lat/9411010 [hep-lat].

Matevosyan, H. H., A. Bacchetta, D. Boer, A. Courtoy, A. Kotzinian, M. Radici, and A. W. Thomas (2018), Phys. Rev. **D97** (7), 074019, arXiv:1802.01578 [hep-ph].

Meng, R., F. I. Olness, and D. E. Soper (1996), Phys. Rev. D **54**, 1919, arXiv:hep-ph/9511311.

Meyer, A. S., M. Betancourt, R. Gran, and R. J. Hill (2016), Phys. Rev. **D93** (11), 113015, arXiv:1603.03048 [hep-ph].

Meyerhoff, M., *et al.* (1994), Phys. Lett. **B327**, 201.

Mezrag, C., H. Moutarde, and F. Sabatié (2013), Phys. Rev. **D88** (1), 014001, arXiv:1304.7645 [hep-ph].

Moffat, E., T. C. Rogers, N. Sato, and A. Signori (2019), Phys. Rev. **D100** (9), 094014, arXiv:1909.02951 [hep-ph].

Mondal, S., R. Gupta, S. Park, B. Yoon, T. Bhattacharya, and H.-W. Lin (2020), arXiv:2005.13779 [hep-lat].

Moutarde, H., B. Pire, F. Sabatie, L. Szymanowski, and J. Wagner (2013), Phys. Rev. **D87** (5), 054029, arXiv:1301.3819 [hep-ph].

Moutarde, H., P. Sznajder, and J. Wagner (2018), Eur. Phys. J. **C78** (11), 890, arXiv:1807.07620 [hep-ph].

Moutarde, H., P. Sznajder, and J. Wagner (2019), Eur. Phys. J. **C79** (7), 614, arXiv:1905.02089 [hep-ph].

Mukherjee, A., and S. Rajesh (2017), Eur. Phys. J. **C77** (12), 854, arXiv:1609.05596 [hep-ph].

Mulders, P. J., and R. D. Tangerman (1996), Nucl. Phys. **B461**, 197, [Erratum: Nucl. Phys.B484,538(1997)], arXiv:hep-ph/9510301 [hep-ph].

Musch, B. U., P. Hagler, M. Engelhardt, J. W. Negele, and A. Schafer (2012), Phys. Rev. **D85**, 094510, arXiv:1111.4249 [hep-lat].

Musch, B. U., P. Hagler, J. W. Negele, and A. Schafer (2011), Phys. Rev. **D83**, 094507, arXiv:1011.1213 [hep-lat].

Müller, D., T. Lautenschlager, K. Passek-Kumericki, and A. Schaefer (2014), Nucl. Phys. **B884**, 438, arXiv:1310.5394 [hep-ph].

Müller, D., D. Robaschik, B. Geyer, F. M. Dittes, and J. Hořejši (1994), Fortsch. Phys. **42**, 101, arXiv:hep-ph/9812448 [hep-ph].

Nocera, E. R. (2017), in *22nd International Symposium on Spin Physics (SPIN 2016) Urbana, IL, USA, September 25-30, 2016*, arXiv:1702.05077 [hep-ph].

Nocera, E. R., R. D. Ball, S. Forte, G. Ridolfi, and J. Rojo (NNPDF) (2014), Nucl. Phys. **B887**, 276, arXiv:1406.5539 [hep-ph].

Nocera, E. R., M. Ubiali, and C. Voisey (2019), arXiv:1912.09543 [hep-ph].

Orginos, K., A. Radyushkin, J. Karpie, and S. Zafeiropoulos (2017), Phys. Rev. **D96** (9), 094503, arXiv:1706.05373 [hep-ph].

Ostrick, M., *et al.* (1999), Phys. Rev. Lett. **83**, 276.

Passchier, I., *et al.* (1999), Phys. Rev. Lett. **82**, 4988, arXiv:nucl-ex/9907012 [nucl-ex].

Paukkunen, H. (LHeC study Group) (2018), *Proceedings, 25th International Workshop on Deep-Inelastic Scattering and Related Topics (DIS 2017): Birmingham, UK, April 3-7, 2017*, PoS **DIS2017**, 109, arXiv:1709.08342 [hep-ph].

Plaster, B., *et al.* (Jefferson Laboratory E93-038) (2006), Phys. Rev. **C73**, 025205, arXiv:nucl-ex/0511025 [nucl-ex].

Polyakov, M. V. (2003), Phys. Lett. **B555**, 57, arXiv:hep-ph/0210165 [hep-ph].

Prokudin, A., P. Sun, and F. Yuan (2015), Phys. Lett. **B750**, 533, arXiv:1505.05588 [hep-ph].

Qiu, J.-W., T. C. Rogers, and B. Wang (2020), arXiv:2004.13193 [hep-ph].

Qiu, J.-w., and X.-f. Zhang (2001a), Phys. Rev. Lett. **86**, 2724, arXiv:hep-ph/0012058 [hep-ph].

Qiu, J.-w., and X.-f. Zhang (2001b), Phys. Rev. **D63**, 114011, arXiv:hep-ph/0012348 [hep-ph].

Radici, M., and A. Bacchetta (2018), Phys. Rev. Lett. **120** (19), 192001, arXiv:1802.05212 [hep-ph].

Radici, M., A. Courtoy, A. Bacchetta, and M. Guagnelli (2015), JHEP **05**, 123, arXiv:1503.03495 [hep-ph].

Radici, M., R. Jakob, and A. Bianconi (2002), Phys. Rev. **D65**, 074031, arXiv:hep-ph/0110252 [hep-ph].

Radici, M., A. M. Ricci, A. Bacchetta, and A. Mukherjee (2016), Phys. Rev. **D94** (3), 034012, arXiv:1604.06585 [hep-ph].

Radyushkin, A. (2017a), Phys. Lett. **B767**, 314, arXiv:1612.05170 [hep-ph].

Radyushkin, A. (2017b), *Proceedings, QCD Evolution Workshop (QCD 2017): Newport News, VA, USA, May 22-26, 2017*, PoS **QCDEV2017**, 021, arXiv:1711.06031 [hep-ph].

Radyushkin, A. (2018a), Phys. Rev. **D98** (1), 014019, arXiv:1801.02427 [hep-ph].

Radyushkin, A. V. (1996), Phys. Lett. **B380**, 417, arXiv:hep-ph/9604317 [hep-ph].

Radyushkin, A. V. (1997), Phys. Rev. **D56**, 5524, arXiv:hep-ph/9704207 [hep-ph].

Radyushkin, A. V. (1999), Phys. Rev. **D59**, 014030, arXiv:hep-ph/9805342 [hep-ph].

Radyushkin, A. V. (2017c), Phys. Rev. **D96** (3), 034025, arXiv:1705.01488 [hep-ph].

Radyushkin, A. V. (2018b), Phys. Lett. **B781**, 433, arXiv:1710.08813 [hep-ph].

Radyushkin, A. V. (2019a), Phys. Rev. **D100** (11), 116011, arXiv:1909.08474 [hep-ph].

Radyushkin, A. V. (2019b), Phys. Lett. **B788**, 380, arXiv:1807.07509 [hep-ph].

Radyushkin, A. V. (2019c), 10.1142/S0217751X20300021, arXiv:1912.04244 [hep-ph].

Rajan, A., A. Courtoy, M. Engelhardt, and S. Liuti (2016), Phys. Rev. **D94** (3), 034041, arXiv:1601.06117 [hep-ph].

Rajan, A., M. Engelhardt, and S. Liuti (2018), Phys. Rev. **D98** (7), 074022, arXiv:1709.05770 [hep-ph].

Rajesh, S., R. Kishore, and A. Mukherjee (2018), Phys. Rev. **D98** (1), 014007, arXiv:1802.10359 [hep-ph].

Rietsch, E. (1977), JOURNAL OF GEOPHYSICS-ZEITSCHRIFT FUR GEOPHYSIK **42** (5), 489.

Rogers, T. C. (2016), Eur. Phys. J. **A52** (6), 153, arXiv:1509.04766 [hep-ph].

Rogers, T. C., and P. J. Mulders (2010), Phys. Rev. **D81**, 094006, arXiv:1001.2977 [hep-ph].

Rohe, D., *et al.* (1999), Phys. Rev. Lett. **83**, 4257.

Rummukainen, K., and H. Weigert (2004), Nucl. Phys. **A739**, 183, arXiv:hep-ph/0309306 [hep-ph].

Sato, N., C. Andres, J. J. Ethier, and W. Melnitchouk (JAM) (2020), Phys. Rev. **D101** (7), 074020, arXiv:1905.03788 [hep-ph].

Sato, N., W. Melnitchouk, S. E. Kuhn, J. J. Ethier, and A. Accardi (Jefferson Lab Angular Momentum) (2016), Phys. Rev. **D93** (7), 074005, arXiv:1601.07782 [hep-ph].

Sawada, T., W.-C. Chang, S. Kumano, J.-C. Peng, S. Sawada, and K. Tanaka (2016), Phys. Rev. **D93** (11), 114034, arXiv:1605.00364 [nucl-ex].

Schiavilla, R., and I. Sick (2001), Phys. Rev. **C64**, 041002, arXiv:nucl-ex/0107004 [nucl-ex].

Schmidt, C., J. Pumplin, C. P. Yuan, and P. Yuan (2018), Phys. Rev. **D98** (9), 094005, arXiv:1806.07950 [hep-ph].

Scimemi, I., and A. Vladimirov (2018), Eur. Phys. J. C **78** (2), 89, arXiv:1706.01473 [hep-ph].

Scimemi, I., and A. Vladimirov (2019), arXiv:1912.06532 [hep-ph].

Seidl, R., *et al.* (Belle) (2017), Phys. Rev. **D96** (3), 032005, arXiv:1706.08348 [hep-ex].

Shanahan, P., M. Wagman, and Y. Zhao (2020a), arXiv:2003.06063 [hep-lat].

Shanahan, P., M. L. Wagman, and Y. Zhao (2020b), Phys. Rev. **D101** (7), 074505, arXiv:1911.00800 [hep-lat].

Shintani, E., K.-I. Ishikawa, Y. Kuramashi, S. Sasaki, and T. Yamazaki (2019), Phys. Rev. **D99** (1), 014510, arXiv:1811.07292 [hep-lat].

Signori, A., A. Bacchetta, M. Radici, and G. Schnell (2013), JHEP **1311**, 194, arXiv:1309.3507 [hep-ph].

Sivers, D. W. (1990), Phys. Rev. **D41**, 83.

Soffer, J. (1995), Phys. Rev. Lett. **74**, 1292, arXiv:hep-ph/9409254 [hep-ph].

Stewart, I. W., and Y. Zhao (2018), Phys. Rev. D **97** (5), 054512, arXiv:1709.04933 [hep-ph].

Sufian, R. S., C. Egerer, J. Karpie, R. G. Edwards, B. Joó, Y.-Q. Ma, K. Orginos, J.-W. Qiu, and D. G. Richards (2020), arXiv:2001.04960 [hep-lat].

Sufian, R. S., J. Karpie, C. Egerer, K. Orginos, J.-W. Qiu, and D. G. Richards (2019), Phys. Rev. **D99** (7), 074507, arXiv:1901.03921 [hep-lat].

Sufian, R. S., Y.-B. Yang, A. Alexandru, T. Draper, J. Liang, and K.-F. Liu (2017), Phys. Rev. Lett. **118** (4), 042001, arXiv:1606.07075 [hep-ph].

Sun, P., J. Isaacson, C. P. Yuan, and F. Yuan (2018), Int. J. Mod. Phys. A **33** (11), 1841006, arXiv:1406.3073 [hep-ph].

Sun, P., and F. Yuan (2013), Phys.Rev. **D88**, 114012, arXiv:1308.5003 [hep-ph].

Tanabashi, M., *et al.* (Particle Data Group) (2018), Phys. Rev. **D98** (3), 030001.

Tangerman, R. D., and P. J. Mulders (1995), Phys. Rev. **D51**, 3357, arXiv:hep-ph/9403227 [hep-ph].

Thorne, R. S., S. Bailey, T. Cridge, L. A. Harland-Lang, A. D. Martin, and R. Nathvani (2019), *Proceedings, 27th International Workshop on Deep Inelastic Scattering and Related Subjects (DIS 2019): Torino, Italy, April 8-12, 2019*, PoS **DIS2019**, 036, arXiv:1907.08147 [hep-ph].

Vinnikov, A. V. (2006), arXiv:hep-ph/0604248 [hep-ph].

Vladimirov, A. A. (2017), Phys. Rev. Lett. **118** (6), 062001, arXiv:1610.05791 [hep-ph].

Vladimirov, A. A., and A. Schäfer (2020), Phys. Rev. **D101** (7), 074517, arXiv:2002.07527 [hep-ph].

Vogelsang, W. (1998), Phys. Rev. **D57**, 1886, arXiv:hep-ph/9706511 [hep-ph].

Vogelsang, W., and F. Yuan (2005), Phys. Rev. **D72**, 054028, hep-ph/0507266.

Vossen, A., *et al.* (Belle) (2011), Phys. Rev. Lett. **107**, 072004, arXiv:1104.2425 [hep-ex].

Walt, M., I. Helenius, and W. Vogelsang (2019), Phys. Rev. **D100** (9), 096015, arXiv:1908.03355 [hep-ph].

Wandzura, S., and F. Wilczek (1977), Phys. Lett. **72B**, 195.

Wang, B., J. O. Gonzalez-Hernandez, T. C. Rogers, and N. Sato (2019a), Phys. Rev. **D99** (9), 094029, arXiv:1903.01529 [hep-ph].

Wang, B.-T., T. J. Hobbs, S. Doyle, J. Gao, T.-J. Hou, P. M. Nadolsky, and F. I. Olness (2018), Phys. Rev. **D98** (9), 094030, arXiv:1803.02777 [hep-ph].

Wang, W., J.-H. Zhang, S. Zhao, and R. Zhu (2019b), Phys. Rev. **D100** (7), 074509, arXiv:1904.00978 [hep-ph].

Warren, G., *et al.* (Jefferson Lab E93-026) (2004), Phys. Rev. Lett. **92**, 042301, arXiv:nucl-ex/0308021 [nucl-ex].

Winter, F., W. Detmold, A. S. Gambhir, K. Orginos, M. J. Savage, P. E. Shanahan, and M. L. Wagman (2017), Phys. Rev. **D96** (9), 094512, arXiv:1709.00395 [hep-lat].

Xiong, X., X. Ji, J.-H. Zhang, and Y. Zhao (2014), Phys. Rev. D **90** (1), 014051, arXiv:1310.7471 [hep-ph].

Yamanaka, N., S. Hashimoto, T. Kaneko, and H. Ohki (JLQCD) (2018), Phys. Rev. **D98** (5), 054516, arXiv:1805.10507 [hep-lat].

Yamanaka, N., B. K. Sahoo, N. Yoshinaga, T. Sato, K. Asahi, and B. P. Das (2017), Eur. Phys. J. **A53** (3), 54,

arXiv:1703.01570 [hep-ph].

Yang, Y.-B., M. Gong, J. Liang, H.-W. Lin, K.-F. Liu, D. Pefkou, and P. Shanahan (2018a), Phys. Rev. D **98** (7), 074506, arXiv:1805.00531 [hep-lat].

Yang, Y.-B., J. Liang, Y.-J. Bi, Y. Chen, T. Draper, K.-F. Liu, and Z. Liu (2018b), Phys. Rev. Lett. **121** (21), 212001, arXiv:1808.08677 [hep-lat].

Yoon, B., M. Engelhardt, R. Gupta, T. Bhattacharya, J. R. Green, B. U. Musch, J. W. Negele, A. V. Pochinsky, A. Schäfer, and S. N. Syritsyn (2017), Phys. Rev. **D96** (9), 094508, arXiv:1706.03406 [hep-lat].

Zhang, J.-H., J.-W. Chen, L. Jin, H.-W. Lin, A. Schäfer, and Y. Zhao (2019a), Phys. Rev. **D100** (3), 034505, arXiv:1804.01483 [hep-lat].

Zhang, J.-H., X. Ji, A. Schäfer, W. Wang, and S. Zhao (2019b), Phys. Rev. Lett. **122** (14), 142001, arXiv:1808.10824 [hep-ph].

Zhang, R., Z. Fan, R. Li, H.-W. Lin, and B. Yoon (2020a), Phys. Rev. **D101** (3), 034516, arXiv:1909.10990 [hep-lat].

Zhang, R., H.-W. Lin, and B. Yoon (2020b), arXiv:2005.01124 [hep-lat].

Zhu, H., *et al.* (E93026) (2001), Phys. Rev. Lett. **87**, 081801, arXiv:nucl-ex/0105001 [nucl-ex].